

# VPLanet: The Virtual Planet Simulator

Rory Barnes<sup>1,2,3</sup>, Rodrigo Luger<sup>2,4</sup>, Russell Deitrick<sup>2,5</sup>, Peter Driscoll<sup>2,6</sup>, Thomas R. Quinn<sup>1,2</sup>, David P. Fleming<sup>1,2</sup>, Hayden Smotherman<sup>1,2</sup>, Diego V. McDonald<sup>1,2</sup>, Caitlyn Wilhelm<sup>1,2</sup>, Rodolfo Garcia<sup>1,2</sup>, Patrick Barth<sup>7</sup>, Benjamin Guyer<sup>1</sup>, Victoria S. Meadows<sup>1,2</sup>, Cecilia Bitz<sup>2,8</sup>, Pramod Gupta<sup>1,2</sup>, Shawn D. Domagal-Goldman<sup>2,9</sup>, John Armstrong<sup>2,10</sup>, David Crisp<sup>2,11</sup>

## ABSTRACT

We describe a software package called `vPLanet` that simulates numerous aspects of planetary system evolution for billions of years, with a focus on habitable worlds. In this initial version, eleven independent models for internal, atmospheric, rotational, orbital, stellar, and galactic processes are included and coupled to self-consistently simulate terrestrial planets, gaseous planets, and stars. We describe these models in detail and validate the code by reproducing observations and/or past results. A key feature of `vPLanet` is that the user can determine at runtime which physics to apply to an individual object, so a single executable can simulate the diverse phenomena that are important across a wide range of planetary and stellar systems. This flexibility is enabled by matrices and vectors of function pointers that are dynamically allocated and populated based on

---

<sup>1</sup>Astronomy Department, University of Washington, Box 951580, Seattle, WA 98195, USA

<sup>2</sup>NASA Virtual Planetary Laboratory Lead Team, USA

<sup>3</sup>E-mail: rory@astro.washington.edu

<sup>4</sup>Center for Computational Astrophysics, Flatiron Institute, New York, NY 10010, USA

<sup>5</sup>Center for Space and Habitability, University of Bern, Gesellschaftsstrasse 6, CH-3012, Bern, Switzerland

<sup>6</sup>Department of Terrestrial Magnetism, Carnegie Institution for Science, 5241 Broad Branch Rd, Washington, DC, 20015, USA

<sup>7</sup>Max Planck Institute for Astronomy, Königstuhl 17, 69117 Heidelberg, Germany

<sup>8</sup>Atmospheric Sciences Department, University of Washington, Box 951580, Seattle, WA 98195, USA

<sup>9</sup>Planetary Environments Laboratory, NASA Goddard Space Flight Center, 8800 Greenbelt Road, Greenbelt, MD 20771, USA

<sup>10</sup>Department of Physics, Weber State University, Ogden, UT 84408-2508, USA

<sup>11</sup>Jet Propulsion Laboratory, California Institute of Technology, M/S 183-501, 4800 Oak Grove Drive, Pasadena, CA 91109, USA

user input. `VPLanet` is publicly available and the repository contains extensive documentation and numerous examples, with code integrity maintained through continuous integration and periodic scanning for memory issues.

## 1. Introduction

Exoplanetary systems show a wide diversity of features, including planetary masses, orbital shapes and sizes, number of sibling planets, and even number of stars. In many systems, these features are qualitatively different from the Solar System, and hence many exoplanets experience an evolution like no planet in our Solar System. Consequently, no single model has yet captured the breadth of architectures and evolutionary processes that can sculpt an arbitrary exoplanet. Here we present a self-consistent physical model of the evolution of gaseous and terrestrial planets in most stellar systems, and its implementation in a software package called `VPLanet`. The approach couples together simple models, *i.e.*, simultaneously solving ordinary differential equations (ODEs), to track the evolution of, and feedbacks between, interior, atmospheric, stellar, orbital, and galactic processes. Below we present the fundamental models, their heritage in various fields of science, and reproduce observations of the Earth, Solar System bodies, and stellar systems. If observations are unavailable, we reproduce previously published results. The software to simulate these processes, `VPLanet`<sup>1</sup>, is open source and includes documentation, examples, and the opportunity for community involvement.

The primary motivation for creating this new model is to determine the evolution of potentially habitable exoplanets. The need for such a model has grown over the last several years with the discovery of approximately Earth-sized planets receiving approximately Earth-like levels of stellar radiation, a combination that can obviously lead to habitable conditions. Moreover, worlds like Proxima Centauri b (Anglada-Escudé et al. 2016) and TRAPPIST-1 c–g (Gillon et al. 2017) orbit bright enough host stars that their atmospheres may be probed with future ground- and space-based facilities (Meadows et al. 2018; Lincowski et al. 2018). With these promising observations on the horizon, a comprehensive model of terrestrial planet evolution is needed to interpret observations, particularly the evolution of an “Earth-like planet.” Here we don’t mean Earth-radius and Earth-mass, but how *the Earth* would evolve in a given system. This paper describes a self-consistent and validated model of planetary system evolution that can be used to simulate the evolution of a  $\sim 1M_{\oplus}$ ,  $\sim 1R_{\oplus}$  terrestrial planet with approximately Earth-like composition and structure. Earth’s

---

<sup>1</sup><https://github.com/VirtualPlanetaryLaboratory/vplanet>

habitability also depends on its environment, primarily the evolution of luminous objects large and/or close massive objects and hence we must include numerous external influences.

Recent theoretical investigations have revealed numerous processes that can severely impact a planet’s potential to support liquid water, even if it is in the habitable zone (HZ; Kasting et al. 1993; Kopparapu et al. 2013). For example, tidal heating may be strong enough to drive a runaway greenhouse (Barnes et al. 2013), the pre-main sequence evolution of low-mass stars may desiccate a planet (Luger & Barnes 2015), and stable resonant orbital oscillations can drive eccentricities above 0.9999 (Barnes et al. 2015). None of these processes is included in the HZ model, but they are all possible for a given planetary system. Thus, the development of a comprehensive theoretical model that can simulate the wide array of phenomena that can remove water from a planet (Meadows & Barnes 2018) is required. Although a tall order, the theoretical models presented below provide a first order approach, and the `vPLanet` software package represents a foundation to compile the relevant phenomena for all planets and moons. The ultimate objectives of `vPLanet` are to 1) simulate newly discovered exoplanets to assess the probability that they possess water, and hence are viable targets for biosignature surveys, and 2) provide a theoretical foundation for the interpretation of spectral and photometric observations of terrestrial planets in terms of habitability and biology.

We define *habitable* to mean a planet that supports liquid surface water, *i.e.*, surface pressures between 10 mbar and 217.75 bars, temperatures between 0 and 374 C, *and* with enough atmospheric water to create global ocean depth of at least 3cm (Abe et al. 2011). These limits correspond to the physical limits of the phase of liquid water and the limit for long-lived humidity, respectively. Our approach is otherwise agnostic to the importance of any one process – a planet is bathed in the luminosity of other objects, moves due the gravitational forces and torques of other objects, transfers material between internal, atmospheric and space reservoirs, and dissipates energy through its interior, atmosphere and ultimately radiation into space. In `vPLanet`, water is tracked in oceanic and atmospheric reservoirs, and is lost to space through hydrodynamic escape. When water abundance and incident stellar radiation (“instellation”) are similar to Earth’s, the climate can be tracked, including ice ages and collapse into a global snowball.

Portions of the algorithm described below have been previously used to study several aspects of stellar and planetary evolution. Deitrick et al. (2018a,b) examined the orbital and rotational dynamics of multiplanet systems and the resulting impact on climate to show that potentially habitable exoplanets can become globally glaciated if their orbital and rotational properties evolve rapidly and with large amplitude. Fleming et al. (2018) showed that the coupled stellar/tidal evolution of tight binary stars can lead to orbital

evolution that ejects circumbinary planets. Lincowski et al. (2018) coupled stellar evolution and atmospheric escape to track water loss and oxygen build-up on the TRAPPIST-1 planets. Finally, Fleming et al. (2019) simulated the coupled stellar/tidal evolution of binary stars to show how unresolved binaries can alter gyrochronology age estimates of stellar populations. Although explicitly designed for habitable worlds, **vPLanet** can be used to model uninhabitable objects, too.

The **vPLanet** code and its ecosystem has been designed to ensure transparency, accessibility, and reproducibility. For example, figures presented below that are derived from **vPLanet** output include a link to the location in the **vPLanet** repository that contains the input files and scripts that generate the figure, *e.g.*, `examples`. Moreover, its modular software design, see § 2, permits new models to be added and coupled to the existing infrastructure with minimal overhead. Thus, the physics appropriate for individual systems or population synthesis models can be added as new observations constrain the observational properties of exoplanets.

This paper is organized as follows. In § 2 we describe the **vPLanet** algorithm and underlying software engineering that enables flexibility with regards to how the “modules” are connected. In §§ 3–13 we qualitatively describe the 11 fundamental models and reproduce previously published results, with quantitative details relegated to Appendices A–K. Briefly, the 11 modules are as follows. We employ simple thermal atmospheric escape models with **AtmEsc** (§ 3, App. A), an analytic model of circumbinary planet orbital evolution with **BINARY** (§ 4, App. B), 2nd and 4th order secular models of orbital evolution with **DistOrb** (§ 5, App. C), a semi-analytic model for the rotational axis due to orbital evolution and the stellar torque with **DistRot** (§ 6, App. D), an approximate model for tidal effects with **EqTide** (§ 7, App. E), a model of Oort Cloud object orbits adopted to capture wide binary orbits with **GalHabit**, (§ 8, App. F), an energy balance climate model with a realistic treatment of ice sheet growth and retreat with **POISE** (§ 9, App. G), radiogenic heating throughout the interior with **RadHeat** (§ 10, App. H), an  $N$ -body model with **SpiNBody** (§ 11, App. I), stellar evolution, including the pre-main sequence, with **STELLAR** (§ 12, J), and an internal, *i.e.*, thermal and magnetic, evolution model that is calibrated to Earth with **ThermInt** (§ 13, App. K). In § 14 we present cases in which multiple models are coupled to reproduce previous results. In § 15 we discuss the value of the coupled model and how it may be used to prioritize targets for life-detection observations. Appendix L is a list of all symbols, and App. M describes **vPLanet**’s accessibility as well as customized tools that streamline its usage.

## 2. The **VPLanet** Algorithm

Models of planetary system evolution must be both comprehensive enough to simulate a planetary system with an arbitrary architecture, as well as flexible enough that extraneous or even inappropriate phenomena are not applied to individual system members. The **VPLanet** approach is to engineer a software framework in which the user selects established models, and the executable assembles the appropriate subroutines to calculate the evolution. Each model has an associated “module” in the code that stores and tracks its properties and the user selects modules for each system member. After checking for self-consistent input, the code can simulate the entire system. This approach permits a simple interface and, more importantly, the opportunity to isolate important processes by easily “turning off” certain physics.

The key software design that permits this flexibility is the use of arrays and matrices of function pointers, *i.e.*, the elements contain function addresses instead of numbers. With this approach **VPLanet** reads in the modules requested by the user and assembles the appropriate governing equations into a multi-dimensional matrix in which one dimension corresponds to a body, the second to a variable, and the third to a process that modifies that variable, see Fig. 1. Parameters that are directly calculated are called “primary variables” and all other properties are derived from them.

The models described in the next 11 sections can all be reduced to ordinary differential equations (ODEs) or explicit functions of time. Thus, to couple the modules together and simulate diverse phenomena, **VPLanet** loops over all the dimensions of the function pointer matrix and solves the equations simultaneously. For parameters influenced by multiple processes, **VPLanet** calculates the derivatives and then sums them to obtain the total derivative.

As an example, consider a system consisting of a star, a close-in planet, and a more distant companion. The star undergoes the stellar evolution process, the inner planet and the star experience tidal effects, and the two planets gravitationally perturb each other. If the user applies the **STELLAR** and **EqTide** modules to the star, the **EqTide**, **DistOrb**, and **DistRot** modules to the inner planet, and the **DistOrb** and **DistRot** modules for the outer planet, then **VPLanet** will simulate the coupled stellar-orbital-tidal-rotational evolution of the 3 objects. In this case, the eccentricity of the inner planet is modified by tidal effects and gravitational perturbations from the other planet, so in the matrix the inner planet’s vector for processes would have 2 members for the two derivatives.

**VPLanet** currently integrates the system of equations using a fourth order Runge-Kutta method with dynamical timestepping. At each timestep, the values of all the derivatives are

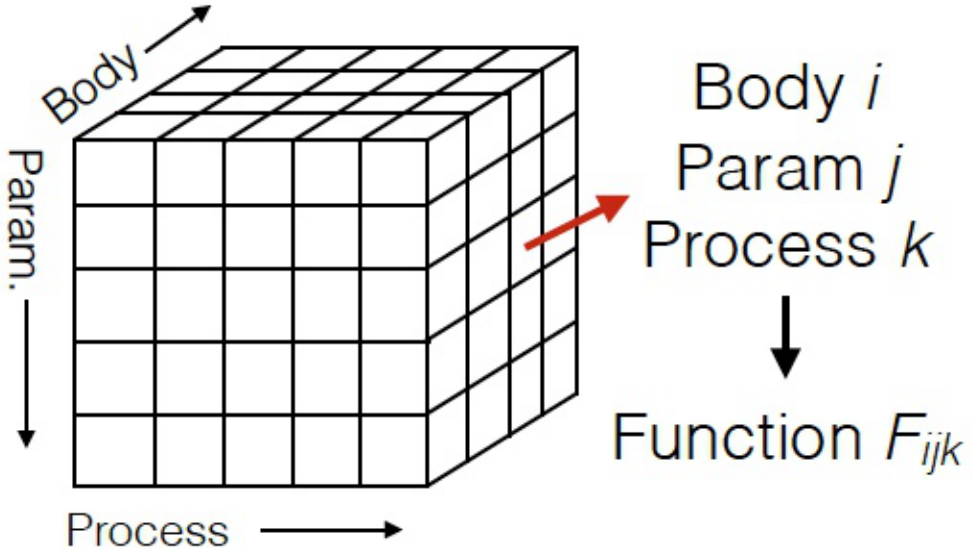


Fig. 1.— Schematic of the matrix of function pointers used by `vPLanet` to integrate a system forward. Each element points to a function that typically contains an ODE. During each timestep, `vPLanet` loops through each body, parameter, and process to solve the entire system simultaneously.

used to calculate a timescale for each process on each body:

$$T_j = \eta \times \min \left| \frac{x_j}{dx_j/dt} \right|, \quad (1)$$

where  $T_j$  is the the timescale of the  $j$ th process,  $\eta$  is a number less than 1 that is tuned to provide the desired accuracy, and  $x_j$  is a variable, *e.g.*, the star's luminosity or a planet's obliquity. All primary variables are updated over the same timescale  $T_j$ , *i.e.*, the timestep is set by the fastest changing variable. In many cases, some variables are updated at a much faster cadence than warranted, but this methodology ensures that all effects are properly modeled. Note that timescales are computed for individual derivatives, not summed derivatives as in the eccentricity example above, the timescales for eccentricity from both tides

and perturbations are calculated. This approach is similar to the stand-alone code EqTide<sup>2</sup> (Barnes 2017), which served as the foundation for vPLanet.

The vPLanet flow chart is shown in Fig. 2. vPLanet first reads in the options set by the user in  $\geq 2$  input files. The primary input file contains the top-level instructions, such as integration parameters (if any), units, and the list of the members of the system. Each system member has a “body file” which contains all the initial conditions, module-specific parameters, and output option selections. After reading in all the options, they are vetted for completeness and inconsistencies in a process called “verify.” After passing this process the physical state and evolution may be self-consistently calculated.

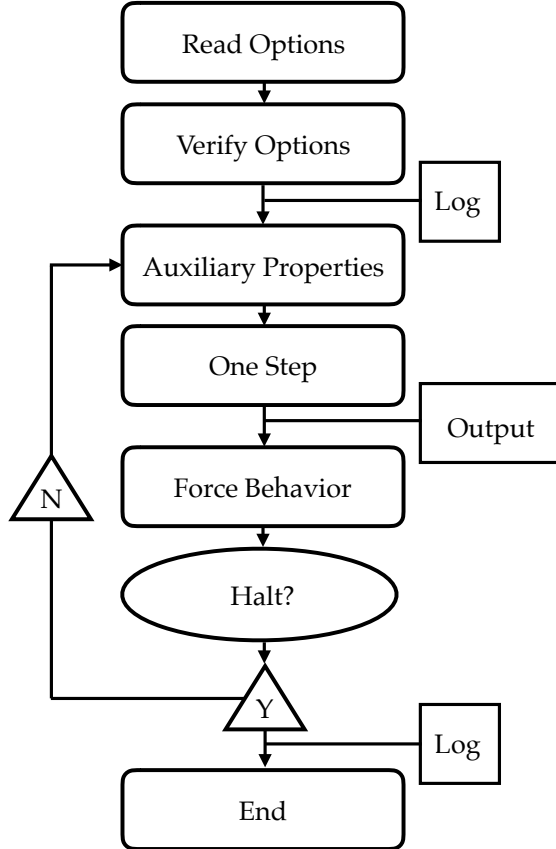


Fig. 2.— The vPLanet flow chart. See text for more details.

After verification, a log file can be written in which the initial state of the system is recorded in SI units, which are the units of vPLanet. At this point, if the user requested

<sup>2</sup><https://github.com/RoryBarnes/EqTide>

an integration, it begins. The evolution is broken up into four parts: 1) calculation of “auxiliary properties,” 2) one step (forward or backward) is taken, 3) if necessary, changes to the integration method are implemented, and 4) checks for any threshold the user set to halt the integration are performed.

Auxiliary properties are not primary variables, but their calculation greatly improves code readability. The second step of the evolutionary stage is to integrate over one time step. The third step is determine if any criterion has been met that requires a change in the evolution, *e.g.*, the loss of an atmosphere or tidal locking. This “force behavior” step can include changing the ODEs that are calculated, fixing parameters to certain values, etc. After this process, **VPLanet** checks if any halting condition has been met, *e.g.*, the user may specify that the execution should be terminated once all water is lost from a planet. If the user has requested to output parameters during the evolution, that is also performed at this stage. Once the integration is complete, the final conditions of the system are recorded in the log file.

Note that in addition to coupling modules through simultaneous solutions of ODEs, coupling also can occur in planetary interiors. For example, in a tidally heated terrestrial planet, the tidal power is a function of temperature (*e.g.*, Driscoll & Barnes 2015), but the temperature is also a function of the tidal power. **VPLanet** couples these connections during the Auxiliary Properties step in Fig. 2.

### 3. Atmospheric Escape: `AtmEsc`

The erosion of a planet’s atmosphere due to extreme stellar radiation is among the biggest challenges to its habitability, particularly around low mass stars (*e.g.*, Lissauer 2007; Scalo et al. 2007; Luger & Barnes 2015). **VPLanet** models the escape of planetary atmospheres and their surface volatiles following simple parametric energy-limited and diffusion-limited prescriptions, which are discussed in detail in § A. In order to validate our approach, in Figure 3 we present a reproduction of Figure 3 in Lopez et al. (2012) using `AtmEsc`. In that study, the authors used a coupled thermal evolution / photoevaporation model to explain the density dichotomy in the Kepler-36 system, which hosts two highly irradiated planets: a low-density mini-Neptune and a high-density super-Earth. The authors showed how, at fixed instellation, the initial core mass dictates the evolution of the gaseous envelope of a sub-giant planet: planets with high-mass cores hold on to their envelopes, while those with low-mass cores are more easily stripped by photoevaporation. As in Lopez et al. (2012), we plot the percentage of the gaseous envelope that is lost as a function of the core mass (top panel), initial envelope mass (center panel), and initial total mass (bottom panel) for

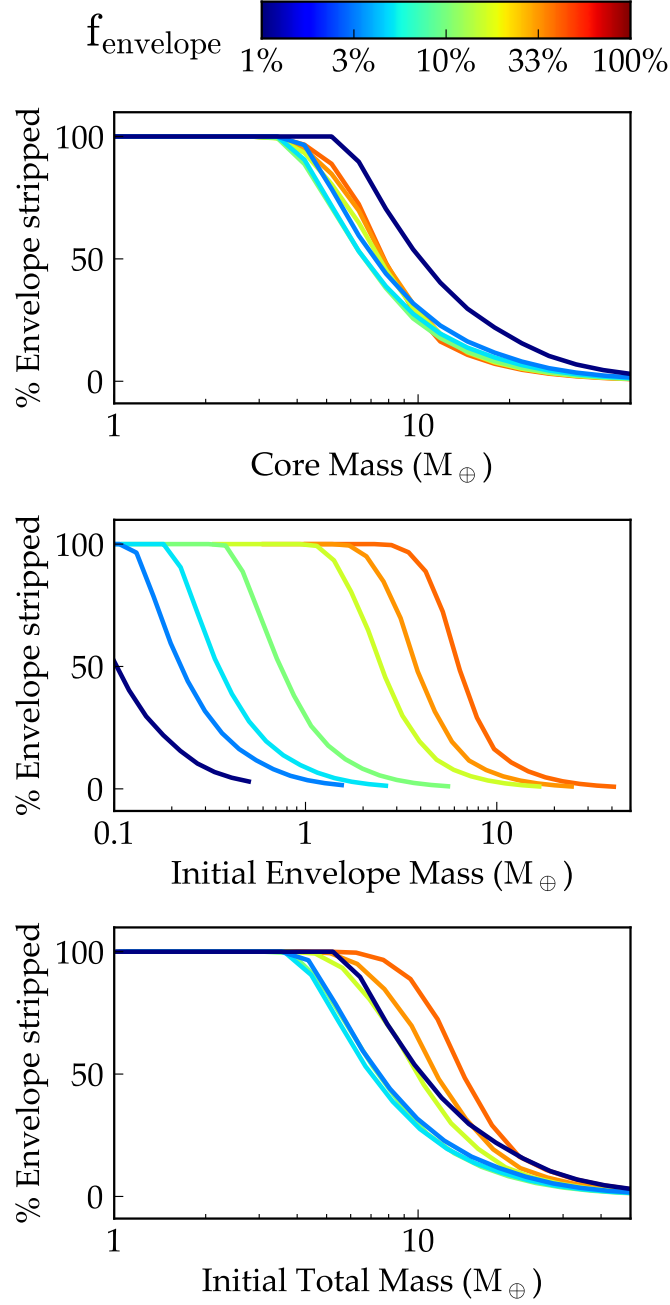


Fig. 3.— Reproduction of Figure 3 in Lopez et al. (2012) using `vPPlanet`. The various curves correspond to the fraction of a planet’s gaseous envelope lost to photoevaporation as a function of the planet core mass (top), the initial envelope mass (center), and the initial total planet mass (bottom). Colors correspond to different initial envelope mass fractions, ranging from 1% (dark blue) to 45% (dark orange). We recover the result of Lopez et al. (2012) that, at fixed instellation, the core mass shows the tightest correlation with the fraction of the envelope that is lost for a mini-Neptune. [examples/AtmEscKepler-36](#)

different initial envelope mass fractions, assuming an escape efficiency  $\epsilon_{XUV} = 0.1$ , a planet age of 5 Gyr, instellation one hundred times that received by Earth, and the XUV evolution model of Ribas et al. (2005) for a solar-mass star. We find, as those authors did, that the core mass displays the tightest correlation with the fraction of the envelope that is lost. Our values generally agree, although **vPLanet** predicts slightly higher escape rates at lower core mass.

#### 4. Circumbinary Planet Orbits: **BINARY**

The recent discovery of transiting circumbinary planets (CBPs) by *Kepler* provides intriguing laboratories to probe the orbital dynamics of such systems. Non-axisymmetric gravitational perturbations from the central binary force CBPs into oscillating orbits that display short and long-term non-Keplerian behavior. The **BINARY** module computes the orbit of a massless test particle on a circumbinary orbit using the analytic theory derived by Leung & Lee (2013). By generalizing the work of Lee & Peale (2006) by extending this theory to the case of an eccentric central binary orbit, Leung & Lee (2013) modeled the orbit of a massless circumbinary planet as a combination of the circular motion of the CBP’s guiding center with radial and vertical epicyclic oscillations induced by non-axisymmetric components of the central binary’s gravitational potential.

Leung & Lee (2013) validated their analytic formalism against direct N-body simulations, and here we validate our implementation of their analytic theory by reproducing their Figure 4 that depicts the orbital evolution of the CBP Kepler-16 b (Doyle et al. 2011). For the initial conditions, we used the orbital parameters for both the binary and CBP given in Table 1 in Leung & Lee (2013) and set the CBP’s  $e_{\text{free}} = 0.03$  following Leung & Lee (2013). The results of our validation simulation are shown in Fig. 4 and are in excellent agreement with Figure 4 from Leung & Lee (2013).

#### 5. Approximate Orbital Evolution: **DistOrb**

An approximate solution to the orbital evolution of a planetary system can be derived from an equation known as the “disturbing function,” a Fourier expansion of the gravitational potential of a multi-body system. First derived by Lagrange and Laplace, this approach produces ODEs for orbital parameters. Outside of mean motion resonances, the equations are known as the “secular” solution, which has the advantage that large time steps (hundreds of years) can be taken. The **DistOrb** module in **vPLanet** is based on the fourth order (in

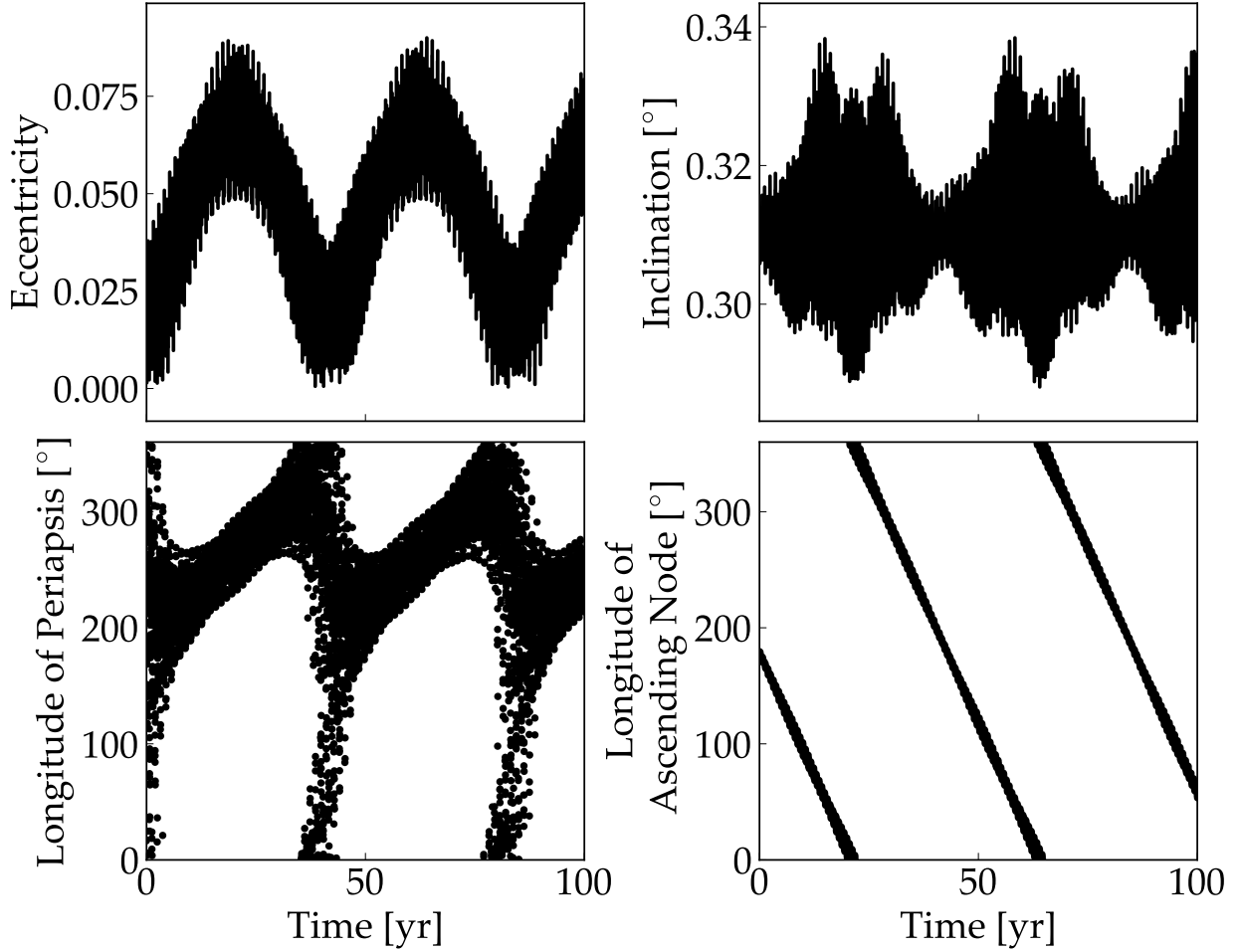


Fig. 4.— `VPLanet` simulation of the orbital evolution of Kepler-16b using the `BINARY` module to be compared with Figure 4 of Leung & Lee (2013). All CBP orbital elements are measured in Jacobi coordinates. *Top left:* CBP orbital eccentricity versus time. *Top right:* CBP orbital inclination relative to the plane of the binary versus time. *Bottom left:* CBP longitude of periaxis versus time. *Bottom right:* CBP longitude of ascending node versus time. [examples/CircumbinaryOrbit](#)

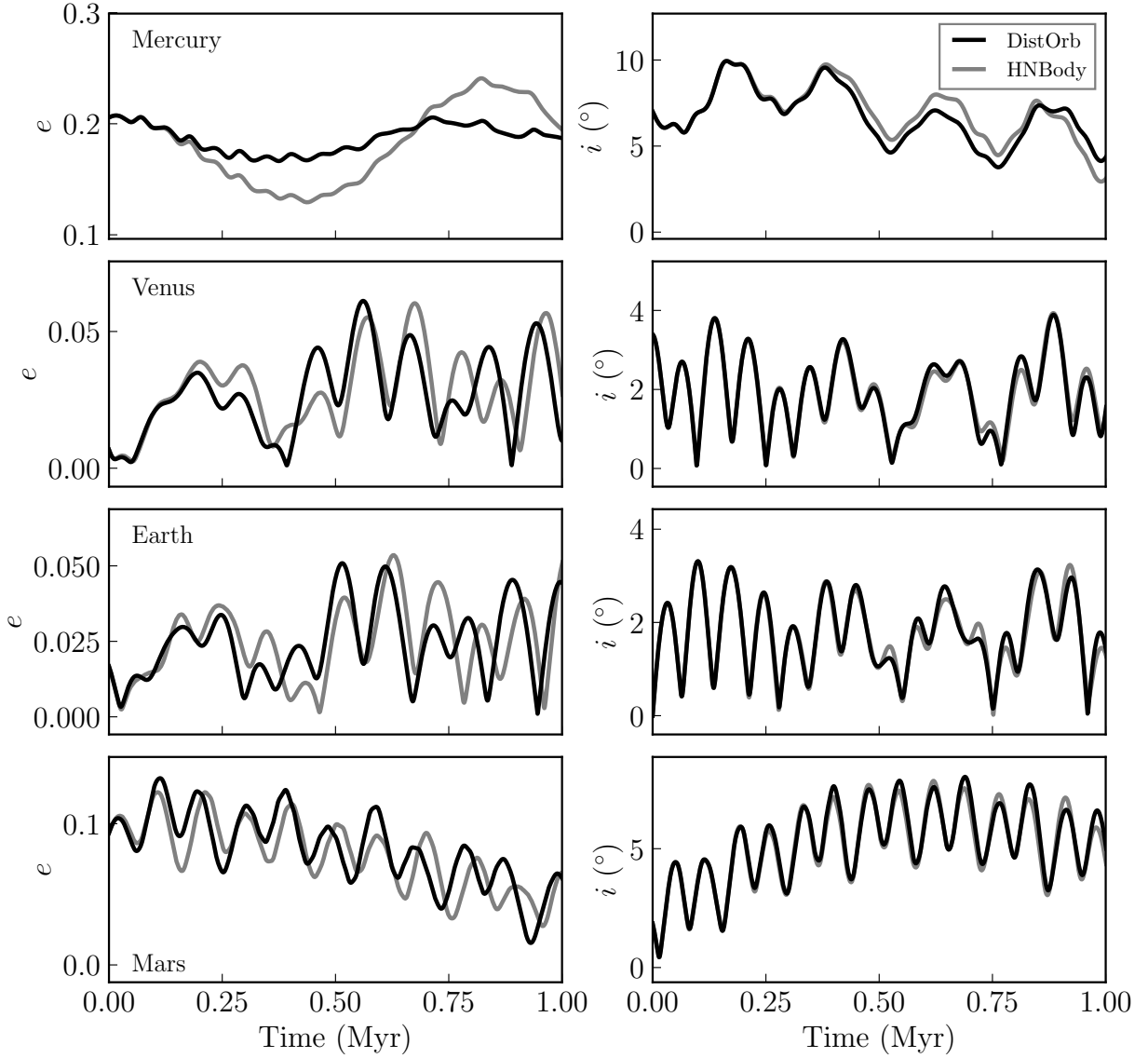


Fig. 5.— Eccentricity evolution (left) and inclination evolution (right) for the inner solar system planets over the next 1 Myr. Black is the result for vPLanet's `DistOrb` module and grey is for the N-body code `HNBODY`. Initial condition are taken from Appendix A of Murray & Dermott (1999). [examples/SSDistOrbDistRot](#)

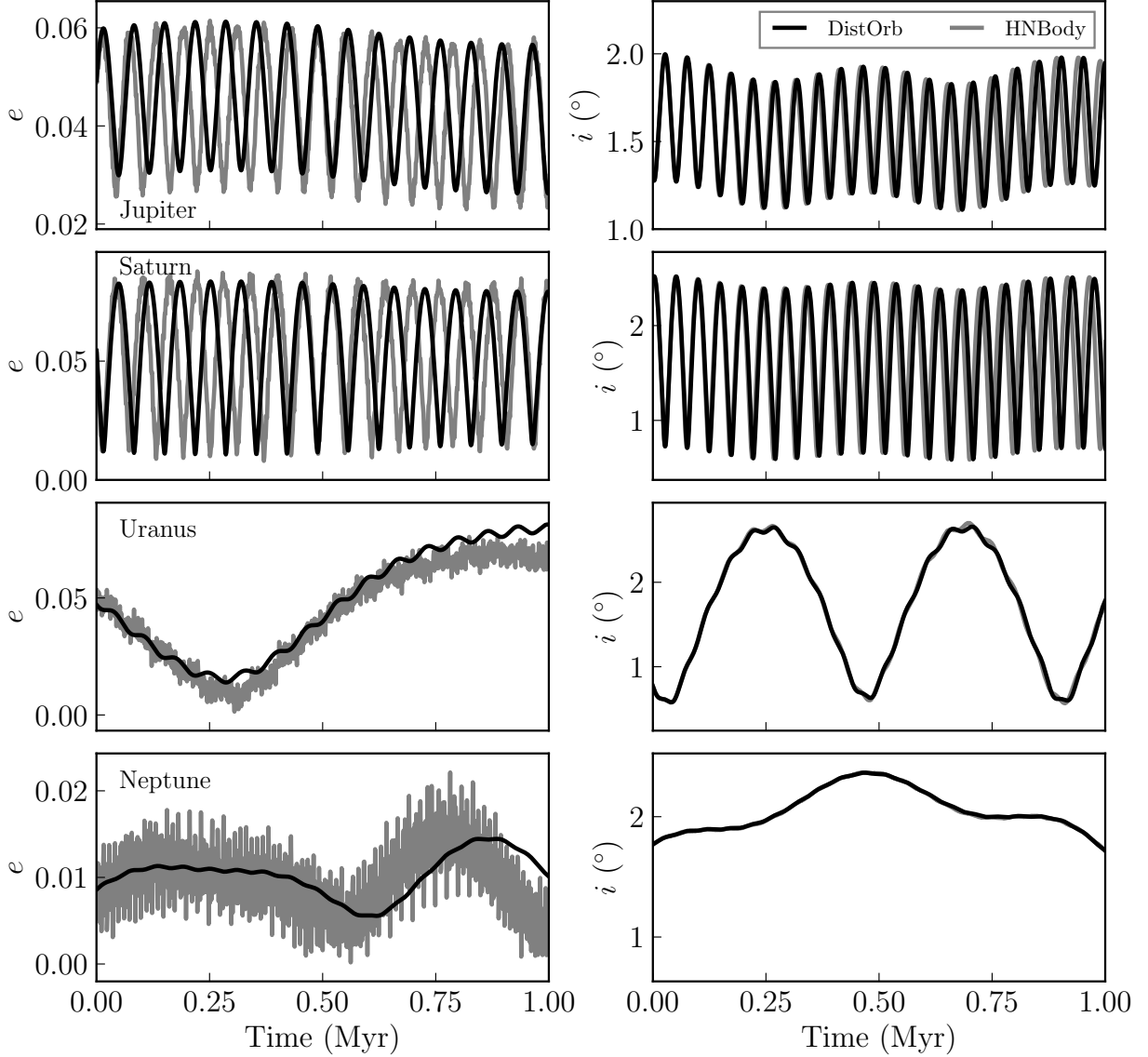


Fig. 6.— Eccentricity evolution (left) and inclination evolution (right) for the outer solar system planets over the next 1 Myr. Black is the result for `VPLanet`'s `DistOrb` module and grey is for the N-body code `HNBODY`. Initial condition are taken from Appendix A of Murray & Dermott (1999). [examples/SSDistOrbDistRot](#)

eccentricity and inclination) secular solution derived in Murray & Dermott (1999) and Ellis & Murray (2000). The theory is developed in App. C; here, we present results from the model.

Figures 5 and 6 show the orbital evolution of the inner solar system planets and the outer solar system planets, respectively, as calculated by `DistOrb` and `HNBody`. The latter software package is an N-body code that calculates the gravitational evolution from first principles (Rauch & Hamilton 2002). For the `DistOrb` runs, we used the fourth-order integration (a second order Lagrange-Laplace solution can be utilized in the code; see App. C). Here we compare to `HNBody` because that model also contains the general relativistic corrections, however, for the solar system these effects are small and `HNBody` results appear almost identical to other N-body integrators.

The inclination evolution in `DistOrb` compares extremely well with `HNBody`. The eccentricity evolution compares reasonably well for most of the planets; the largest error is in the amplitude of Mercury’s eccentricity variation. We do not expect to perfectly reproduce the N-body solution with our secular model, as the Solar System is affected by the proximity of Jupiter and Saturn to a 5:2 mean-motion resonance (Lovett 1895). The other source of error is Mercury’s relatively large eccentricity ( $e \sim 0.2$ ), which the fourth-order model does not handle as well as the direct N-body solution.

## 6. Rotational Evolution from Orbits and the Stellar Torque: `DistRot`

There are a number of physical processes that affect the position of a planet’s spin axis. The module `DistRot` captures the physics of two processes: the torque acting on the equatorial bulge by the host star, and the motion of the planet’s orbital plane (*e.g.*, the change in inclination). The model was derived in Kinoshita (1975) and Kinoshita (1977); see App. D for details.

Figure 6 shows the obliquity evolution for Earth and Mars using `DistRot`. We show the obliquity for Earth over the next Myr with and without the effect of the Moon, which compares extremely well with Laskar et al. (1993), Fig. 11. Note that we do not directly include the effect of the Moon—here, the effect is mimicked by forcing Earth’s precession rate to the known value,  $50.290966''/\text{yr}$  (Laskar et al. 1993).

Mars is more challenging because its obliquity is known to be very sensitive to orbital frequencies (Ward & Rudy 1991; Ward 1992; Touma & Wisdom 1993; Laskar et al. 2004). We show the obliquity evolution utilizing two methods for the orbital evolution over the last 10 Myr. The first couples `DistRot` directly to `DistOrb`. In this case, the obliquity evolution

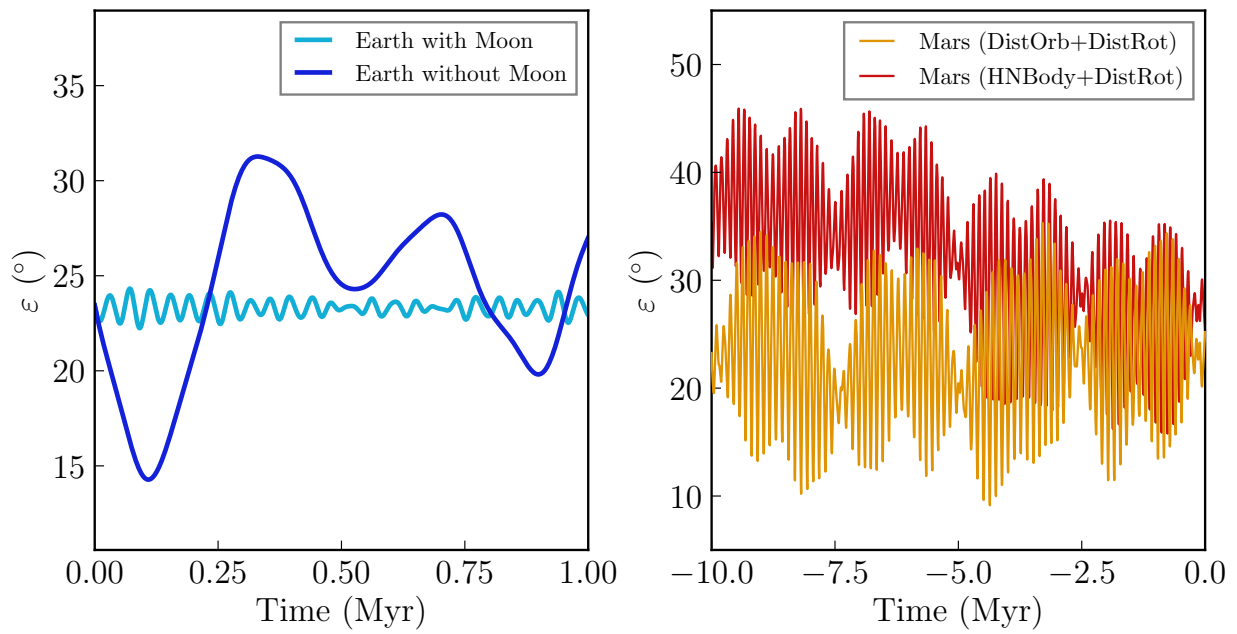


Fig. 7.— Obliquity evolution of Earth with and without the Moon over the next Myr (left) and Mars using secular and N-body models for the orbit over the last 10 Myr (right).  
[examples/SSDistOrbDistRot](#)

over the last  $\sim 5$  Myr compares well with previous studies (*e.g.*, Touma & Wisdom 1993, Fig. 1), but it does not contain the well known shift to a higher obliquity state at  $\sim 5$  Ma. In the second case, we use the orbital evolution from `HNBODY` as input into `DistRot`. This second case does produce the 5 Ma obliquity shift, indicating that the problem lies with the accuracy of the orbital model, not with `DistRot` itself.

## 7. Tidal Effects: `EqTide`

Tidal effects modify a planet by changing its orbit, rotational properties, and generating internal heat. The `EqTide` module employs the “equilibrium tide” models originally developed by Darwin (1880). We specifically use formulations called the “constant-phase lag” (CPL) and “constant-time-lag” (CTL) models developed by Ferraz-Mello et al. (2008) and Leconte et al. (2010), respectively. See App. E for more details on these models.

In Fig. 8, we show the rotational evolution of the putative exoplanet Gl 581 d (Udry et al. 2007), which may be an artefact and not a planet (Robertson et al. 2014). We nonetheless consider this example as it was examined by Heller et al. (2011) and thus provides a straightforward validation of `EqTide`. Physical and orbital parameters are listed in Table 1 (Udry et al. 2007). Fig. 8 is very similar to Fig. 6 in Heller et al. (2011) in which CPL is labeled “FM08” and CTL is “Lec10.” Therefore this aspect of tidal evolution is validated.

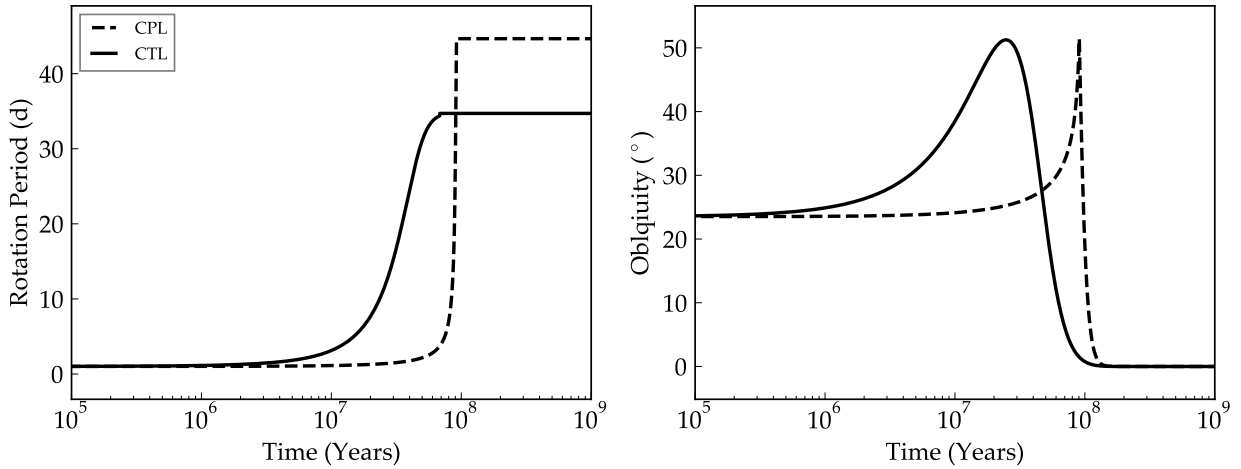


Fig. 8.— *Left:* Rotational period evolution of Gl 581 d for the CPL (dashed curve) and CTL (solid curve) equilibrium tide models and assuming an initial rotation period of 1 day, a tidal Q of 100, and an obliquity of 23.5 degrees. *Right:* Same, but for obliquity. [examples/TideLock](#)

In Fig. 9 we show the tidal heating surface flux of Io as a function of  $e$  and  $\varepsilon$ . The current heat flux is  $1.5 - 3 \text{ W/m}^{-2}$  (Veeder et al. 1994, 2012), and the physical and orbital parameters of Jupiter and Io are listed in Table 1. Io’s orbit has been damped to 0.004 and its eccentricity is likely in a Cassini state, see § 14.4 and Bills & Ray (2000), with an obliquity of  $0.0023^\circ$ , a displacement that remains below the detection threshold. The predicted heat flow of Io is about 2–3 times higher than observed, which has led some researchers to speculate that Io’s heat flow is not in equilibrium (Moore 2003), although it is also likely that the equilibrium tide formalism does not accurately reflect Io’s tidal response. Nonetheless, this result is consistent with previous studies, validating this aspect of tidal effects.

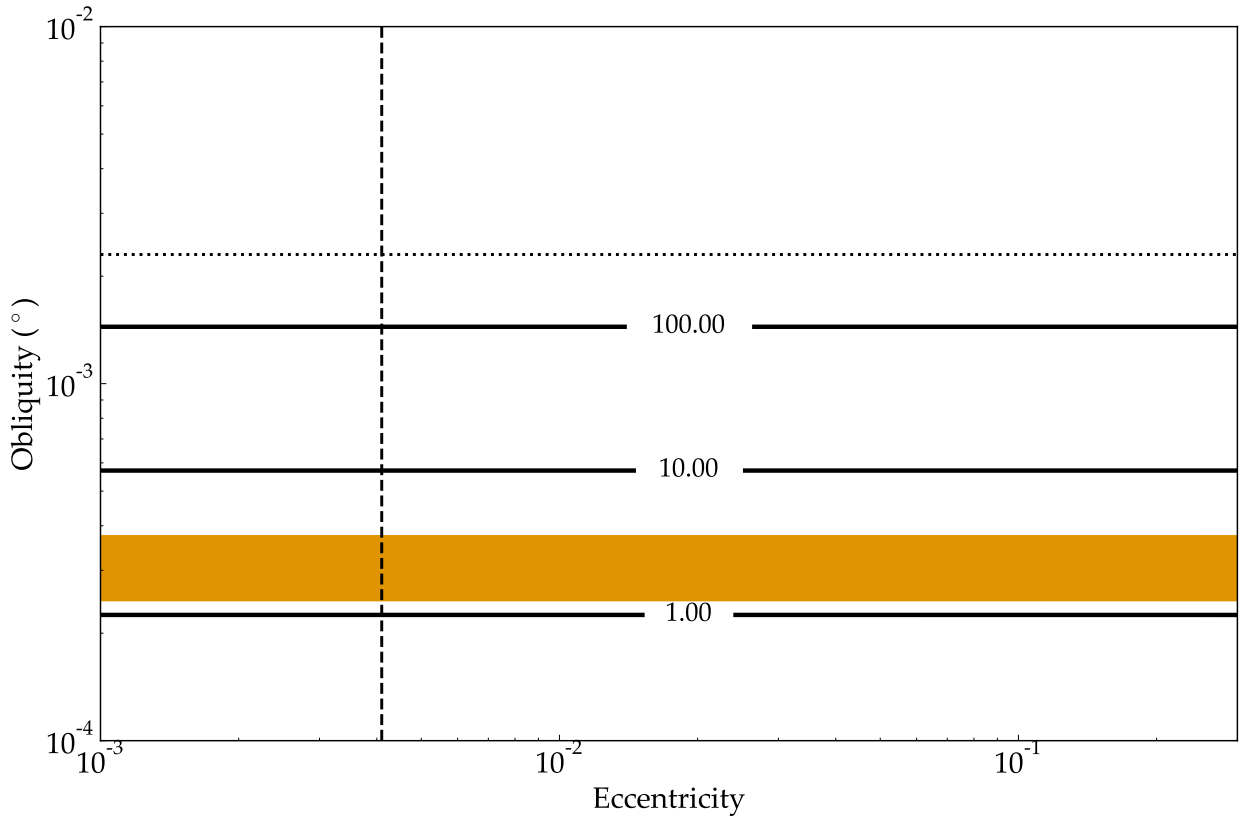


Fig. 9.— Surface tidal heat flux of Io as a function of  $e$  and  $\varepsilon$ . Contour units are  $\text{W/m}^2$ , the vertical line corresponds to Io’s observed eccentricity, and the horizontal line is the expected obliquity if Io is in a Cassini state (Bills & Ray 2000). The orange shaded region corresponds to the observed value of  $1.5 - 3 \text{ W/m}^2$  (Veeder et al. 2012). [examples/IoHeat](#)

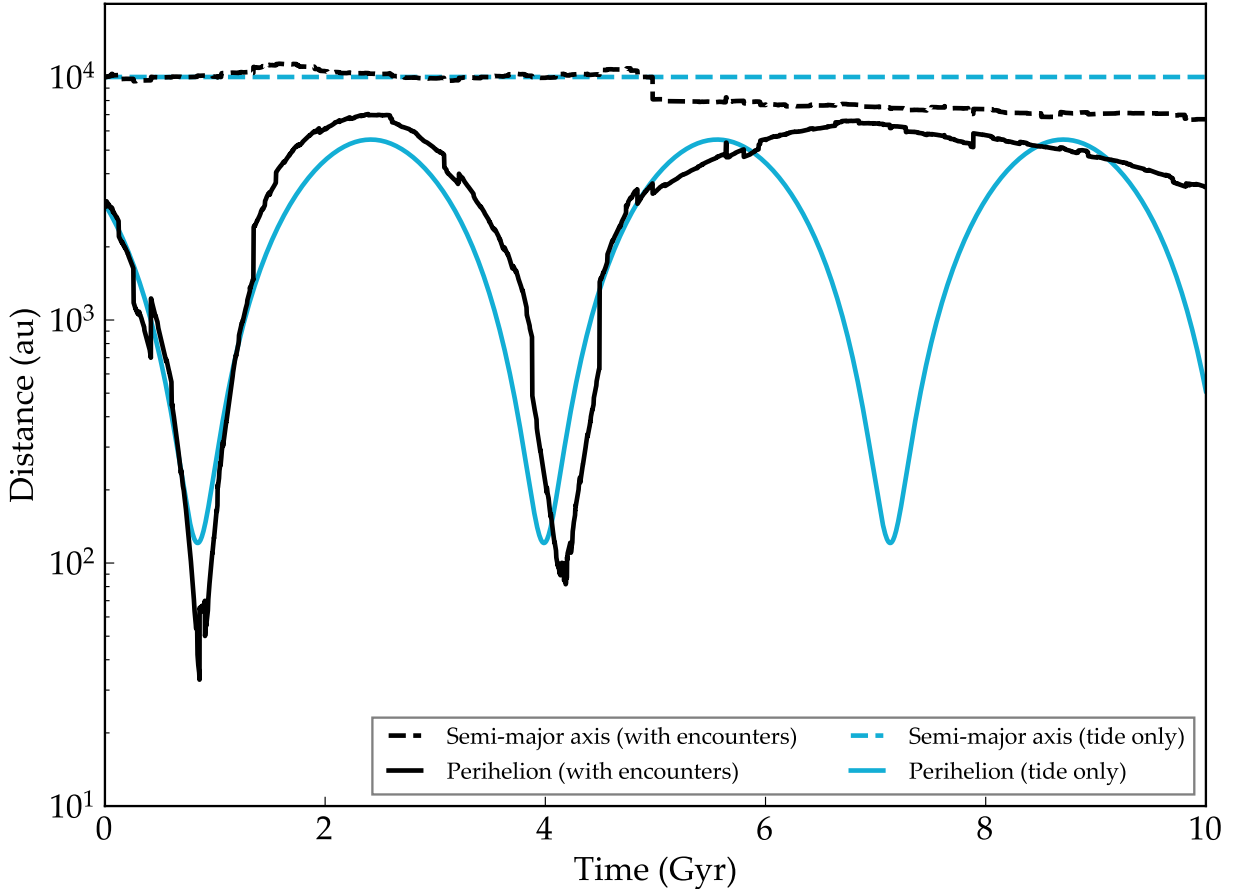


Fig. 10.— Evolution of an M dwarf orbiting the sun under the influence of the galactic environment. The blue curves represent the evolution due to the galactic tide alone, while the black includes the effects of random stellar encounters. The dash curves are the semi-major axis (unaffected by the tide); the solid curves are the perihelion distance. Note that stellar encounters are random, so the black curves are only qualitatively reproducible.  
[examples/GalaxyEffects](#)

## 8. Galactic Evolution: `GalHabit`

The `GalHabit` module accounts for two effects of the galactic environment on the orbits of binary star systems: the galactic tide and perturbations from passing stars. Such effects have been shown to impact the stability of planetary systems (Kaib et al. 2013) and so should be considered when studying planets in wide binary systems. As in the Kaib et al. (2013) study, our model is derived from the work of Heisler & Tremaine (1986), Heisler et al. (1987), and Rickman et al. (2008).

We model the evolution of an M dwarf orbiting the sun, with a mass of  $0.12 M_{\odot}$ ,  $a = 10000$  au,  $e = 0.7$ , and  $i = 80^{\circ}$ . This is similar to the simulation used in Figure 1 of Kaib et al. (2013). Two examples are shown: the evolution of the orbit under the galactic tide alone and the evolution with both the tide and random stellar encounters. We cannot reproduce the evolution shown in Kaib et al. (2013) exactly because our stellar encounters are drawn randomly. Nonetheless, we qualitatively recover the behavior of such a system.

## 9. Climates of Habitable Planets: `POISE`

To model climate, `VPLanet` utilizes an energy balance model (EBM) appropriate for Earth-like atmospheres. `POISE` is based on North & Coakley (1979) who solved for the temperature and albedo as a function of the incoming instellation. An additional component, a model for the dynamics of ice sheets on land, is based on Huybers & Tziperman (2008). The instellation is calculated directly from the planet’s orbital parameters and obliquity and the luminosity of the host star.

In Figure 11 we show the seasonal cycle for Earth as modeled by `POISE`. The instellation, surface temperature, and OLR compare well with other EBMs (North & Coakley 1979). The ice mass balance shows where and when snowing and melting occur. Here, the negative values represent *potential* melting—this value is calculated even in the absence of ice. This allows for easier bookkeeping when calculating the yearly total ice balance.

## 10. Radiogenic Heating: `RadHeat`

The major sources of radiogenic heating are included in the module `RadHeat`, specifically  $^{238}U$ ,  $^{235}U$ ,  $^{232}Th$ ,  $^{40}K$ , and  $^{26}Al$ . On Earth, and presumably other planets, these isotopes are distributed through planetary cores, mantles, and crusts.  $^{26}Al$  is relatively short-lived, but can provide enormous power on planets that form quickly. The evolution of these reservoirs

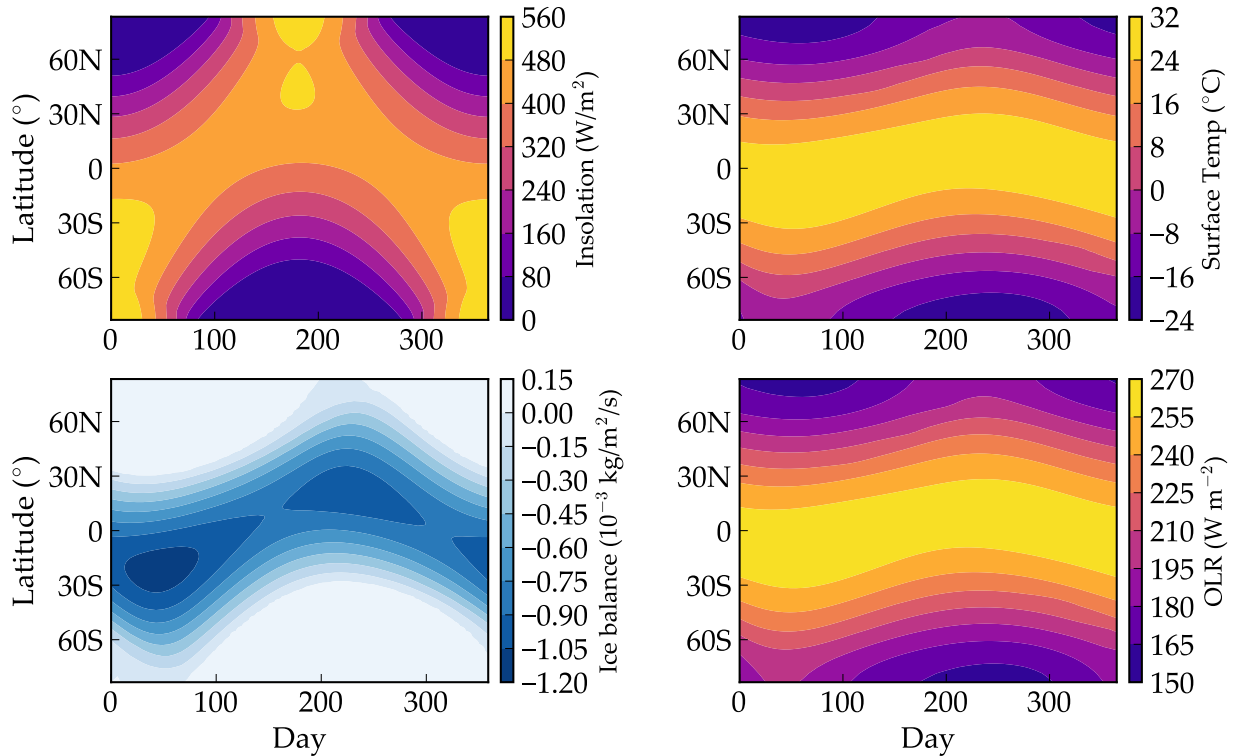


Fig. 11.— Instellation (upper left), surface temperature (upper right), ice mass balance (lower left), and out-going longwave radiation (lower right), for Earth over a single year, as modeled by `POISE`. Note that negative values in ice mass balance represent *potential* melting, *i.e.*, this value is calculated even in the absence of ice on the surface. [examples/EarthClimate](#)

on Earth, described in more details in § 13 and App. K is shown in Fig. 12. For more information on this module, consult App. H.

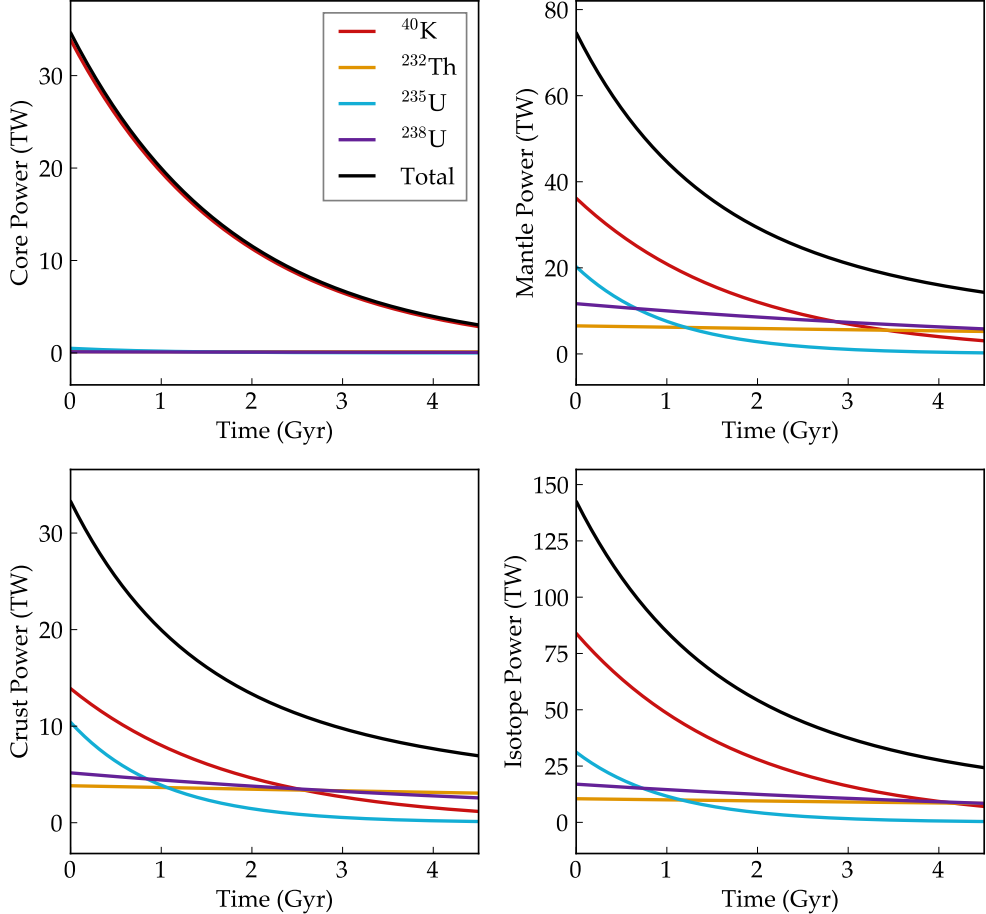


Fig. 12.— Radiogenic heating of the Earth since its formation. *Top Left:* Core power. Note that Th and both U powers are negligible in the core. *Top Right:* Mantle power. *Bottom Left:* Crust power. *Bottom Right:* Power by isotope. [examples/RadHeat](#)

## 11. Accurate Orbital Evolution: SpiNBody

The vPLAnet N-body model, **SpiNBody**, directly calculates the gravitational acceleration between massive objects. As this calculation is from first principles, **SpiNBody** is valid for any configuration. Figure 13 reproduces Fig. 13 from Barnes et al. (2015). This system consists of a solar-type star, an Earth-mass planet in the HZ, and outer Neptune-mass planet in a 3:1 resonance. The eccentricity occasionally surpasses 0.9999, but the system is stable for 10

Gyr. The results in Barnes et al. (2015) were performed with `HNBODY` and `MERCURY`, and thus `SpiNBody` is validated.

## 12. Stellar Evolution: `STELLAR`

`VPLanet`'s stellar evolution module, `STELLAR`, tracks the evolution of the fundamental stellar parameters of low-mass ( $M_\star \lesssim 1.4M_\odot$ ) stars, including a star's radius, radius of gyration,  $r_g$ , effective temperature, luminosity, XUV luminosity, and rotation rate. These evolving stellar parameters shape the dynamics and habitability of stellar and exoplanetary systems. For example, exoplanets orbiting in the habitable zone of late M-dwarfs likely experienced an extended runaway greenhouse during the host star's superluminous pre-main sequence phase, potentially driving extreme water loss (*e.g.*, Luger & Barnes 2015). The combination of evolving stellar radii and magnetic braking, the long-term removal of stellar angular momentum arising from the coupling of the stellar wind with the surface magnetic field, dictate the stellar angular momentum budget, molding observed stellar rotation period distributions as a function of stellar age and mass (*e.g.*, Skumanich 1972; McQuillan et al. 2014; Matt et al. 2015). Moreover, in stellar binaries, coupled stellar-tidal evolution depends intimately on the evolving stellar radii and rotation periods, driving orbital circularization on the pre-main sequence (*e.g.*, Zahn 1989) and can destabilizes any circumbinary planets they may harbor (*e.g.*, Fleming et al. 2018). Here, we demonstrate the modeling capabilities of `STELLAR`, while in the App. J, we describe the numerical and theoretical details of the module.

`STELLAR` models stellar evolution via a bicubic interpolation of the Baraffe et al. (2015) stellar evolution models of solar metallicity stars over mass and time, assuming  $f_{sat} = 10^{-3}$ ,  $t_{sat} = 1$  Gyr, and  $\beta_{XUV} = -1.23$  (Ribas et al. 2005). `STELLAR` computes the XUV luminosity according to the product of the luminosity and Eq. (J1) for stars that drive atmospheric escape and water loss (see § 3; Luger & Barnes 2015) Furthermore, `STELLAR` allows the user to model the long-term angular momentum evolution of low-mass stars using one of three magnetic braking models (Reiners & Mohanty 2012; Repetto & Nelemans 2014; Matt et al. 2015, 2019). We demonstrate the evolution predicted by `STELLAR` in Figure 14 that depicts the evolution of the stellar radius,  $r_g$ , temperature, luminosity, and XUV luminosity, the latter computed using Eq. J1, all as function of time for several stars ranging in mass from late M dwarfs ( $M_\star = 0.08M_\odot$ ) to late F dwarfs ( $M_\star = 1.3M_\odot$ ). Our tracks agree with present-day solar values and display the well-known extended pre-main sequence phase of M dwarfs (*e.g.*, Luger & Barnes 2015).

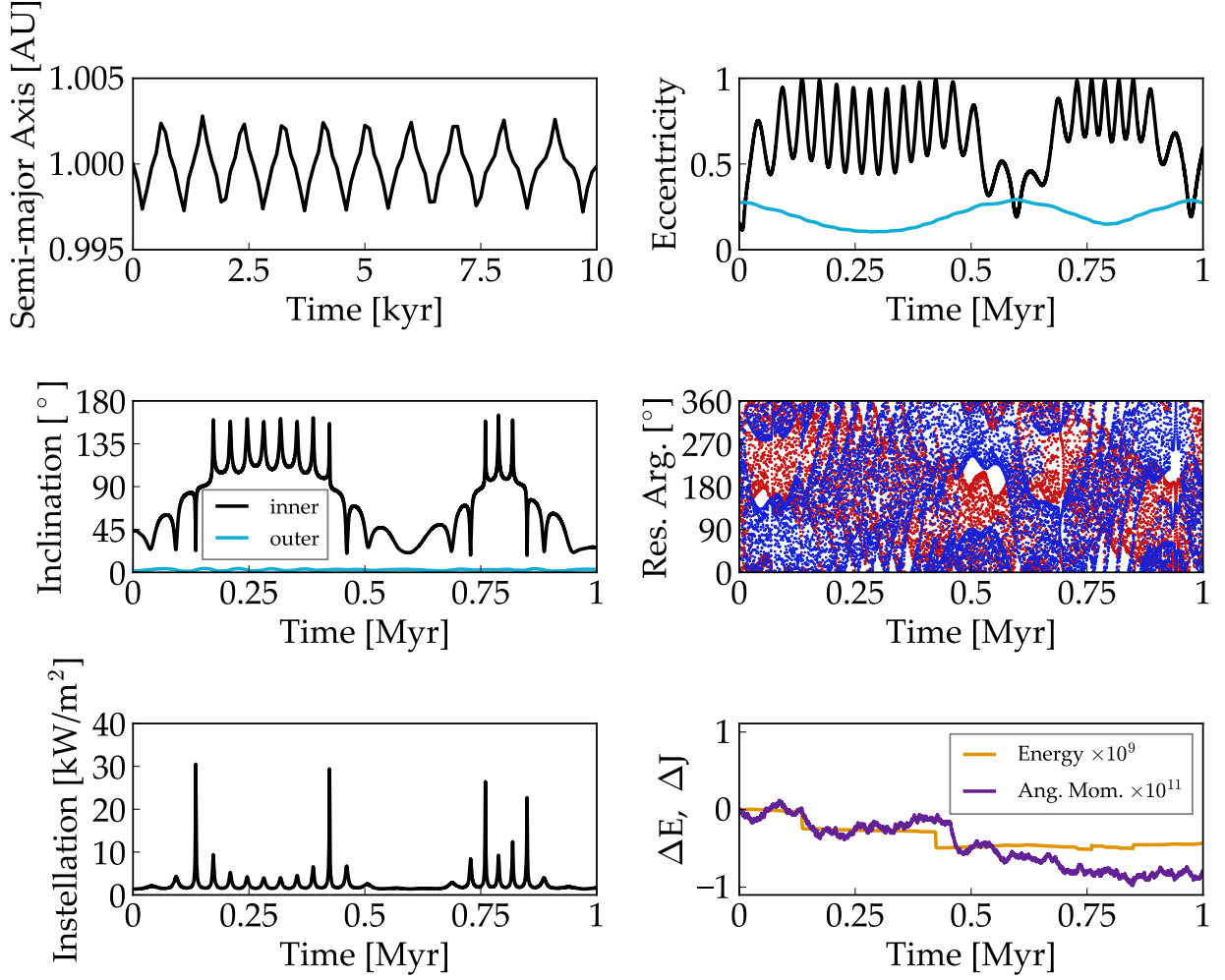


Fig. 13.— Evolution of a planetary system in a chaotic 3:1 eccentricity-inclination resonance. *Top left:* Semi-major axis of the inner planet. Note the *x*-axis timescale. *Top right:* Eccentricity. The black curve is for the inner planet, blue for outer. *Middle left:* Inclination. *Middle right:* The two resonant arguments:  $(3\lambda' - \lambda - 2\varpi)$  in red and  $(3\lambda' - \lambda - 2\varpi')$  in blue, where primes indicate the outer planet. *Bottom left:* Orbit-averaged instellation of the inner planet. *Bottom right:* Evolution of total energy (orange) and angular momentum (purple).

[examples/ChaoticResonances](#)

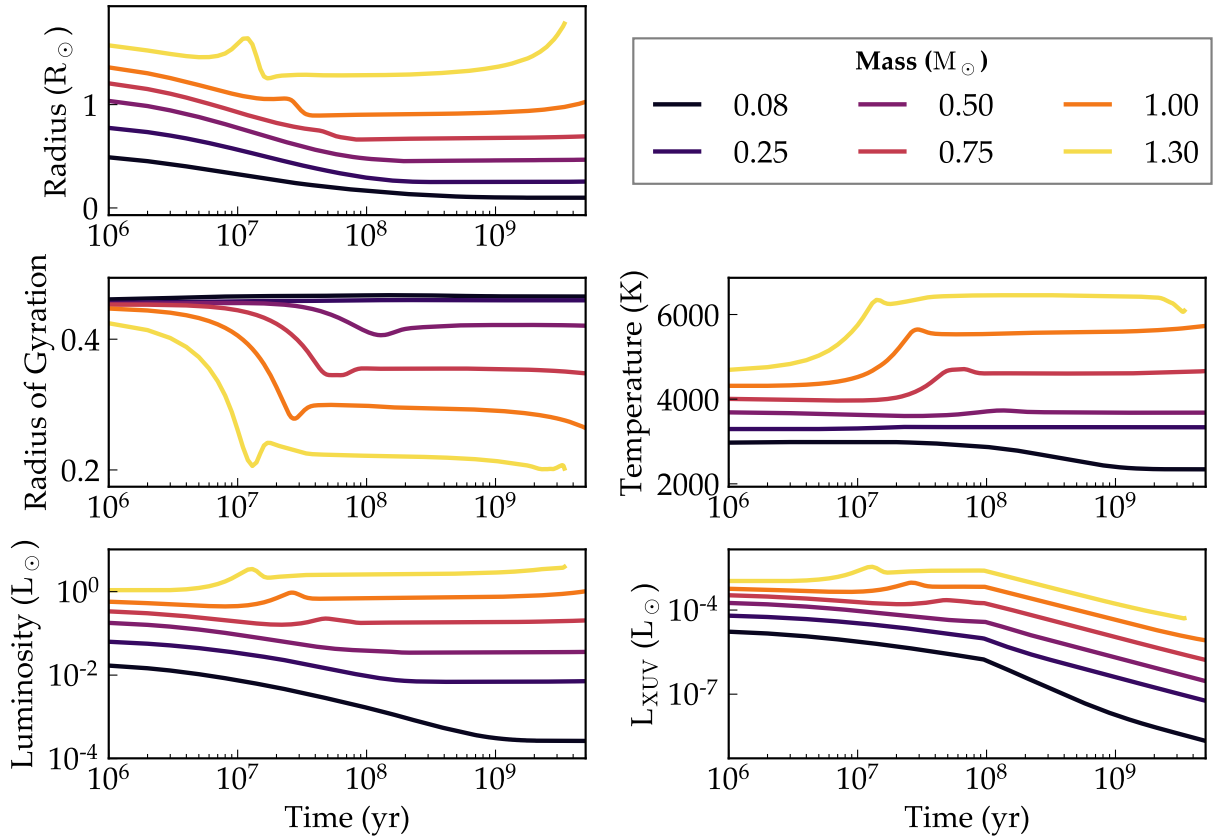


Fig. 14.— Evolution of the radius (top left), radius of gyration (middle left), luminosity (bottom left), effective temperature (middle right), and XUV luminosity (bottom right) of stars of different masses predicted by the `STELLAR` module. [examples/StellarEvol](#)

### 13. Geophysical Evolution: `ThermInt`

The thermal and magnetic evolution of Earth’s interior is modeled in `ThermInt` by solving a coupled heat balance in the mantle and core by assuming parameterized heat flow scalings and material properties appropriate for Earth. A nominal Earth-model is calibrated to approximately reproduce the main constraints on the thermal and magnetic evolution: present-day mantle potential temperature of 1630 K, mantle surface heat flow of 38 TW, upwelling mantle melt fraction of 7%, inner core radius of 1221 km, and a continuous core magnetic field. The radiogenic abundances assumed in the mantle are based on the bulk silicate Earth (Arevalo et al. 2013; Jaupart et al. 2015) and 3 TW of  $K^{40}$  in the core today to maintain a continuous dynamo (Driscoll & Bercovici 2014). Using the default Earth values, `ThermInt +RadHeat` produce an “Earth interior model” with the following values at 4.5 Gyr:  $Q_{surf} = 33.4$  TW,  $Q_{cmb} = 13.5$  TW,  $T_{UM} = 1587$  K,  $T_{CMB} = 4000$  K,  $R_{ic} = 1224$  km,  $M = 80$  ZAm<sup>2</sup>, and inner core nucleation at 3.97 Gyr (0.53 Ga). For the nominal Earth-model Figure 15 shows the thermal evolution of the mantle and core temperatures, heat flows, thermal boundary layer thicknesses, mantle viscosities, upwelling mantle melt fraction, and mantle melt mass flux over time. Figure 16 shows the thermal and magnetic evolution of the core in terms of inner core radius, core buoyancy fluxes, geodynamo magnetic moment, and magnetopause radius over time.

## 14. Multi-Module Applications

In this section we present results in which the previous modules are coupled together and reproduce previous results.

### 14.1. Milankovitch Cycles

In this subsection we demonstrate `VPLanet`’s ability to qualitatively reproduce Milankovitch cycles on Earth. This section utilizes `DistOrb`, `DistRot`, and `POISE`. Note that in order to reproduce the effect of Earth’s moon on Earth’s obliquity, we force the precession rate to be 50.290966'' year<sup>-1</sup> (Laskar et al. 1993). This choice does not perfectly match the dynamics of the Earth-moon-sun system, but it is close enough to replicate the physics of the ice age cycles. The surface properties are shown in Figure 17 (see Huybers & Tziperman 2008, Figure 4 for comparison), for a 200,000 year window. The ice sheets in the northern hemisphere high latitude region grow and retreat as the obliquity, eccentricity, and climate-precession-parameter, or CPP ( $e \sin(\varpi + \psi)$ ), vary. The ice deposition rate is less than that used by

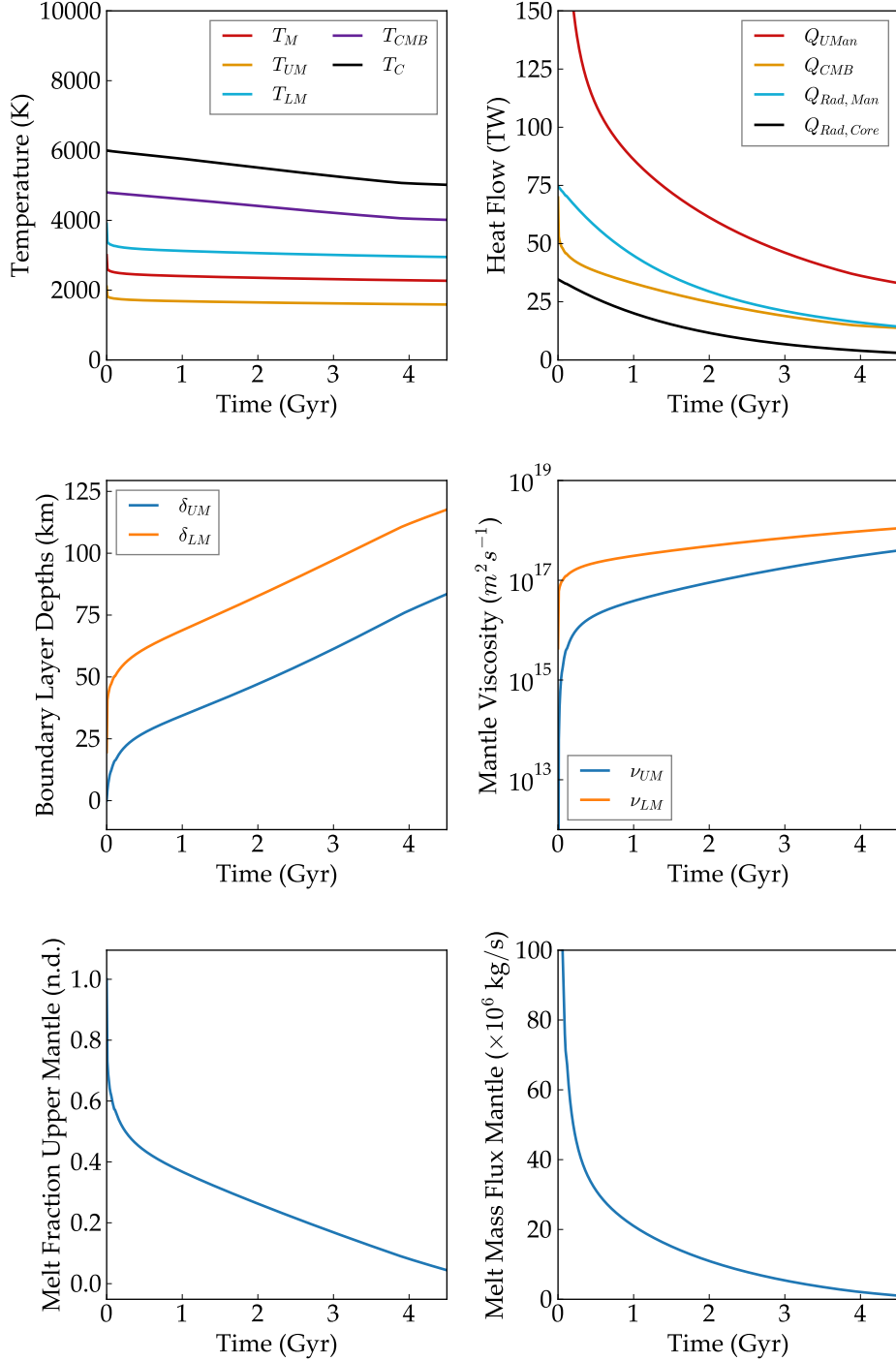


Fig. 15.— Thermal evolution of Earth’s mantle and some resultant material properties.  
[examples/EarthInterior](#)

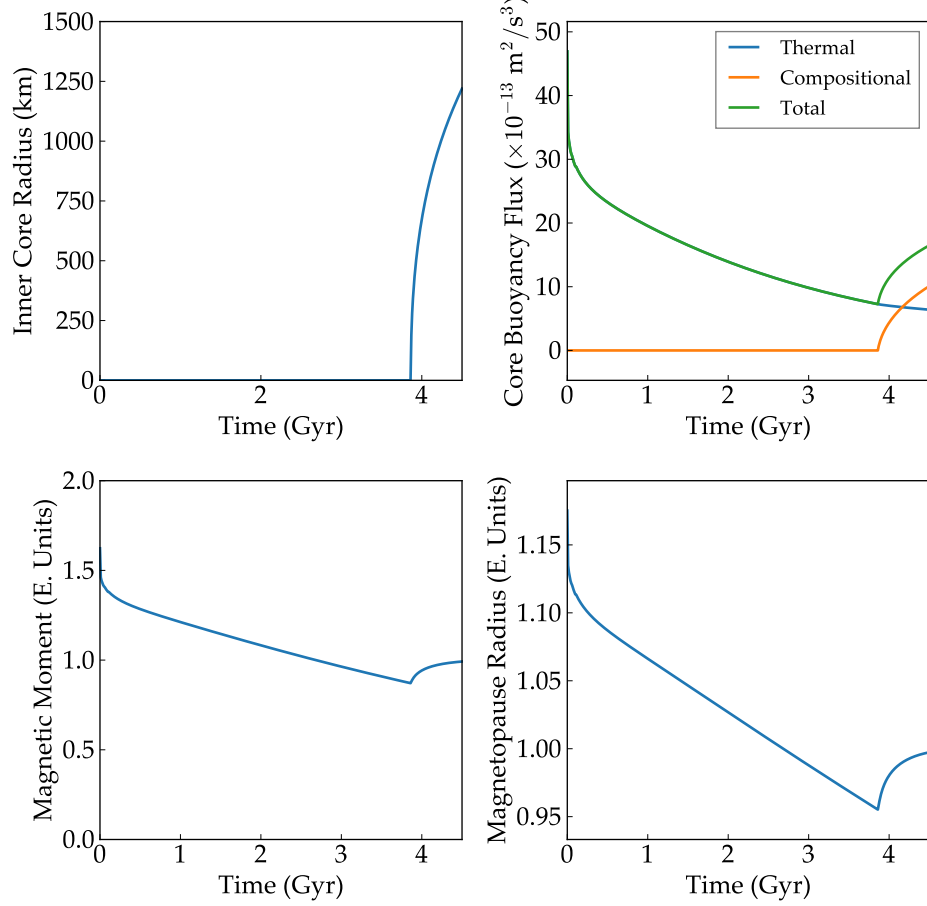


Fig. 16.— Evolution of Earth’s core and magnetic field. [examples/EarthInterior](#)

Huybers & Tziperman (2008) and so the ice accumulation per year is slightly smaller. The ice ablation occurs primarily at the ice edge (around latitude 60°) and is slightly larger than Huybers & Tziperman (2008), but is qualitatively similar.

We note that in this framework, the net growth and retreat of ice sheets is highly sensitive to the tuneable ice deposition rate,  $r_{\text{snow}}$ . With  $r_{\text{snow}}$  too low, we do not build up ice caps on Earth at all. With  $r_{\text{snow}}$  too high, the ice sheets grow so large that they become insensitive to orbital forcing. With  $r_{\text{snow}} \sim 2.25 \times 10^{-5} \text{ kg m}^{-2} \text{ s}^{-1}$ , we roughly reproduce the Earth’s ice age cycles at  $\sim 40,000$  years and  $\sim 100,000$  years over a 10 million year simulation.

There are a number of differences between our reproduction of Milankovitch cycles and those of Huybers & Tziperman (2008). Most notably, our ice sheets tend to persist for

longer periods of time, taking up to three obliquity cycles to fully retreat. We also require a lower ice deposition (snowing) rate than Huybers & Tziperman (2008) in order to ensure a response from the ice sheets to the orbital forcing. We attribute these differences primarily to the difference in energy balance models used for the atmosphere. For example, our model has a single-layer atmosphere with a parameterization of the OLR tuned to Earth, while Huybers & Tziperman (2008) used a multi-layer atmosphere with a simple radiative transfer scheme. Further, while the Huybers & Tziperman (2008) model contained only land, our model has both land and water which cover a fixed fraction of the surface. The primary effect of having an ocean in this model is to change the effective heat capacity of the surface. This dampens the seasonal cycle, and affects the ice sheet growth and retreat. Thus, our seasonal cycle is somewhat muted compared to theirs, and our ice sheets do not grow and retreat as dramatically on orbital time scales. Ultimately, our ice age cycles are more similar to the longer late-Pleistocene cycles than to  $\sim 40,000$  year cycles of the early-Pleistocene.

Even though we cannot perfectly match the results of Huybers & Tziperman (2008), there are two clear reasons why. First, both models make approximations to a number of physical processes and thus have numerous parameters that have to be tuned to reproduce the desired behavior. Second, both models are missing boundary conditions based on the continent distribution of the Earth—continental edges can limit the equator-ward advance of ice sheets or alter the speed of their flow through calving of ice shelves.

#### 14.2. Evolution of Tight Binary Stars

Stars form large and contract until the central pressure become large enough for fusion. For stars in tight binary systems, this size facilitates large tidal torques that rapidly circularize the orbit. In a classic study of the evolution of short-period binary stars, Zahn & Bouchet (1989) found that orbits of binaries with an orbital period of less than about 8 days tidally circularized before they reach the Zero Age Main Sequence (ZAMS), consistent with contemporaneous observations. More recent surveys have found that circularization extends to binary orbital periods of about 10 days (*e.g.*, Meibom & Mathieu 2005; Lurie et al. 2017). Here we reproduce the Zahn & Bouchet result by coupling the stellar evolution models of Baraffe et al. (2015), incorporated in the **STELLAR** module and the equilibrium tide CPL model via **EqTide**. See Sections 7 and 12 and their corresponding Appendices, E and J, respectfully, for a more in-depth discussion of those models.

Adopting the initial conditions used to produce Figure 1 from Zahn & Bouchet (1989), we model an equal mass  $1M_{\odot} - 1M_{\odot}$  binary with initial orbital eccentricity  $e = 0.3$  and an orbital period of 5 days. The initial stellar rotation rate to mean motion ratio is set at

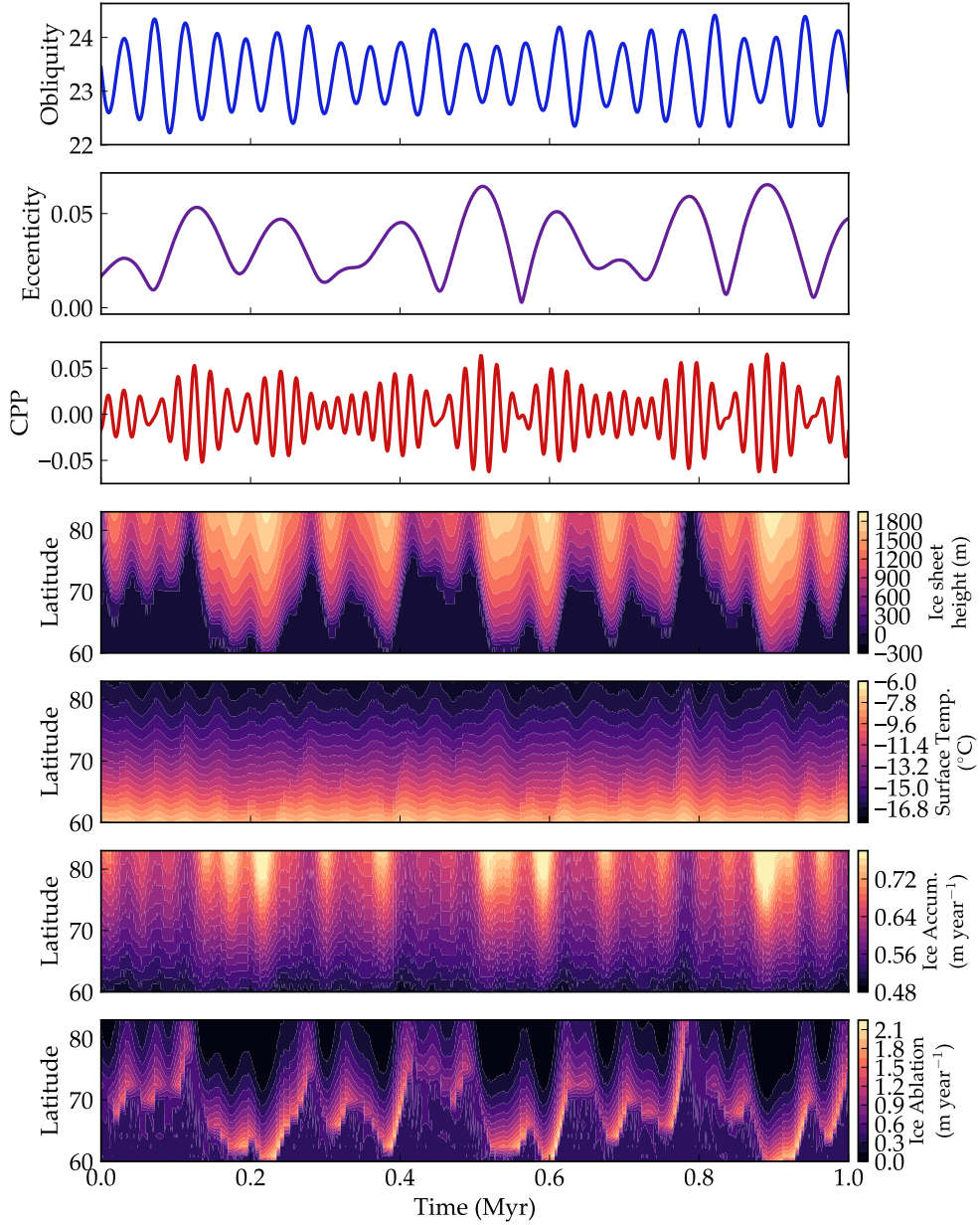


Fig. 17.— Milankovitch cycles on Earth’s northern hemisphere. See Figure 4 of Huybers & Tziperman (2008), for comparison. From top to bottom: obliquity,  $\text{CPP} = e \sin(\varpi + \psi)$ , eccentricity, ice sheet height (m), annually averaged surface temperature ( $^{\circ}\text{C}$ ), annual ice accumulation rate ( $\text{m yr}^{-1}$ ), and annual ice ablation rate ( $\text{m yr}^{-1}$ ). [examples/EarthClimate](#)

$\Omega/n = 3$  in line with the estimates Zahn & Bouchet (1989), who assumed conservation of angular momentum during the star’s accretion phase. Both stellar radii of gyration are fixed at  $r_g = 0.5$ . For our tidal model, we set  $Q = 1.25 \times 10^5$  and  $k_2 = 0.5$ , both reasonable values for stars given the wide range of assumed values in the literature (*e.g.*, Barnes et al. 2013; Fleming et al. 2018).

The results of the simulation are depicted in Figure 15. Our results are in good agreement with Zahn & Bouchet (1989), Fig. 1. After an initial increase in orbital eccentricity, the binary circularizes within the first  $\sim 10^6$  years before the ZAMS. The transition between increasing to decreasing eccentricity occurs when  $e = \sqrt{1/19}$  at the  $\Omega/n = 1.5$  transition, as expected from the CPL model (see Section E.1). The orbital period peaks at around  $10^4$  years and then decreases as the orbit circularizes. One difference between the two model predictions is that Zahn & Bouchet (1989) find an increase in  $\Omega/n$  from unity to over 2 near  $10^6$  years, before the stars tidally lock again after about  $10^9$  years. In our model, the stars remain tidally locked after  $10^5$  years as we force stars with rotation periods close to the orbital period to remain tidally locked to prevent numerical instabilities (see the appendix of Barnes et al. (2013) for a more in-depth discussion of this numerical necessity).

### 14.3. Interiors of Tidally Heated Planets

In this multi-module application we model the gravitational tidal dissipation in the interior of an Earth-like planet and its orbit. The modules used are `ThermInt`, `RadHeat`, and `EqTide`. The tidal dissipation equations used in this application is the “orbit-only” model from Driscoll & Barnes (2015), see also App. E.3, and the dissipation efficiency depends on the temperature of the mantle. To reproduce the results of Driscoll & Barnes (2015) the dissipation efficiency in the orbital equations ( $\dot{e}$  and  $\dot{a}$ ) is approximated by  $Im(k_2) \approx k_2/Q$ , where  $Q = \eta\omega/\mu$  is the Maxwell tidal efficiency.

This example approximately reproduces the results of Driscoll & Barnes (2015) for three tidally evolving planets orbiting a 0.1 solar-mass star. Figures 18 and 19 compare the thermal, magnetic, and orbital evolution of three Earth-like planets each with the same initial eccentricity of 0.5 and initial Semi-major axes of 0.01, 0.02, 0.05 all in AU. Figure 18 reproduces Driscoll & Barnes (2015), Fig. 5 and Fig. 19 reproduces Driscoll & Barnes (2015), Fig. 4.

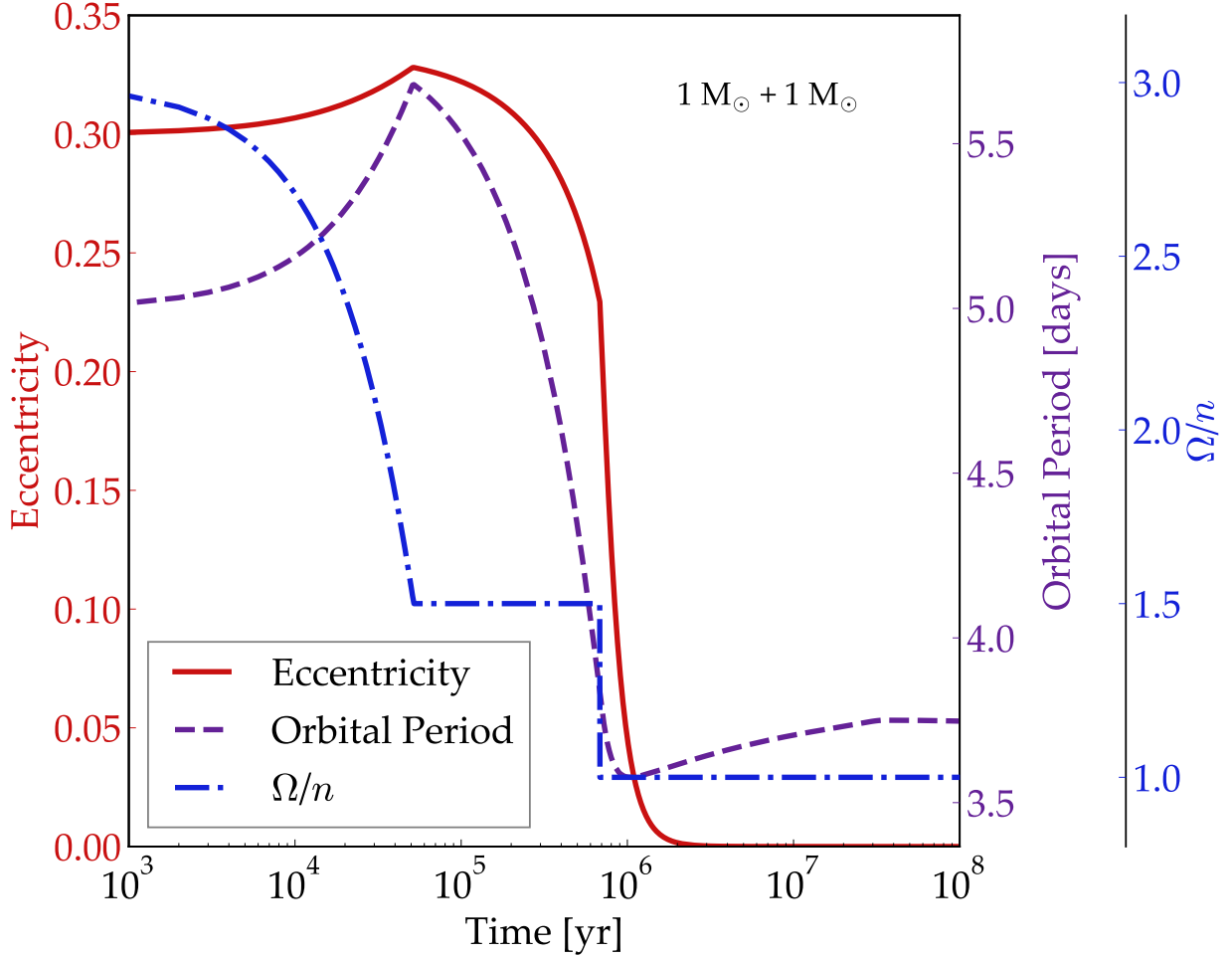


Fig. 15.— Coupled stellar and tidal evolution of a solar twin binary from the pre-main sequence onward calculated in `VPLanet` using the `EqTide` and `STELLAR` modules. Orbital eccentricity evolution is given by the red solid line, the orbital period by the purple dashed line, and the ratio of stellar rotation rate to binary mean motion ( $\Omega/n$ ) evolution is given by the blue dot dashed curve. The binary’s evolution matches with that of an identical system presented in Figure 1 of Zahn & Bouchet (1989). [examples/BinaryTides](#)

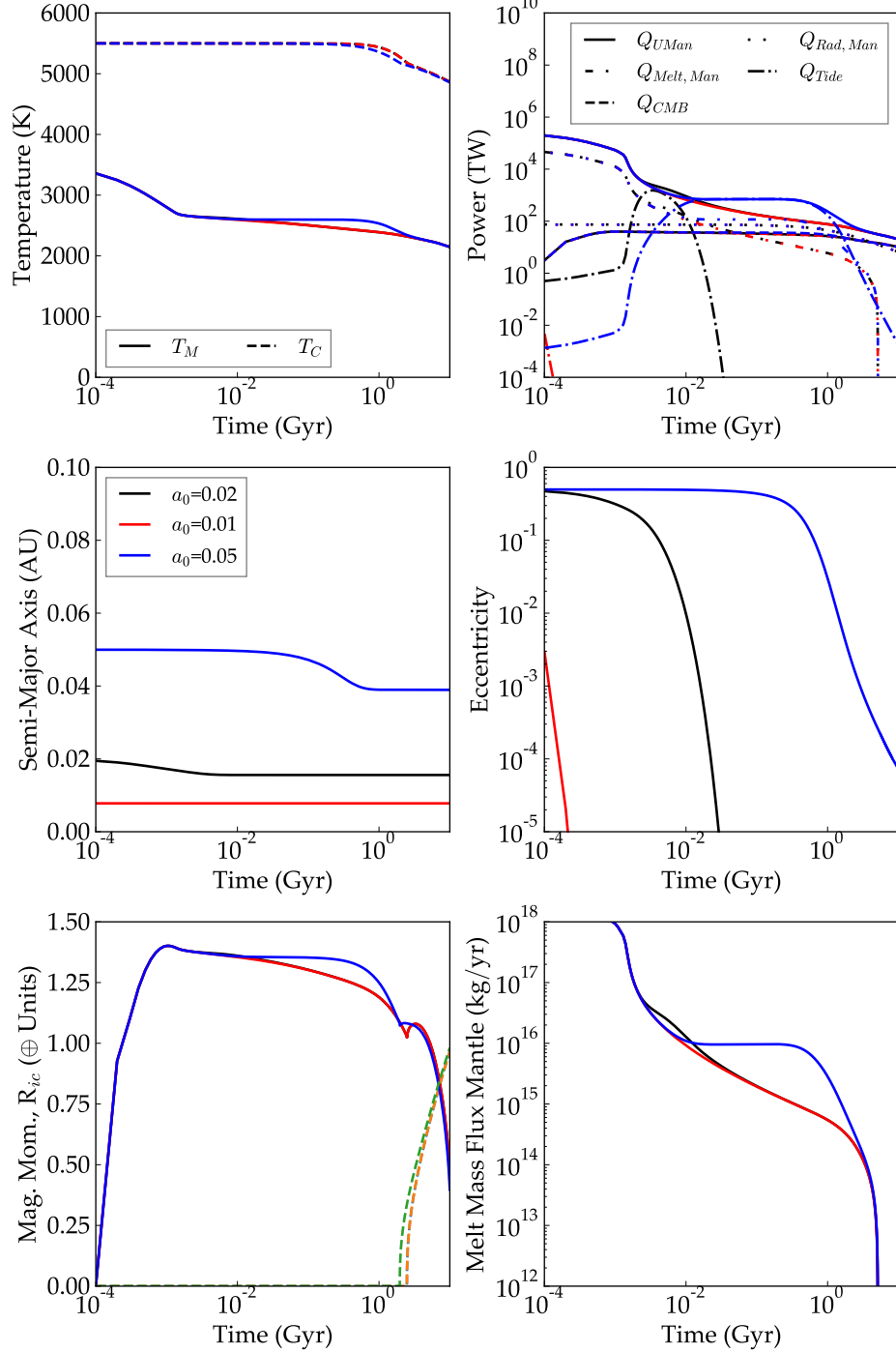


Fig. 18.— Internal evolution of three Earth-like planets orbiting a 0.1 solar-mass star with initial eccentricities of 0.5 and semi-major axes of 0.01 (red), 0.02 (black), and 0.05 (blue). Bottom left panel: Magnetic moment is scaled to Earth’s current value of  $80 \text{ ZAm}^2$  and inner core radius scaled to core-mantle boundary radius  $R_{ic}/R_{cmb}$  is shown as a dashed line.

[examples/TidalEarth](#)

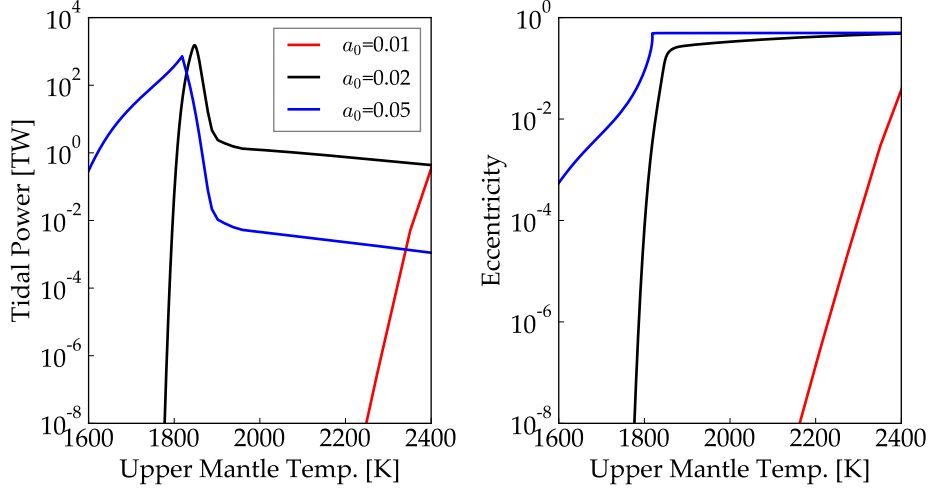


Fig. 19.— Internal properties for the same models as Figure 18 shown here as functions of  $T_{UM}$ . [examples/TidalEarth](#)

#### 14.4. Tidal Damping in Multi-Planet Systems

In multi-planet systems in which one or more planets is close enough to the host star for tides to damp the orbit, orbital and rotational properties can reach an approximately fixed state. Tides remove energy and angular momentum from planetary orbits and rotations. In this subsection, we reproduce the damping of orbital evolution into the “fixed point solution” (Wu & Goldreich 2002; Zhang & Hamilton 2008), and the damping of rotational cycles into a Cassini state (Colombo & Shapiro 1966; Ward & Hamilton 2004; Brasser et al. 2014; Deitrick et al. 2018a).

One difficulty arises from the fact that the semi-major axis decays, and its evolution is not accounted for in `Dist0rb`, which ignores terms involving the mean longitude. The functions,  $f_i$ , in the disturbing function (Table 4) are computationally expensive. In the secular approximation used in `Dist0rb`, the semi-major axes of the planets do not change, thus the  $f_i$  do not change. So when `Dist0rb` is used without `EqTide`, we calculate all of the  $f_i$  values at the start of the simulation and store them in an array. This accelerates the model by over a factor of 100 compared to recalculating  $f_i$  every time step.

However, the tidal forces in `EqTide` do change the semi-major axes, and so when the two models are coupled, we must recalculate  $f_i$ . Rather than recalculate every time step, we additionally store the derivatives,  $df_i/d\alpha$ , and the value of  $\alpha$  (the semi-major axis ratio for each pair of planets) at which  $f_i$  was calculated. Every time step, then, we can calculate the

change in  $\alpha$ , and recalculate  $f_i$  only when

$$\Delta\alpha > \eta f_i \left( \frac{df_i}{d\alpha} \right)^{-1}, \quad (2)$$

where  $\eta$  is a user-defined tolerance factor. The smaller  $\eta$  is, the more accurate the simulation will be, at the expense of computation time.

#### 14.4.1. Apsidal Locking

Multi-planet systems in which one or more planets experience strong tidal damping of  $e$  can reach a so-called “fixed point state” in which the eccentricities stop exchanging angular momentum and the longitudes of periastron circulate with identical frequency (Wu & Goldreich 2002; Rodríguez et al. 2011). In Fig. 20, we use **VPLanet**’s **DistOrb** and **EqTide** modules to reproduce the evolution of  $e$  and  $\varpi$  for the CoRoT-7 system examined by Rodríguez et al. (2011). This figure should be compared to Figs. 2–3 from Rodríguez et al. (2011). We adopted the initial conditions from Rodríguez et al. (2011) and list them in Table 2. We find good agreement between our **VPLanet** results and the original work by Rodríguez et al. (2011).

#### 14.4.2. Cassini States

In this section we consider the damping of a planet’s obliquity into a Cassini state (Colombo & Shapiro 1966; Ward & Hamilton 2004; Winn & Holman 2005; Deitrick et al. 2018a). In a two-planet system, such a configuration occurs when a planet’s orbital and rotational angular momentum vectors remain coplanar with the system’s total angular momentum vector. Such an alignment can occur by chance, but it is far more likely for a world to reach a Cassini state if its obliquity experiences both damping and excitation, *i.e.*, a damped driven configuration. In that case, the obliquity reaches a non-zero equilibrium value, such as the  $\sim 6^\circ$  obliquity of the moon, as first noted by Giovanni Cassini himself.

The physics and mathematics of Cassini states has been discussed at length in the literature, but, briefly, any given three (or more) body system will have Cassini states available to its members. Each member has up to 4 possible Cassini states available, but only up to 2 can be stable. One or more separatrices exist in the phase space, and if damping is present, the stable Cassini states represent attractors.

A Cassini state can be quantitatively identified using the following relations from Ward

Table 1. Properties of Selected Tidally Perturbed Worlds

Parameter	Gl 581	Gl 581 d	Jupiter	Io <sup>a</sup>
$m_p (M_\oplus)$	$1.03 \times 10^5$	5.6	317.828	0.015
$r_p (R_\oplus)$	31.6	1.6	11.209	0.286
$a (R_\oplus)$	-	5123	-	66.13
$e$	-	0.0549	-	0.38
$P$ (d)	94.2	1	0.47	
$\epsilon$ (°)	0	23.5	3.08 <sup>a</sup>	0.0023
$r_g$	0.5	0.628	0.5	0.27
$k_2$	0.5	0.024059	0.3	1.5
$Q$	$10^6$	100	$10^5$	100

<sup>a</sup>[https://ssd.jpl.nasa.gov/?sat\\_phys\\_par](https://ssd.jpl.nasa.gov/?sat_phys_par)

Table 2. CoRoT-7 System Parameters

Parameter	Value
$M_\star [M_\odot]$	0.93
$m_b [M_\oplus]$	8
$m_c [M_\oplus]$	13.6
$a_b, \text{initial}$ [AU]	0.0188
$a_c, \text{initial}$ [AU]	0.0462
$e_b, \text{initial}$	0
$e_c, \text{initial}$	0.2
$Q_b$	100
$Q_c$	100

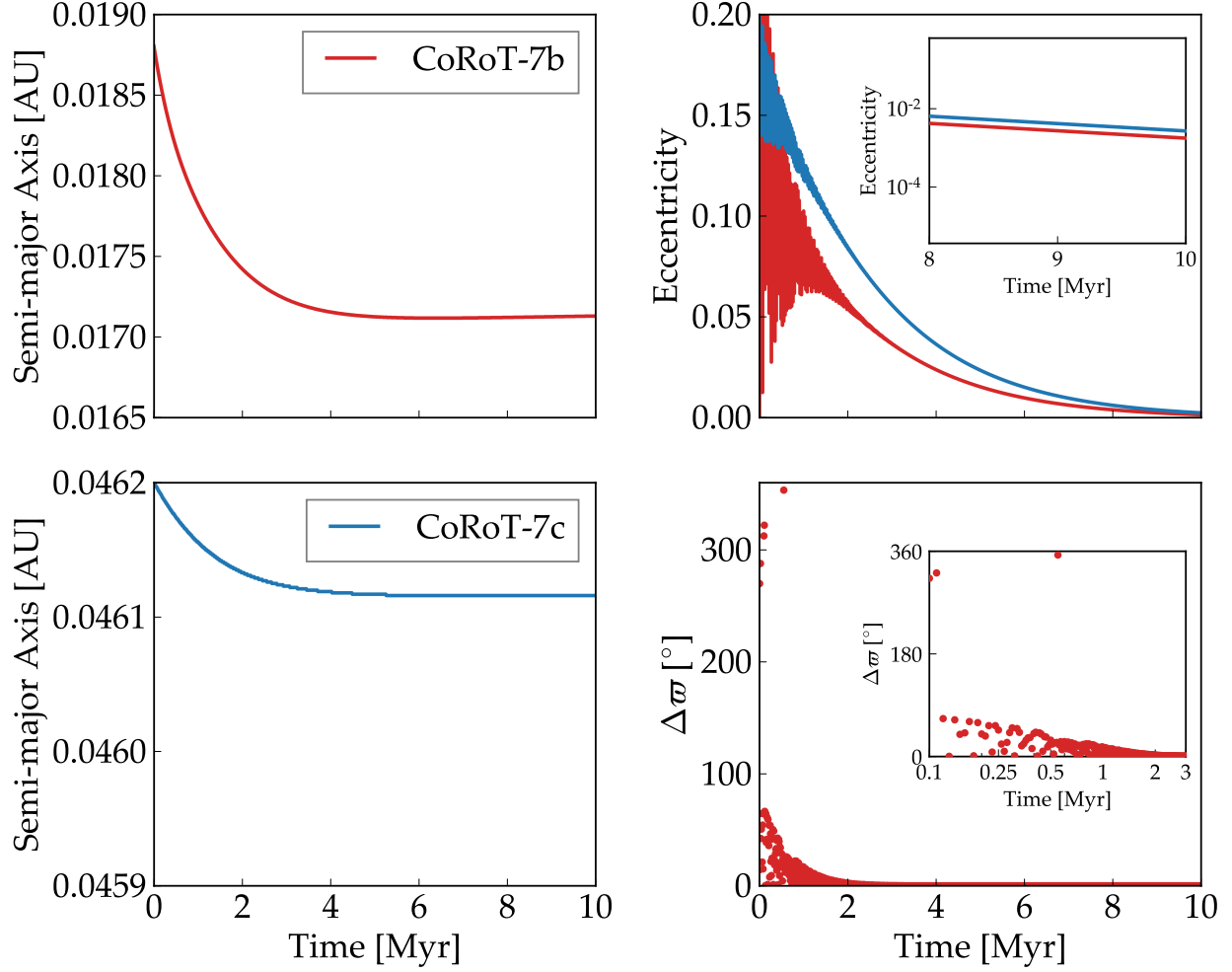


Fig. 20.— Tidally damped orbital evolution of CoRoT-7 b and c as computed by `EqTide` and `DistOrb`. Compare to Figures 2 and 3 from Rodríguez et al. (2011). *Top left:* Semi-major axis evolution of CoRoT-7 b. *Top Right:* Eccentricity evolution for both CoRoT-7b and c. CoRoT-7 b's eccentricity is initially excited by gravitational perturbations from CoRoT-7 c, but eventually damps towards 0 due to tidal forces. The inset shows the slightly non-zero eccentricities for planet b and c decaying towards 0 near the end of the simulation. *Lower left:* Semi-major axis evolution of CoRoT-7 c. *Lower right:* Difference between the longitudes of pericenters of CoRoT-7 b and c,  $\Delta\varpi = \varpi_b - \varpi_c$ . In the inset, we display both planets becoming apsidally locked within 3 Myr due to tidal damping. [examples/ApsideLock](#)

& Hamilton (2004), see also (Deitrick et al. 2018a):

$$\sin \Psi = \left\| \frac{(\mathbf{k} \times \mathbf{n}) \times (\mathbf{s} \times \mathbf{n})}{|\mathbf{k} \times \mathbf{n}| |\mathbf{s} \times \mathbf{n}|} \right\|, \quad (3)$$

where  $\mathbf{k}$ ,  $\mathbf{n}$ , and  $\mathbf{s}$  are the vectors associated with the perpendicular to the appropriate reference plane (the invariable plane or Laplace plane, for example), the angular momentum of the body's orbit, and the angular momentum of the body's rotation. Alternatively, the complimentary relation can be used:

$$\cos \Psi = \frac{(\mathbf{k} \times \mathbf{n}) \cdot (\mathbf{s} \times \mathbf{n})}{|\mathbf{k} \times \mathbf{n}| |\mathbf{s} \times \mathbf{n}|}. \quad (4)$$

A Cassini state occurs when  $\cos \Psi$  and/or  $\sin \Psi$  oscillate about 1, 0, or -1, with the equilibrium value depending on the particular Cassini state.

To demonstrate evolution into a Cassini state, we follow the procedure of Winn & Holman (2005), but consider the planetary system listed in Table 3, and with a stellar mass of  $1M_\odot$ . We use the `EqTide`, `DistOrb`, and `DistRot` modules to perform this experiment. The evolution of the system is shown in Fig. 21 and the obliquity settles into an equilibrium value of  $\sim 48^\circ$ . In this case, we include first order GR corrections, see § C. See Dobrovolskis (2009) for more details on the possible Cassini states of habitable planets.

Fig. 22 shows the phase space of this configuration, as well as the evolution of this test system. Cassini states 1 and 2 are stable, but state 4 is a saddle point and hence is unstable. The gray curves show lines of constant Hamiltonian (Equation 5 in Winn & Holman (2005)) and the black curve shows the separatrix between states 1 and 2. In this case, the system is attracted to Cassini state 2 after  $\sim 500$  kyr.

## 14.5. Evolution of Venus

### 14.5.1. Interior

The interior of Venus is modeled using `ThermInt +RadHeat`, where Venus is approximated have the same total mass as Earth, and assumed to have the same core mass fraction (0.32), radiogenic budget in the mantle (20 TW today) and core (3 TW today), and mantle and core melting curves. The difference between the Venus and Earth models is Venus' mantle is assumed to be in a stagnant lid for 4.5 Gyr reducing the mantle heat flow, and the bulk mantle viscosity and activation energy are assumed to be  $2 \times 10^9 \text{ m}^2 \text{ s}^{-1}$  and  $3.5 \times 10^5 \text{ J mol}^{-1}$ , which is necessary to ensure there is no dynamo today. We note that this model is

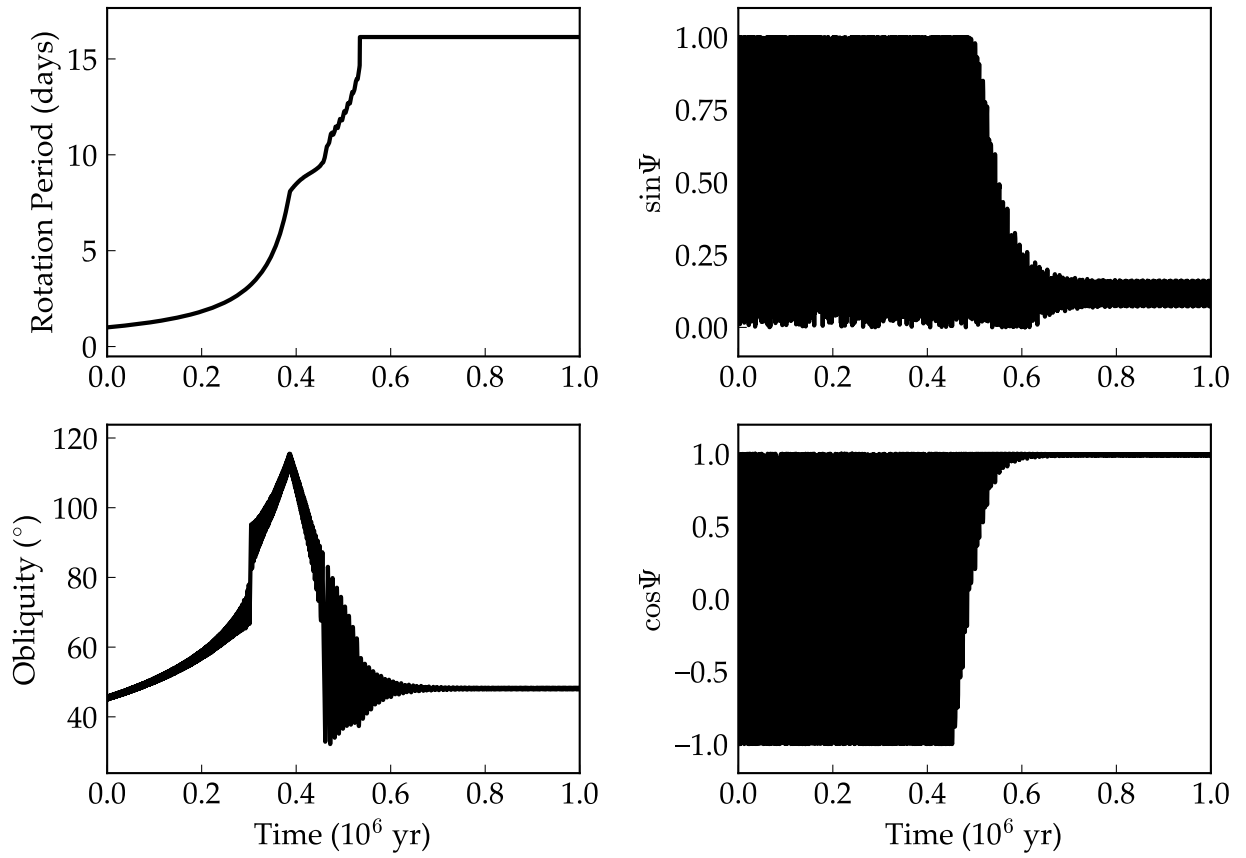


Fig. 21.— An Earth-mass planet damping into Cassini state 2 under the influence of tides and perturbations from an  $18 M_\oplus$  companion planet. This example is constructed to be similar to Fig. 2 of Winn & Holman (2005). [examples/CassiniStates](#)

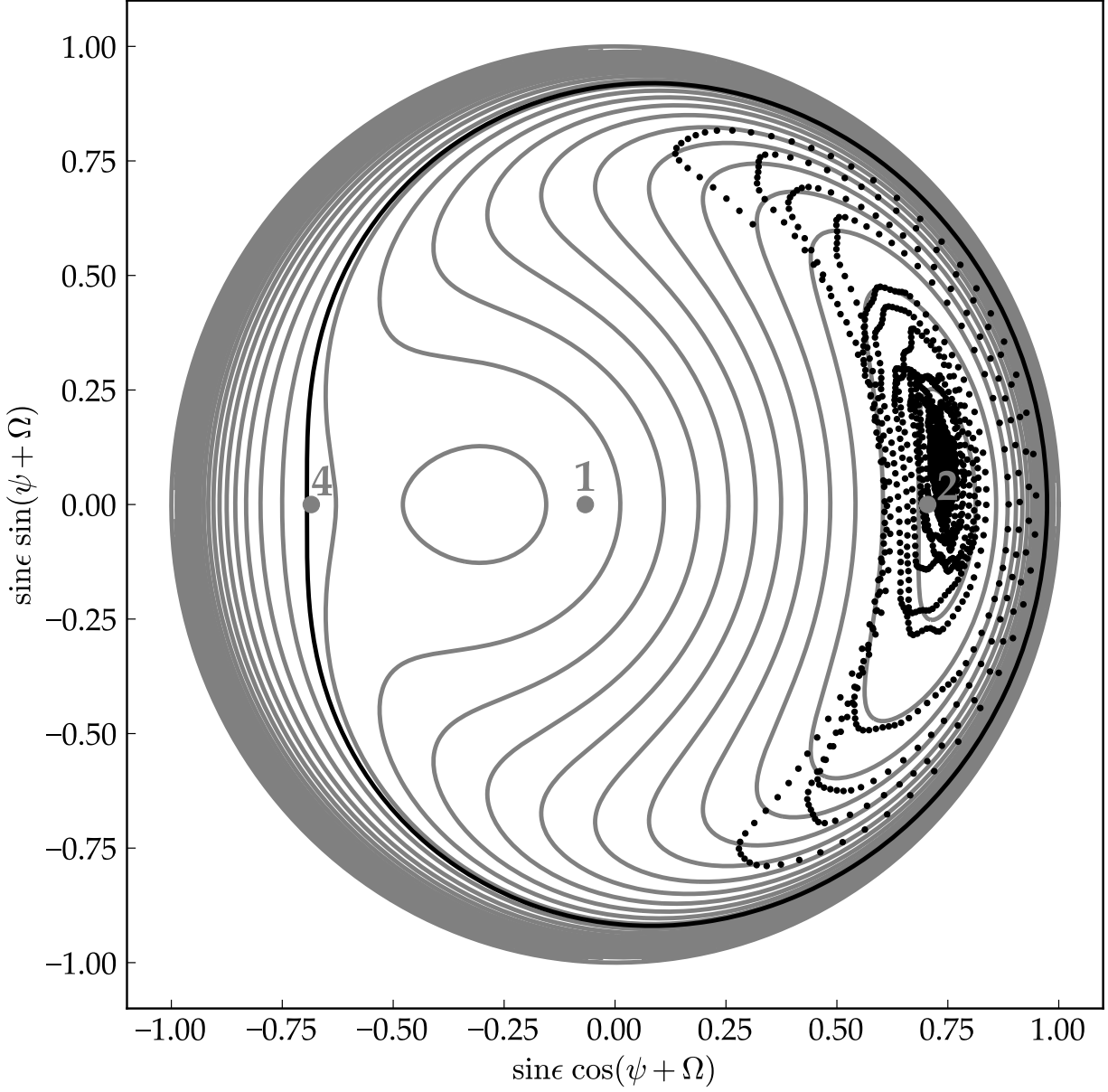


Fig. 22.— Phase space of the three prograde Cassini states (numbered). The gray curves show lines of constant Hamiltonian (Equation 5 in Winn & Holman (2005)) and the black curve shows the separatrix between states 1 and 2. The three possible Cassini states for this system are denoted by the light gray numbers 1, 2, and 4. This case is constructed to be similar to the illustrative case shown in Figure 2 of Winn & Holman (2005), with  $-g/\alpha \sim 0.75$  and  $i = 0.5^\circ$ . The location of the planet's pole after  $\sim 400$  kyr is shown as the black points, with dots separated by 100 years. As the planet's spin is damped by tidal torques, its obliquity sinks into Cassini state 1. [examples/CassiniStates](#)

similar to that in Driscoll & Bercovici (2014), with the main difference here being that the viscosity depends on melt fraction.

Figures 23 and 24 show the thermal evolution of the mantle and core. Due to the isolation of the stagnant lid the core heats up over time and the mantle cools very little, which causes thermal convection and dynamo action to cease in the Venusian core around 3.5 Gyr. These results are very similar to those of (Driscoll & Bercovici 2014, Figs. 5 and 6).

#### 14.5.2. Atmospheric Loss

Venus is widely believed to have once had a substantial surface water inventory (comparable to that of Earth) that was subsequently lost to both thermal and nonthermal escape processes (Watson et al. 1981; Kasting et al. 1984; Kasting 1988; Chassefière 1996a,b; Gillmann et al. 2009). However, the total initial amount of water and the rate at which hydrogen escaped is extremely uncertain, as measurements of D/H fractionation (*e.g.*, Donahue et al. 1982) only place a lower limit on the total amount lost.

Figure 25 shows the evolution of Venus’ water content due to hydrodynamic escape in the first  $\sim$ 200 Myr following its formation, assuming the XUV evolution law of Ribas et al. (2005) and the escape efficiency model of Bolmont et al. (2012). The results in the left panel of Figure 25 are consistent with estimates that Venus may have lost on the order of one to a few terrestrial oceans of water in the first several hundred Myr. The dashed vertical line at  $t = 280$  Myr is the timescale for the loss of 1 TO predicted by Watson et al. (1981). As can be seen from the figure, our model predicts that nearly 5 TO can be lost in that amount of time. This discrepancy is due to two reasons. First, Watson et al. (1981) assumed a constant value of  $\epsilon_{\text{XUV}} \mathcal{F}_{\text{XUV}} \approx 2 \text{ erg/cm}^2/\text{s}$  for Venus, which they computed from estimates of the current XUV flux at Earth and an efficiency  $\epsilon_{\text{XUV}} = 0.15$ . Since then, studies have shown that the XUV flux from the Sun was about two orders of magnitude higher during the first 100 Myr (Ribas et al. 2005), resulting in a much shorter timescale for ocean loss. Second, Watson et al. (1981) did not account for the hydrodynamic drag of oxygen, which strongly damps the net rate of ocean loss during the first several tens of Myr (Luger & Barnes 2015). Together, these effects lead to a timescale for the loss of 1 TO that is approximately 3 times shorter: about 100 Myr.

For reference, the right panel in the Figure shows the amount of photolytically produced oxygen that is retained by the planet, ranging from a few to several hundred bars. The vast majority of this oxygen would have gone into oxidation of the surface.

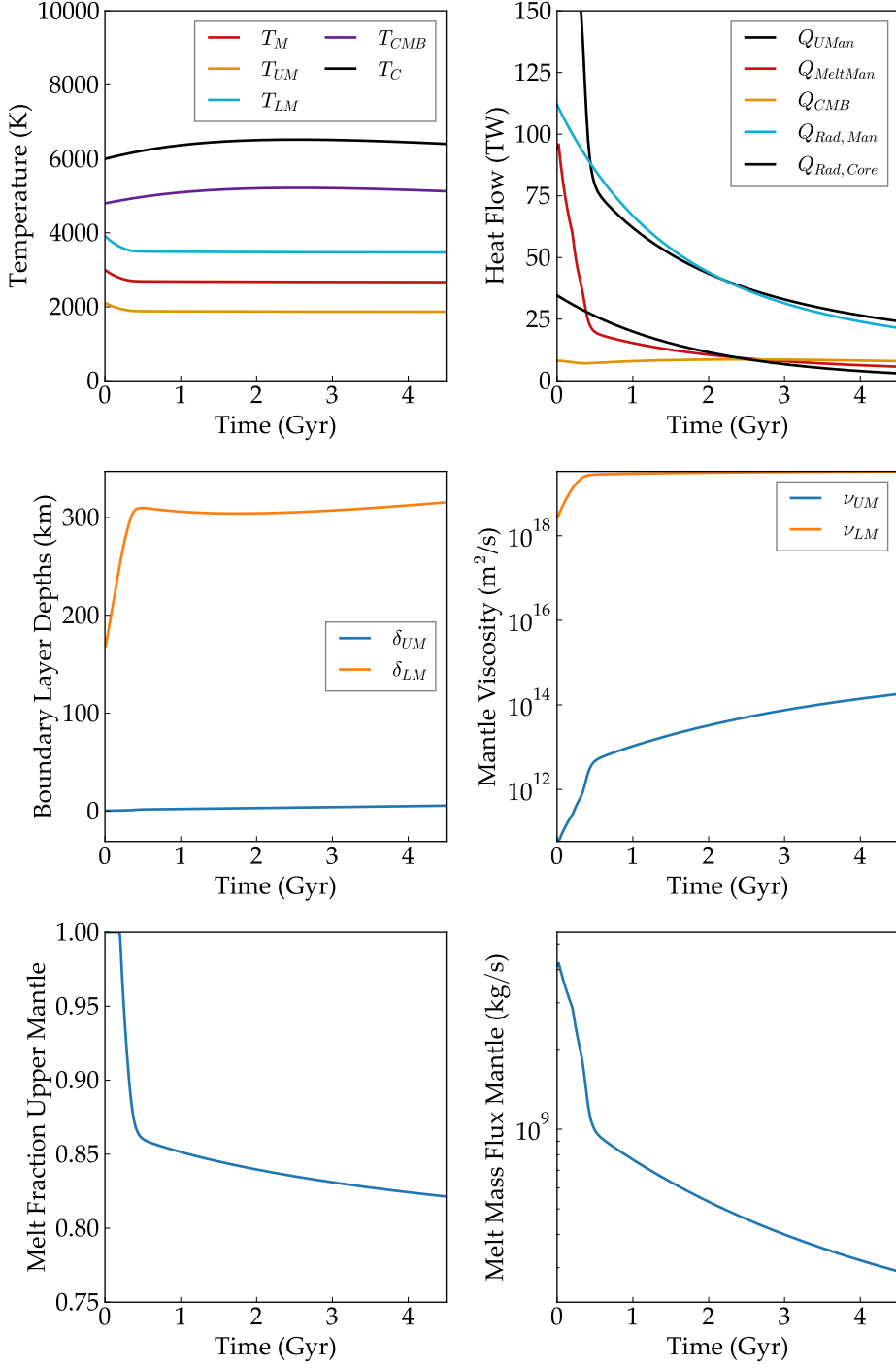


Fig. 23.— Thermal evolution of the Venus interior model. All parameters of the model are the same as the Earth model except the following:  $\nu_r = 2 \times 10^9$ ,  $A_\nu = 3.5 \times 10^5$ ,  $\epsilon_{erupt} = 0$ ,  $Q_{rad,man}^* = 20$  TW, and to account for the stagnant lid  $Q_{conv}$  is multiplied by a factor of 1/25. [examples/VenusInterior](#)

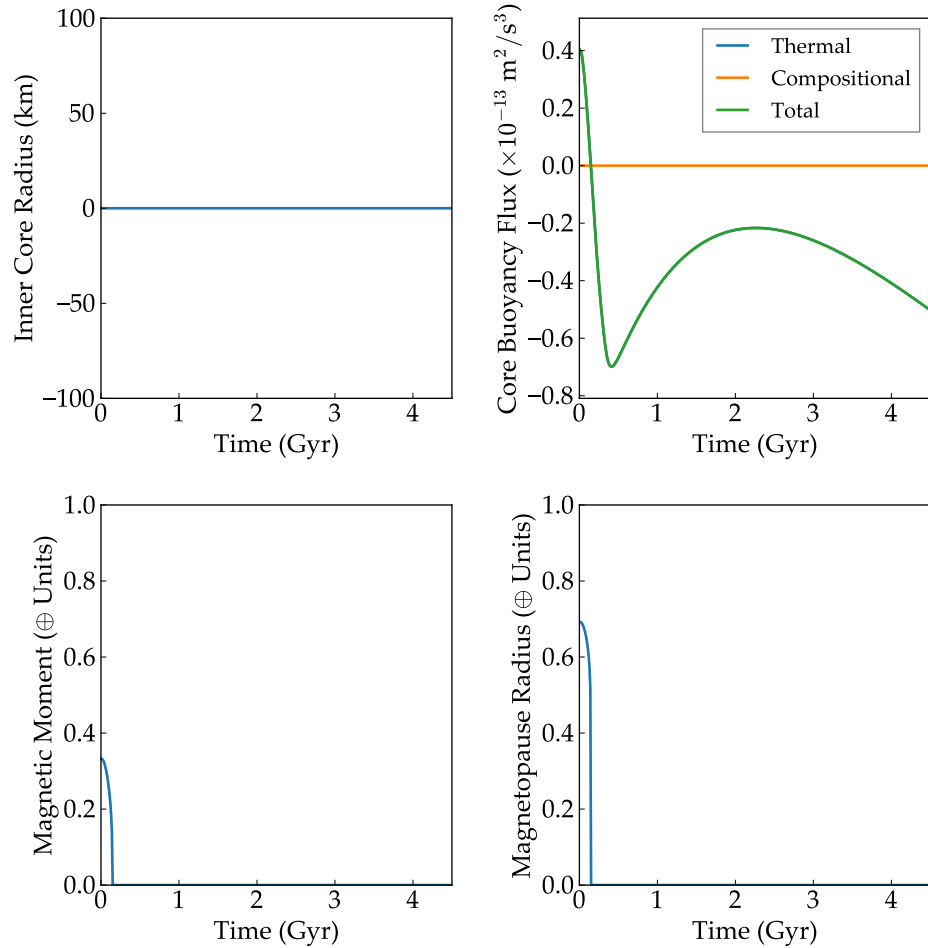


Fig. 24.— Thermal and magnetic evolution of the Venus interior model in Figure 23.  
[examples/VenusInterior](#)

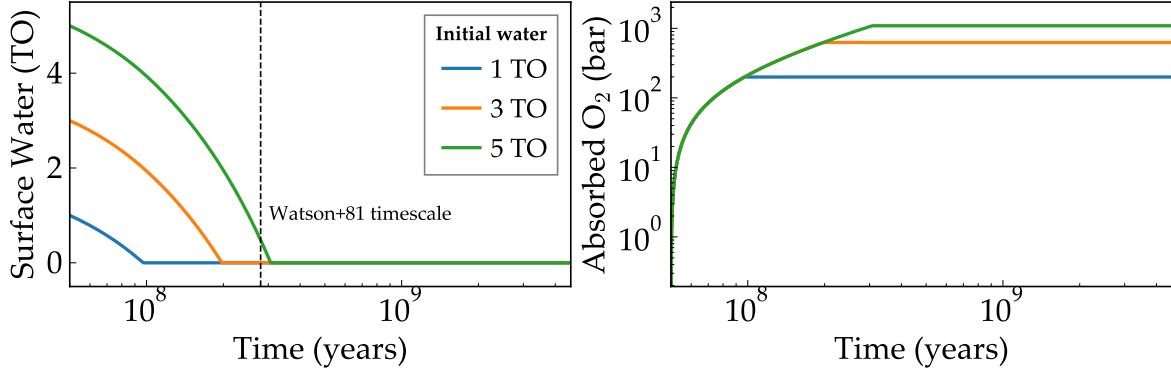


Fig. 25.— Atmospheric escape on Venus as predicted by `vPLanet`. The evolution of the surface water content (left) and the amount of photolytically-produced oxygen absorbed by the surface (right) are plotted for three different initial surface water inventories. For an initial water inventory equal to that of Earth, Venus could have been completely desiccated within the first 100 Myr following its formation. [examples/VenusWaterLoss](#)

#### 14.6. Water Loss During the Pre-Main Sequence

We recover the result that planets near the inner edge of the HZ of low mass M dwarfs can lose one to several oceans of water and produce hundreds to a few thousand bars of atmospheric O<sub>2</sub>. In Figure 26 we reproduce Figure 7 in Luger & Barnes (2015), showing the amount of water lost and the amount of atmospheric oxygen that builds up for a water-rich Earth-mass planet orbiting an M dwarf. Our water loss estimates are somewhat lower than those in Luger & Barnes (2015), primarily because of the lower escape efficiency predicted by the model of Bolmont et al. (2017), which we use here, see App. A. We also account for the increasing mixing ratio of oxygen as water is lost, which acts to slow the escape of hydrogen.

### 15. Discussion and Conclusions

In the previous sections we described the `vPLanet` algorithm, how individual modules reproduce previous results, and how module combinations also reproduce previous results. In conjunction with previous studies that used `vPLanet` to explore new research directions (Deitrick et al. 2018a,b; Fleming et al. 2018; Lincowski et al. 2018; Fleming et al. 2019), we conclude that `vPLanet` is a validated tool for planetary system modeling that can provide new insight into planetary system evolution and planetary habitability.

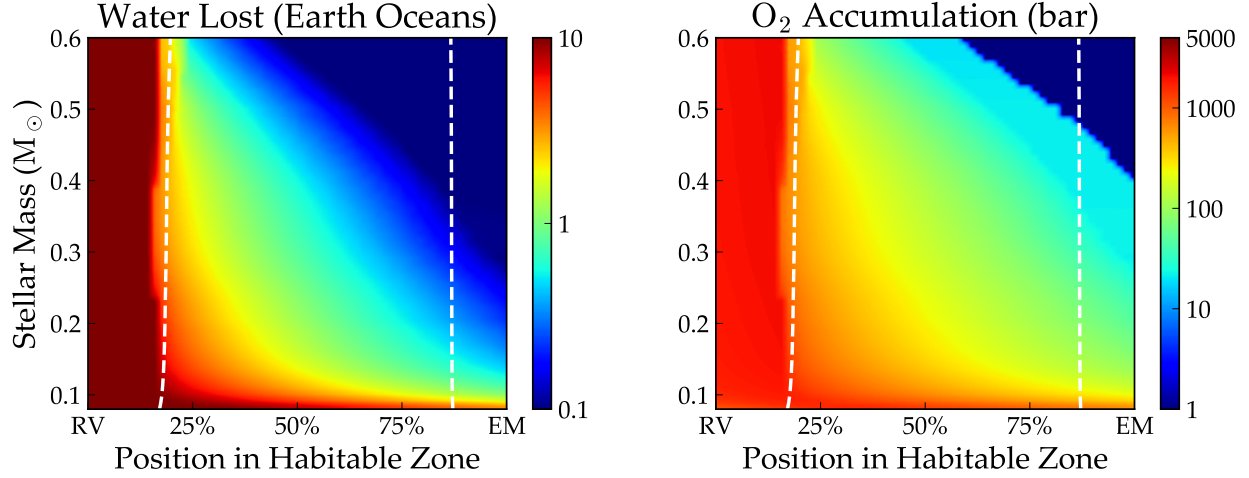


Fig. 26.— Reproduction of Figure 7 in Luger & Barnes (2015) using `vPLanet`. Shown here is the total amount of water lost (left) and the total amount of atmospheric oxygen that builds up (right) due to atmospheric escape on an Earth-mass planet orbiting different mass  $M$  dwarfs (vertical axes) and at different relative positions in the HZ (horizontal axes). The HZ is bounded by the recent Venus (RV) limit at the inner edge and the early Mars (EM) limit at the outer edge; the runaway greenhouse and maximum greenhouse limits are shown as dashed lines. The amount of water lost is somewhat lower than in Luger & Barnes (2015) due primarily to the lower escape efficiency assumed here. [examples/Abiotic02](#)

While the previous sections showed the coupling of many modules, not all module couplings have been tested yet. This situation is partly due to some modules being incompatible, *e.g.*, `DistOrb` and `SpiNBody`, but also due to the shear number of combinations that are possible. Future research can explore more combinations, but at least this first version can reasonably simulate a large number of processes that affect planetary system evolution.

`vPLanet` fills a critical niche in the search for inhabited exoplanets: the simulation of water retention on planets for billions of years. Since astrochemical and planet formation research suggests that many small planets typically do form with large inventories of water and the bioessential elements (*e.g.*, van Dishoeck et al. 2014; Morbidelli et al. 2018), the most pertinent question for potentially habitable planets may not be “do they form with water?” but rather “do they still have water?” By simulating planetary systems completely, `vPLanet` can identify those planets that may retain liquid water in a harsh universe, including phenomena such as the high luminosities of young  $M$  dwarfs (*e.g.*, Luger & Barnes 2015), extreme eccentricity oscillations (Barnes et al. 2015), and dangerous perturbations from passing stars Kaib et al. (2013).

By folding in priors from planet formation simulations, suites of `VPLanet` simulations can, in principle, determine the likelihood that a given planet is habitable today, based on the known properties of its host system. Such an estimate may be key to the prioritization of exoplanets for biosignature searches. Since the constraints are few and the parameter space vast, a proper calculation of the current water abundance will likely require advanced statistical techniques and even machine learning algorithms such as `APPROXPOSTERIOR` (Fleming & VanderPlas 2018). Any `VPLanet` simulation that is consistent with current observations is a viable trajectory of the system, so should such a history permit liquid water on the planet today, then that planet is, by definition, habitable.

In the more distant future, `VPLanet` could be improved to interpret spectral and photometric data that may reveal the presence of extant life on exoplanet. If future versions include the capability to simulate atmospheric structure, photochemistry, geochemistry, and radiative transfer then the outcomes of `VPLanet` simulations could be used to predict and/or interpret the observations of planets in terms of inhabitance. This first version of `VPLanet` focuses on the thermal aspects of planetary system evolution, not the chemical aspects. However, the modular and expandable design of `VPLanet` could permit these calculations in the future, and possibly facilitate the discovery of life beyond the Solar System.

This work was supported by the NASA Astrobiology Institute’s Virtual Planetary Laboratory under Cooperative Agreement number NNA13AA93A. Additional support was provided by NASA grants NNX15AN35G, and 13-13NAI7.0024. DPF is supported by NASA Headquarters under the NASA Earth and Space Science Fellowship Program - Grant 80NSSC17K0482. **ALL: Please place your additional support here.** This work also benefited from participation in the NASA Nexus for Exoplanet Systems Science (NExSS) research coordination network.

### A. The AtmEsc Module

The escape of a planet’s atmosphere to space is an extremely complex process. The rate at which a gaseous species escapes from a planet strongly depends on factors including but not limited to the magnetic properties of the planet and the host star, the space weather the planet is exposed to, the wavelength-dependent irradiation of the planet’s atmosphere, as well as the temperature-pressure profile of the atmosphere and its detailed composition, down to the abundance of trace gases that can act as coolants. Decades of work on solar system bodies have enabled the measurement and modeling of the escape fluxes from the

Earth, Mars, and Venus using complex hydrodynamic and kinetic models (Hunten 1973; Watson et al. 1981; Donahue et al. 1982; Kasting & Pollack 1983; Hunten et al. 1987; Zahnle et al. 1988; Chassefière & Leblanc 2004). For extrasolar planets, however, the situation is drastically different. Even for the most well-studied exoplanets, little is known at present about their bulk properties other than their radii, their instellations, and occasionally their masses. Some constraints have been placed on the bulk atmospheric composition of some hot exoplanets via transit transmission spectroscopy, but even in the most favorable cases, little is known other than the presence or absence of a large hydrogen/helium envelope (*e.g.*, Nortmann et al. 2018; Allart et al. 2019) or loose constraints on the presence of simple molecules such as CO<sub>2</sub> and H<sub>2</sub>O (*e.g.*, Line et al. 2014; MacDonald & Madhusudhan 2019). Stellar activity measurements can yield information about the space weather that some of these exoplanets are exposed to, but the measurement of an exoplanet’s magnetic properties is yet to be made (*e.g.*, Driscoll & Olson 2011; Lynch et al. 2018). On the observation front, hydrogen escape fluxes have been inferred for only a few large, hot exoplanets from Lyman-alpha absorption measurements (*e.g.*, Odert et al. 2019).

However, while precious little is known about the atmospheric escape process from most (individual) exoplanets, recent studies have leveraged the statistical information from the ensemble of all known exoplanets to infer trends in atmospheric escape as a function of planet size and irradiation (Lopez & Rice 2016; Owen & Wu 2017). These studies show that the distribution of radii of hot exoplanets discovered by the *Kepler* mission are well explained, on average, by a surprisingly simple atmospheric escape model, first introduced by Watson et al. (1981). In this *energy-limited* model, the escape from a planetary atmosphere is controlled by the supply of energy to the upper atmosphere by stellar extreme ultraviolet (XUV; 1–1000Å) photons, which are absorbed by hydrogen atoms and converted into kinetic energy. In the simplest form of the model, a fixed fraction  $\epsilon_{\text{XUV}}$  of the incoming XUV energy goes into driving the escape (Watson et al. 1981; Erkaev et al. 2007; Lammer et al. 2013; Volkov & Johnson 2013; Johnson et al. 2013). For a hydrogen-dominated atmosphere, the energy-limited particle escape rate  $F_{\text{EL}}$  is obtained by equating the energy provided by XUV photons to the energy required to lift the atmosphere out of the gravitational potential well:

$$F_{\text{EL}} = \frac{\epsilon_{\text{XUV}} \mathcal{F}_{\text{XUV}} R_p}{4GM_p K_{\text{tide}} m_H}, \quad (\text{A1})$$

where  $\mathcal{F}_{\text{XUV}}$  is the XUV energy flux,  $M_p$  is the mass of the planet,  $R_p$  is the planet radius,  $\epsilon_{\text{XUV}} \approx 0.1$  is the XUV absorption efficiency, and  $K_{\text{tide}}$  is a tidal correction term of order unity (Erkaev et al. 2007). The total escape rate is this quantity integrated over the surface area of the planet, whose effective radius to incoming XUV energy is  $R_{\text{XUV}} \approx R_p$ . For

terrestrial planets, we compute this quantity as

$$R_{XUV} = \frac{R_p^2}{H \ln(p_{XUV}/p_s) + R_p} \quad (\text{A2})$$

(Lehmer & Catling 2017),  $H$  is the atmospheric scale height,  $p_{XUV}$  is the pressure at the effective XUV absorption level, and  $p_s$  is the pressure at the surface.

In the absence of detailed information about the properties of an exoplanet that can control or modulate the atmospheric escape rate, we implement this simple model for atmospheric escape in `VPLanet`, with a few modifications to explicitly model the escape rate from potentially habitable terrestrial planets. Our model closely follows that of Luger et al. (2015) and Luger & Barnes (2015). Here we briefly discuss the principal equations and slight modifications to the models presented in those papers.

In `VPLanet`, we model atmospheric escape from two basic types of atmospheres: hydrogen-dominated atmospheres, such as that of an Earth or super-Earth with a thin primordial hydrogen/helium envelope, and water vapor-dominated atmospheres, such as that of a terrestrial planet in a runaway greenhouse. In the former case, we compute the escape in the energy-limited regime (Equation A1) and assume that the gaseous envelope must fully escape before any other volatiles can be lost to space, given the expected large diffusive separation between light H atoms and other atmospheric constituents. If the envelope is not lost by the time the star reaches the main sequence, we shut off the escape process to account for the transition to ballistic escape predicted by Owen & Mohanty (2016). We model the planet’s radius with the evolutionary tracks for super-Earths of Lopez et al. (2012) and Lopez & Fortney (2014). If an exoplanet loses its H/He envelope, we compute its solid radius using the Sotin et al. (2007) mass-radius relation. The XUV flux is computed from stellar evolution tracks (App. J) and the XUV absorption efficiency parameter  $\epsilon_{XUV}$  is a tunable constant.

In the case of a terrestrial planet with no hydrogen/helium envelope, we assume atmospheric escape only takes place if the total flux incident on the planet exceeds the runaway greenhouse threshold. Typically, the fluxes experienced by planets in or near the habitable zone are not high enough to drive the hydrodynamic escape of the high mean molecular weight bulk atmosphere. Although water vapor can be photolyzed by stellar ultraviolet photons, liberating hydrogen atoms that can go on to escape hydrodynamically, on Earth this process is strongly inhibited by the stratospheric cold trap, which prevents water molecules from reaching the upper atmosphere. However, during a runaway greenhouse, the surface temperature exceeds the temperature of the critical point of water (647 K) and the surface oceans fully evaporate, leading to an upper atmosphere that is dominated by water vapor (*e.g.*, Kasting 1988). As in Luger & Barnes (2015), we use the energy-limited formalism to compute the loss rate of a planet’s surface water via escape of hydrogen to space, with

modifications to allow for the hydrodynamic drag of oxygen by the escaping hydrogen atoms. The total hydrogen particle escape rate is (Luger & Barnes 2015):

$$F_H = \begin{cases} F_{\text{EL}} & \text{if } F_{\text{EL}} < F_{\text{diff}} \\ F_{\text{EL}} \left( 1 + \frac{X_O}{1 - X_O} \frac{m_O}{m_H} \frac{m_c - m_O}{m_c - m_H} \right)^{-1} & \text{if } F_{\text{EL}} \geq F_{\text{diff}}, \end{cases} \quad (\text{A3})$$

where

$$F_{\text{diff}} = \frac{(m_O - m_H)(1 - X_O)b_{\text{diff}}gm_H}{k_{\text{boltz}}T_{\text{flow}}} \quad (\text{A4})$$

is the diffusion-limited flux of oxygen atoms through a background atmosphere of hydrogen and

$$m_c = \frac{1 + \frac{m_O^2}{m_H^2} \frac{X_O}{1 - X_O}}{1 + \frac{m_O}{m_H} \frac{X_O}{1 - X_O}} m_H + \frac{k_{\text{boltz}}T_{\text{flow}}F_H^{\text{ref}}}{\left( 1 + X_O \left( \frac{m_O}{m_H} - 1 \right) \right) b_{\text{diff}}g} \quad (\text{A5})$$

is the *crossover mass*, the largest particle mass that can be dragged upward in the flow. In the expressions above,  $m_H$  and  $m_O$  are the masses of the hydrogen and oxygen atoms, respectively,  $k_{\text{boltz}}$  is the Boltzmann constant,  $T_{\text{flow}} \approx 400\text{K}$  is the temperature of the hydrodynamic flow (Hunten et al. 1987; Chassefière 1996b),  $b_{\text{diff}} = 4.8 \times 10^{17}(T_{\text{flow}}/\text{K})^{0.75}\text{ cm}^{-1}\text{s}^{-1}$  (Zahnle & Kasting 1986) is the binary diffusion coefficient for the two species,  $g$  is the acceleration of gravity, and  $X_O$  is the oxygen molar mixing ratio at the base of the flow, equal to  $\frac{1}{3}$  when the upper atmosphere is water vapor-dominated. As in Tian (2015) and Schaefer et al. (2016), we account for the increasing mixing ratio of oxygen at the base of the hydrodynamic flow, which slows the escape of hydrogen. Tian (2015) finds that as oxygen becomes the dominant species in the upper atmosphere, the Hunten et al. (1987) formalism predicts that an oxygen-dominated flow can rapidly lead to the loss of all  $\text{O}_2$  from planets around M dwarfs. However, hydrodynamic oxygen-dominated escape requires exospheric temperatures  $\sim m_O/m_H = 16$  times higher than that for a hydrogen-dominated flow, which is probably unrealistic for most planets. Following the prescription of Schaefer et al. (2016), we therefore shut off oxygen escape once its mixing ratio exceeds  $X_O = 0.6$ , switching to the diffusion-limited escape rate of hydrogen. Finally, users can either choose a constant value for  $\epsilon_{\text{XUV}}$  or model it as a function of the incoming XUV flux as in Bolmont et al. (2017). In Bolmont et al. (2017), the authors modeled atmospheric loss with a set of 1D radiation-hydrodynamic simulations that allowed them to calculate the XUV escape efficiency,  $\epsilon_{\text{XUV}}$ . In Fig. 27, we show a subset of the range of  $\epsilon_{\text{XUV}}$  values calculated in Bolmont et al. (2017) for some values of stellar XUV flux received by the planet. As **STELLAR** can calculate the star's changing XUV flux over time, the XUV escape efficiency will change over time if set by the Bolmont et al. (2017) model.

Currently, `AtmEsc` does not model the absorption of oxygen by surface sinks, although users can run the code in two limiting cases: efficient surface sinks, corresponding to (say) a reducing magma ocean that immediately absorbs any photolytically produced oxygen; and inefficient surface sinks, corresponding to (say) a fully oxidized surface, leading to atmospheric buildup of O<sub>2</sub> over time. Upcoming modifications to `AtmEsc` will couple it to the geochemical evolution of the planet’s mantle in order to more realistically compute the rate of oxygen buildup in a hydrodynamically escaping atmosphere.

As a word of caution, it is important to reiterate that the energy-limited formalism we adopt in `AtmEsc` is a very approximate description of the escape of an atmosphere to space. The heating of the upper atmosphere that drives hydrodynamic escape is strongly wavelength dependent and varies with both the composition and the temperature structure of the atmosphere, which we do not model. Moreover, line cooling mechanisms such as recombination radiation scale non-linearly with the incident flux. Non-thermal escape processes, such as those controlled by magnetic fields, flares, and/or coronal mass ejections, lead to further departures from the simple one-dimensional energy-limited escape rate. Nevertheless, as we argued above, several studies show that for small planets the escape rate does indeed scale with the stellar XUV flux and inversely with the gravitational potential energy of the gas (*e.g.*, Lopez et al. 2012; Lammer et al. 2013; Owen & Wu 2013, 2017) and that  $\epsilon_{\text{xuv}} \approx 0.1$  is a reasonable median value that predicts the correct escape fluxes within a factor of a few. Since presently we have little information about the atmospheric structure of exoplanets, we choose to employ the energy-limited approximation and fold all of our uncertainty regarding the physics of the escape process into the XUV escape efficiency  $\epsilon_{\text{xuv}}$ .

## B. The BINARY Module

Here we describe the analytic theory for circumbinary orbits of test particles derived by Leung & Lee (2013). We adopt a cylindrical coordinate system centered on the binary center of mass, the system barycenter in this case, and consider the test particles to be massless circumbinary planets (CBPs). Assuming that the binary orbit lies in the  $x - y$  plane, and that the orbit of the CBP is nearly coplanar, Leung & Lee (2013) approximate

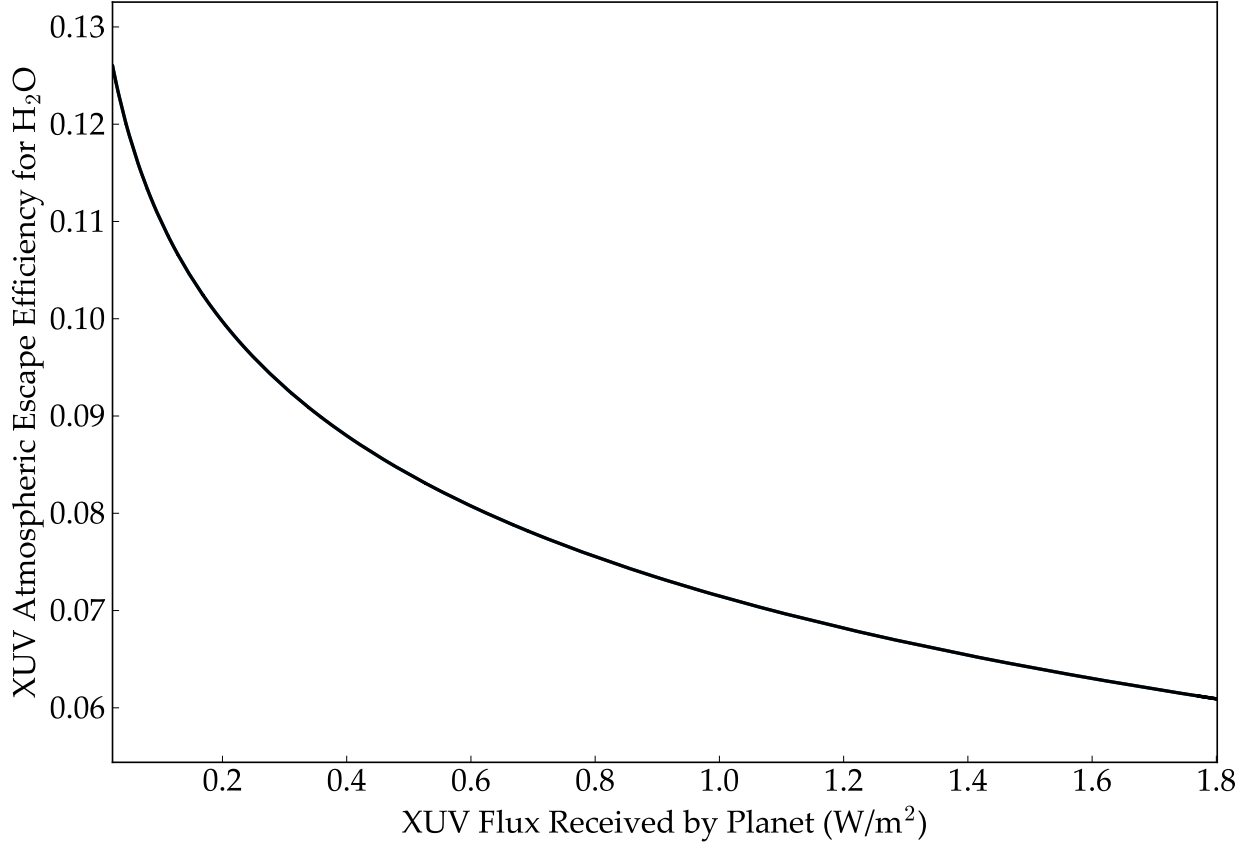


Fig. 27.— Relationship between the XUV escape efficiency parameter  $\epsilon_{\text{xuv}}$  as found by Bolmont et al. (2017). [examples/VenusWaterLoss](#)

the gravitational potential felt by the CBP due to the binary at the position  $(r, \phi, z)$  as

$$\begin{aligned}
 \Phi(r, \phi, z) = & \sum_{k=0}^{\infty} \left[ \Phi_{0k0}(R) - \frac{1}{2} \left( \frac{z}{R} \right)^2 \Phi_{2k0}(R) + \dots \right] \cos k(\phi - M_b - \varpi_B) \\
 & + e_{AB} \sum_{k=0}^{\infty} \left( k \left[ \Phi_{0k0}(R) - \frac{1}{2} \left( \frac{z}{R} \right)^2 \Phi_{2k0}(R) + \dots \right] \right. \\
 & \quad \left. - \frac{1}{2} \left[ \Phi_{0k1}(R) - \frac{1}{2} \left( \frac{z}{R} \right)^2 \Phi_{2k1}(R) + \dots \right] \right) \cos(k(\phi - \varpi_B) - (k+1)M_B) \quad (\text{B1}) \\
 & + e_{AB} \sum_{k=0}^{\infty} \left( -k \left[ \Phi_{0k0}(R) - \frac{1}{2} \left( \frac{z}{R} \right)^2 \Phi_{2k0}(R) + \dots \right] \right. \\
 & \quad \left. - \frac{1}{2} \left[ \Phi_{0k1}(R) - \frac{1}{2} \left( \frac{z}{R} \right)^2 \Phi_{2k1}(R) + \dots \right] \right) \cos(k(\phi - \varpi_B) - (k-1)M_B)
 \end{aligned}$$

for integer  $k$ , binary mean anomaly  $M_b$ , binary orbital eccentricity  $e_{AB}$ , and binary longitude of the periape  $\varpi_B$ . This expression, correct to first order in  $e_{AB}$ , contains the two gravitational potential components from the stars that are in general not axisymmetric. The two components,  $\Phi_{jk0}(R)$  and  $\Phi_{jk1}(R)$ , are given by the following expressions

$$\Phi_{jk0}(R) = -\frac{2-\delta_{k0}}{2} \left[ (-1)^k \frac{m_A}{(m_A + m_B)} b_{(j+1)/2}^k(\alpha_A) + \frac{m_B}{(m_A + m_B)} b_{(j+1)/2}^k(\alpha_B) \right] \frac{G(m_A + m_B)}{R}, \quad (\text{B2})$$

and

$$\Phi_{jk1}(R) = -\frac{2-\delta_{k0}}{2} \left[ (-1)^k \frac{m_A}{(m_A + m_B)} \alpha_A D b_{(j+1)/2}^k(\alpha_A) + \frac{m_B}{(m_A + m_B)} \alpha_B D b_{(j+1)/2}^k(\alpha_B) \right] \frac{G(m_A + m_B)}{R}, \quad (\text{B3})$$

where  $b_{(j+1)/2}^k$  is a Laplace coefficient,  $D = \partial/\partial\alpha$ ,  $m_A$  and  $m_B$  are the masses of the primary and secondary star, respectively,  $G$  is the Universal Gravitational constant, and  $\delta_{k0}$  is the Kroeneker delta function. For a CBP located at cylindrical position  $R$ ,  $\alpha_A$  and  $\alpha_B$  are the normalized semi-major axis of the CBP relative to each star, given by

$$\alpha_i = \frac{a_{AB} m_i}{R(m_A + m_B)}, \quad (\text{B4})$$

where  $a_{AB}$  is the binary orbital semi-major axis and the index  $i$  is  $A$  for the primary and  $B$  for the secondary star, respectively.

Given the approximation for the binary gravitational potential in Eq. (B1),  $\Phi$ , the equations that govern the motion of the CBP in cylindrical coordinates are given by

$$\ddot{R} - R\dot{\phi}^2 = -\frac{\partial\Phi}{\partial R}, R\ddot{\phi} + 2\dot{R}\dot{\phi} = -\frac{1}{R}\frac{\partial\Phi}{\partial\phi}, \ddot{z} = -\frac{\partial\Phi}{\partial z}. \quad (\text{B5})$$

Following Lee & Peale (2006), Leung & Lee (2013) approximate the orbit of the CBP as small epicyclic deviations from the circular motion of the guiding center via

$$R = R_0 + R_1(t), \phi = \phi_0(t) + \phi_1(t), z = z_1(t) \quad (\text{B6})$$

where  $R_0$  is the cylindrical radius of the CBP guiding center in the plane of the binary orbit, 0 subscripts denote the position of the guiding center, and 1 subscripts denote the epicyclic deviations.

The Keplerian mean motion at the radius of the CBP's guiding center is

$$n_k = \sqrt{G(m_A + m_B)/R_0^3} \quad (\text{B7})$$

and the phase angle of the circular motion of the CBP’s guiding center is

$$\phi_0(t) = n_0 t + \psi_0 \quad (\text{B8})$$

for time  $t$  and arbitrary constant phase offset,  $\psi_0$ .

The CBP mean motion is given by

$$n_0^2 = \left[ \frac{1}{R} \frac{d\Phi_{000}}{dR} \right]_{R_0} \quad (\text{B9})$$

where this expression is evaluated at the radius of the guiding center,  $R = R_0$ .

Given these assumptions and definitions, Leung & Lee (2013) solve the equations of motion given in Eq. (B5) to obtain the radial position,  $R$ , of the CBP relative to the binary center of mass, the position of the CBP above or below the orbital plane of the binary,  $z$ , and the phase angle of the CBP,  $\phi$ , over the course of its orbit as an analytic function of time. The CBP’s radial position,  $R$ , is given by the following expression

$$R = R_0 \left( 1 - e_{\text{free}} \cos(\kappa_0 t + \psi) - C_0 \cos M_B - \sum_{k=1}^{\infty} \left[ C_k^0 \cos k(\phi_0 - M_b - \varpi_B) + C_k^+ \cos(k(\phi_0 - \varpi_B) - (k+1)M_b) + C_k^- \cos(k(\phi_0 - \varpi_B) - (k-1)M_b) \right] \right) \quad (\text{B10})$$

where  $e_{\text{free}}$  is the CBP’s free eccentricity, a free parameter of the model, and  $\psi$  is an arbitrary phase offset. Although the summations in Eq. (B10) extend to  $\infty$ , in practice, `VPLanet` truncates the summation  $k = 3$  for computational speed with minimal loss of accuracy.

The variables  $C_0$ ,  $C_k^0$ , and  $C_k^\pm$  represent the approximate radial amplitudes for the forced oscillations due to the non-axisymmetric components of the binary gravitational potential and are given by the following

$$C_0 = -e_{AB} \left[ \frac{d\Phi_{001}}{dR} \right]_{R_0} / [R_0(k_0^2 - n_{AB}^2)], \quad (\text{B11})$$

$$C_k^0 = \left[ \frac{d\Phi_{0k0}}{dR} + \frac{2n\Phi_{0k0}}{R(n - n_{AB})} \right]_{R_0} / (R_0[\kappa_0^2 - k^2(n_0 - n_{AB})^2]), \quad (\text{B12})$$

and

$$C_k^\pm = e_{AB} \left[ \pm k \frac{d\Phi_{0k0}}{dR} - \frac{d\Phi_{0k1}}{2dR} + \frac{kn(\pm 2k\Phi_{0k0} - \Phi_{0k1})}{R(kn - (k \pm 1)n_{AB})} \right]_{R_0} / (R_0[\kappa_0^2 - (kn_0 - (k \pm 1)n_{AB})^2]). \quad (\text{B13})$$

In these expressions,  $k_0$  is the epicyclic frequency and is given by

$$\kappa_0^2 = \left[ R \frac{dn^2}{dR} + 4n^2 \right]_{R_0} \quad (\text{B14})$$

for CBP mean motion,  $n$  given by Eq. (B9), and is evaluated at CBP radial position  $R = R_0$ .

The CBP cylindrical phase angle is

$$\begin{aligned} \phi = n_0 t + \phi_0 + \frac{2n_0}{\kappa_0} e_{\text{free}} \sin(\kappa_0 t + \psi) + \frac{n_0}{n_{AB}} D_0 \sin M_b \sum_{k=1}^{\infty} & \left[ \frac{n_0}{k(n_0 - n_{AB})} D_k^0 \sin k(\phi_0 - M_b - \varpi_B) \right. \\ & \left. + \frac{n_0}{kn_0 - (k+1)n_{AB}} D_k^+ \sin(k(\phi_0 - \varpi_B) - (k+1)M_b) + \frac{n_0}{kn_0 - (k-1)n_{AB}} D_k^- \sin(k(\phi_0 - \varpi) - (k-1)M_b) \right] \end{aligned} \quad (\text{B15})$$

where  $\varphi$  is an arbitrary phase offset and the variables  $D_0$ ,  $D_k^0$ , and  $D_k^\pm$  are given by

$$D_0 = 2C_0, \quad (\text{B16})$$

$$D_k^0 = 2C_k^0 - \left[ \frac{\Phi_{0k0}}{R^2 n(n - n_{AB})} \right]_{R_0}, \quad (\text{B17})$$

and

$$D_k^\pm = 2C_k^\pm - e_{AB} \left[ \frac{k(\pm 2k\Phi_{0k0} - \Phi_{0k1})}{2R^2 n(kn - (k \pm 1)n_{AB})} \right]_{R_0}. \quad (\text{B18})$$

The cylindrical position of the CBP above or below the plane of the binary,  $z$ , is decoupled from the epicyclic motion of the CBP orbital radius and phase angle and is simply

$$z = R_0 i_{\text{free}} \cos(\nu_0 t + \zeta), \quad (\text{B19})$$

where  $\zeta$  is an arbitrary phase offset and  $i_{\text{free}}$  is the free inclination, a free parameter of the model. The vertical frequency  $\nu_0$  is given by

$$\nu_0^2 = \left[ -\frac{\Phi_{200}}{R^2} \right]_{R_0}. \quad (\text{B20})$$

### C. The `DistOrb` Module

Our model for the orbital evolution, called `DistOrb` (for “Disturbing function Orbits”), uses the literal, 4th order disturbing function developed in Murray & Dermott (1999) and

Ellis & Murray (2000). We use only the secular terms, meaning that the rapidly varying terms that depend on the mean longitudes of the planets are ignored on the assumption that these terms will average to zero over long timescales. This assumption is valid as long as no planets are in proximity of mean-motion resonances.

There are two orbital models in `Dist0rb`: the first is simply a direct Runge-Kutta integration of the fourth-order equations of motion; the second is the Laplace-Lagrange eigenvalue solution, which reduces the accuracy in the disturbing function to second-order, but returns a solution that is explicit in time, and thus provides a solution in much less computation time. The fourth-order solution tends to produce results that match better with N-body; however, the Laplace-Lagrange solution can be a powerful predictive tool because it provides secular frequencies directly. One example of the use of such frequencies is in the prediction of Cassini states, as shown in § 14.4.2 (see also Ward & Hamilton 2004; Brasser et al. 2014; Deitrick et al. 2018a).

The equations of motion are Lagrange’s equations (see Murray & Dermott 1999). In the secular approximation the equations for semi-major axis and mean longitude, and any disturbing function derivative with respect to these variables, are ignored. Additionally, to avoid singularities in the equations for the longitudes of pericenter and ascending node, which occur at zero eccentricity and inclination, respectively, we rewrite Lagrange’s equations and the disturbing function in terms of the variables (a form of Poincaré coordinates):

$$h = e \sin \varpi \quad (C1)$$

$$k = e \cos \varpi \quad (C2)$$

$$p = \sin \frac{i}{2} \sin \Omega \quad (C3)$$

$$q = \sin \frac{i}{2} \cos \Omega, \quad (C4)$$

where  $e$  is the orbital eccentricity,  $i$  is the inclination,  $\Omega$  is the longitude of ascending node, and  $\varpi = \omega + \Omega$  is the longitude of periastron (see Figure 28).

Lagrange's equations for secular theory are then:

$$\begin{aligned} \frac{dh}{dt} &= \frac{\sqrt{1-e^2}}{na^2} \frac{\partial \mathcal{R}}{\partial k} + \frac{kp}{2na^2\sqrt{1-e^2}} \frac{\partial \mathcal{R}}{\partial p} \\ &\quad + \frac{kq}{2na^2\sqrt{1-e^2}} \frac{\partial \mathcal{R}}{\partial q} \end{aligned} \quad (\text{C5})$$

$$\begin{aligned} \frac{dk}{dt} &= -\frac{\sqrt{1-e^2}}{na^2} \frac{\partial \mathcal{R}}{\partial h} - \frac{hp}{2na^2\sqrt{1-e^2}} \frac{\partial \mathcal{R}}{\partial p} \\ &\quad - \frac{hq}{2na^2\sqrt{1-e^2}} \frac{\partial \mathcal{R}}{\partial q} \end{aligned} \quad (\text{C6})$$

$$\begin{aligned} \frac{dp}{dt} &= -\frac{kp}{2na^2\sqrt{1-e^2}} \frac{\partial \mathcal{R}}{\partial h} + \frac{hp}{2na^2\sqrt{1-e^2}} \frac{\partial \mathcal{R}}{\partial k} \\ &\quad + \frac{1}{4na^2\sqrt{1-e^2}} \frac{\partial \mathcal{R}}{\partial q} \end{aligned} \quad (\text{C7})$$

$$\begin{aligned} \frac{dq}{dt} &= -\frac{kq}{2na^2\sqrt{1-e^2}} \frac{\partial \mathcal{R}}{\partial h} + \frac{hq}{2na^2\sqrt{1-e^2}} \frac{\partial \mathcal{R}}{\partial k} \\ &\quad - \frac{1}{4na^2\sqrt{1-e^2}} \frac{\partial \mathcal{R}}{\partial p}, \end{aligned} \quad (\text{C8})$$

where  $\mathcal{R}$  is the disturbing function, and  $a$ ,  $n$ , and  $e$  are the semi-major axis, mean motion, and eccentricity, respectively. See Berger & Loutre (1991) for the complete set of Lagrange's equations in  $h$ ,  $k$ ,  $p$ , and  $q$ , including mean-motion (*i.e.*, resonant) effects.

General relativity is known to affect the apsidal precession (associated with eccentricity) of planetary orbits, so we include a correction to Equations (C5) and (C6). Following Laskar (1986), the apsidal corrections are:

$$\frac{dh}{dt} \Big|_{GR} = \delta_R k \quad (\text{C9})$$

$$\frac{dk}{dt} \Big|_{GR} = -\delta_R h, \quad (\text{C10})$$

where

$$\delta_R = \frac{3n^3a^2}{c^2(1-e^2)}, \quad (\text{C11})$$

and  $c$  is the speed of light.

The secular approximation allows us to take large time-steps (years to hundreds of years) and thus to run thousands of simulations quickly and explore parameter space with relatively minimal computer usage compared with N-body models.

For systems well away from mean-motion resonances, `Dist0rb` does a reasonable job at modeling the orbital evolution, up to eccentricities of  $\sim 0.4$  or mutual inclinations of  $\sim 35^\circ$ .

See Deitrick et al. (2018a) for further comparisons. However, as noted in Murray & Dermott (1999), one of the series expansions used in deriving the disturbing function diverges at  $e = 0.6627434$ . If the eccentricity of a planet ever exceeds this value, `DistOrb` immediately halts. In this case, the user will need to switch to an N-body integrator such as `SpinBody`, or another N-body code, which can still be coupled to `DistRot` and `POISE` if desired.

Because planetary systems have a large number of parameters (masses, number of planets, eccentricities, inclinations, etc.), the full limitations of `DistOrb` are difficult to map. Thus we advise users to always compare a small selection of cases with an N-body model, to understand `DistOrb`'s applicability to the desired planetary system.

Finally we present, for the sake of completeness, the disturbing function as used in `DistOrb`, in the variables  $h, k, p$ , and  $q$  (Table 4). These were originally derived by Ellis & Murray (2000); we have simply applied coordinate transformations and calculated derivatives with respect to the new coordinates. This disturbing function, in its original form, can also be seen in Murray & Dermott (1999). We will not restate the semi-major axis functions,  $f_1, f_2, f_3$  and so on, in this paper, as they are taken directly from Table B.3 of Murray & Dermott (1999).

The secular disturbing function, for any pair of planets, is:

$$\mathcal{R} = \frac{\mu'}{a'} \mathcal{R}_D, \quad (\text{C12})$$

for the inner body, and

$$\mathcal{R}' = \frac{\mu}{a'} \mathcal{R}_D, \quad (\text{C13})$$

for the outer body. Here,  $a'$  is the semi-major axis of the exterior planet and the mass factors are  $\mu = \kappa^2 m$  and  $\mu' = \kappa^2 m'$ , where  $m$  is the mass of the interior planet,  $m'$  is the mass of the exterior planet, and  $\kappa$  is Gauss' gravitational constant. Finally,

$$\mathcal{R}_D = D0.1 + D0.2 + D0.3 + \dots, \quad (\text{C14})$$

where the terms D0.1, D0.2, and so on, are given in Table 4.

#### D. The `DistRot` Module

The rotational axis model, `DistRot` (for “Disturbing function Rotation”), is derived from the Hamiltonian for rigid body motion introduced by Kinoshita (1975, 1977) and has been used extensively (*e.g.*, Laskar 1986; Laskar et al. 1993; Armstrong et al. 2004, 2014). In the

absence of large satellites (such as the Moon), the equations of motion for a rigid planet are:

$$\frac{d\psi}{dt} = R(\varepsilon) - \cot(\varepsilon) [A(p, q) \sin \psi + B(p, q) \cos \psi] - 2\Gamma(p, q) - p_g \quad (\text{D1})$$

$$\frac{d\varepsilon}{dt} = -B(p, q) \sin \psi + A(p, q) \cos \psi, \quad (\text{D2})$$

where  $\psi$  is the “precession angle” (see Figure 28 and the following paragraph),  $\varepsilon$  is the obliquity, and,

$$R(\varepsilon) = \frac{3\kappa^2 M_\star J_2 Mr^2}{a^3 \nu} \frac{C}{S_0} \cos \varepsilon \quad (\text{D3})$$

$$S_0 = \frac{1}{2}(1 - e^2)^{-3/2} \quad (\text{D4})$$

$$A(p, q) = \frac{2}{\sqrt{1 - p^2 - q^2}} [\dot{q} + p\Gamma(p, q)] \quad (\text{D5})$$

$$B(p, q) = \frac{2}{\sqrt{1 - p^2 - q^2}} [\dot{p} - q\Gamma(p, q)] \quad (\text{D6})$$

$$\Gamma(p, q) = q\dot{p} - p\dot{q}. \quad (\text{D7})$$

Note the sign error in Equation (8) of Armstrong et al. (2014), corrected in our Equation (D5). Our Equation (D3) does not contain the lunar constants present in Eq. (24) of Laskar (1986). Here,  $\varepsilon$  represents the obliquity,  $p$  and  $q$  are from Eqs. (C3) and (C4),  $\dot{p}$  and  $\dot{q}$  are their time derivatives (Equations (C7) and (C8)),  $\kappa$  is the Gaussian gravitational constant,  $M_\star$  is the mass of the host star in solar units,  $\nu$  is the rotation frequency of the planet in rad day<sup>-1</sup>,  $CM^{-1}r^{-2}$  is the specific polar moment of inertia of the planet, and  $J_2$  is the gravitational quadrupole of the (oblate) planet. The final term in Equation (D1),  $p_g$ , accounts for precession due to general relativity and is equal to  $\delta_R/2$  (Barker & O’Connell 1970). **What is  $\delta_R/2$ ?**

The symbol  $\psi$  refers to the precession angle, defined as  $\psi = \Lambda - \Omega$ , where  $\Lambda$  is the angle between the vernal point  $\Upsilon$ , the position of the sun/host star at the planet’s northern spring equinox, and the location of the ascending node,  $\Omega$ , measured from some reference direction  $\Upsilon_0$  (often taken to be the direction of the vernal point at some reference date, hence the use of the symbol  $\Upsilon^1$ ), see Figure 28. The convention of defining  $\Upsilon$  as the location of the sun at northern spring equinox is sensible for the solar system since we observe from Earth’s surface,

---

<sup>1</sup>The vernal point occurred in the constellation Aries during Ptolemy’s time, thus it is also called the “first point of Aries” and the “ram’s horn” symbol is used.

however, it is a confusing definition to use for exoplanets, for which the direction of the rotation axis is unknown. We adhere to the convention for the sake of consistency with prior literature. In the coming decades, it may become possible to determine the obliquity and orientation of an exoplanet’s spin axis; in that event, care should be taken in determining the initial  $\psi$  for obliquity modeling. One can equivalently refer to  $\Upsilon$  as the position of the planet at its northern spring equinox  $\pm 180^\circ$ . The relevant quantity for determining the instellation, however, is the angle between periastron and the spring equinox,  $\omega + \Lambda = \varpi + \psi$ .

An additional complication for obliquity evolution is, of course, the presence of a large moon. We do not include the component of the Kinoshita (1975) model that accounts for the lunar torque because the coefficients used are specific to the Earth-Moon-Sun three body problem and were calculated from the Moon’s orbital evolution (and are therefore not easily generalized). However, in `DistRot` we can approximate the effect of the Moon by *forcing* the precession rate, Eq. (D3), to be equal to the observed terrestrial value. The effect of this is shown in Figure 7.

Equation (D1) for the precession angle contains a singularity at  $\varepsilon = 0$ . To avoid numerical instability, we instead recast Equations (D1) and (D2) in terms of the rectangular coordinates:

$$\xi = \sin \varepsilon \sin \psi \quad (\text{D8})$$

$$\zeta = \sin \varepsilon \cos \psi \quad (\text{D9})$$

$$\chi = \cos \varepsilon. \quad (\text{D10})$$

The third coordinate,  $\chi$ , is necessary to preserve sign information when the obliquity crosses  $90^\circ$  (see Laskar et al. 1993). The equations of motion for these variables are then:

$$\frac{d\xi}{dt} = -B(p, q) \sqrt{1 - \xi^2 - \zeta^2} + \zeta[R(\varepsilon) - 2\Gamma(p, q) - p_g] \quad (\text{D11})$$

$$\frac{d\zeta}{dt} = A(p, q) \sqrt{1 - \xi^2 - \zeta^2} - \xi[R(\varepsilon) - 2\Gamma(p, q) - p_g] \quad (\text{D12})$$

$$\frac{d\chi}{dt} = \xi B(p, q) - \zeta A(p, q). \quad (\text{D13})$$

The value of  $J_2$  is a function of the planet’s rotation rate and density structure. In hydrostatic equilibrium, the Darwin-Radau relation (Cook 1980; Murray & Dermott 1999) shows that the planet’s gravitational quadrupole moment,  $J_2$ , scales with the rotation rate squared. Earth is very close to hydrostatic equilibrium, while Mars and the Moon are not. In `DistRot`, we give the option to assume that planets are in hydrostatic equilibrium, and scale  $J_2$  according to:

$$J_2 = J_{2\oplus} \left( \frac{\nu}{\nu_\oplus} \right)^2 \left( \frac{r}{R_\oplus} \right)^3 \left( \frac{M}{M_\oplus} \right)^{-1}, \quad (\text{D14})$$

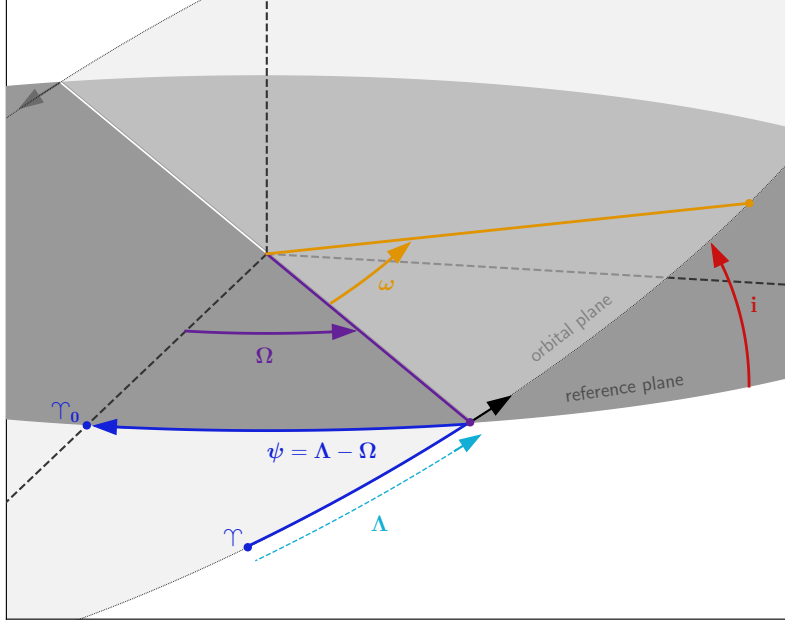


Fig. 28.— Geometry used in the obliquity model, `DistRot`. The light gray represents the planet’s orbital plane, while the darker gray represents a plane of reference. The important orbital angles are the inclination,  $i$ , the longitude of ascending node,  $\Omega$ , and the argument of pericenter,  $\omega$ . The *longitude* of pericenter is a “dog-leg” angle,  $\varpi = \Omega + \omega$ . The angle  $\Lambda$  is measured from the vernal point  $\Upsilon$  at time  $t$ , to the ascending node,  $\Omega$ . The precession angle is defined as  $\psi = \Lambda - \Omega$  (also a dog-leg angle). The reference point for  $\Omega$  is usually chosen as the vernal point at some known date for solar system, however, there is probably a more sensible choice for exoplanetary systems.

where  $\nu$  is the rotation rate,  $r$  is the mean planetary radius, and  $M$  is its mass. Earth’s measured values of  $J_{2\oplus} = 1.08265 \times 10^{-3}$ ,  $\nu_{\oplus} = 7.292115 \times 10^{-5}$  radians s $^{-1}$ ,  $R_{\oplus} = 6.3781 \times 10^6$  m, and  $M_{\oplus} = 5.972186 \times 10^{24}$  kg are used for reference ( $J_2$  from Cook (1980),  $R_{\oplus}$  and  $M_{\oplus}$  from Prša et al. (2016)). This is identical to the method used by Brasser et al. (2014). Like that study, we assume that  $J_2$  cannot go below the measured value of Venus from Yoder (1995), which would ordinarily occur at rotation periods  $\gtrsim 13$  days. The assumption then is that there is a limit to hydrostatic equilibrium for a partially rigid body. Alternatively, the dynamical ellipticity,  $E_D = J_2 M^{-1} r^{-2}$ , and the polar moment of inertia (see below) can be independently set, allowing for departures from hydrostatic equilibrium.

The *specific* polar moment of inertia of a planet,  $CM^{-1}r^{-2}$ , is always between 0.2 and 0.4. Here we assume the  $CM^{-1}r^{-2}$  value of the Earth, 0.33, (Cook 1980). A different

assumption for  $CM^{-1}r^{-2}$  will change the exact values of our results, however, as the moment of inertia should be similar to this value for a terrestrial planet, the overall nature of our results shouldn't change dramatically.

Finally, we note that `DistRot` can also ingest output from previous orbital simulations, such as from N-body models, and compute the rotational axis through finite differencing. This functionality can be useful for complicated systems.

## E. The EqTide Module

The tidal model we use is commonly called the “equilibrium tide” model and was first conceived by George Darwin, grandson of Charles (Darwin 1880). This model assumes the gravitational potential of the tide raiser on an unperturbed spherical surface can be expressed as the sum of Legendre polynomials (*i.e.*, surface waves) and that the elongated equilibrium shape of the perturbed body is slightly misaligned with respect to the line that connects the two centers of mass. This misalignment is due to dissipative processes within the deformed body and leads to a secular evolution of the orbit as well as the spin angular momenta of the two bodies. Furthermore, the bodies are assumed to respond to the time-varying tidal potential as though they are damped, driven harmonic oscillators, a well-studied system. As described below, this approach leads to a set of 6 coupled, non-linear differential equations, but note that the model is linear in the sense that there is no coupling between the surface waves which sum to the equilibrium shape. A substantial body of research is devoted to tidal theory (*e.g.*, Darwin 1880; Goldreich & Soter 1966; Hut 1981; Ferraz-Mello et al. 2008; Wisdom 2008; Efroimsky & Williams 2009; Leconte et al. 2010), and the reader is referred to these studies for a more complete description of the derivations and nuances of equilibrium tide theory.

Equilibrium tide models have the advantage of being semi-analytic, and hence can be used to explore parameter space quickly. They reduce the tidal effects to a single parameter, which is valuable in systems for which very little compositional and structural information is known, *e.g.*, exoplanets. However, they suffer from self-inconsistencies. A rotating, tidally deformed body does not in fact possess multiple rotating tidal waves that create the non-spherical equilibrium shape of a body. The properties of the tidal bulge are due to rigidity, viscosity, structure, and frequencies. Equilibrium tide models are not much more than toy models for tidal evolution – self-consistent models would require three dimensions and include the rheology of the interior and, for ocean-bearing worlds, a 3-dimensional model of currents, ocean floor topography and maps of continental margins. For exoplanets, such a complicated model is not available, nor is it necessarily warranted given the dearth of

observational constraints.

The equilibrium tide frameworks permits fundamentally different assumptions regarding the lag between the passage of the perturber and the passage of the tidal bulge. This ambiguity has produced two well-developed models that have reasonably reproduced observations in our Solar System, but which can diverge significantly when applied to configurations with different properties. One model assumes that the lag is a constant in phase and is independent of frequency. In other words, regardless of orbital and rotational frequencies, the angle between the perturber and the tidal bulge remains constant. Following Greenberg (2009) we will refer to this version as the “constant-phase-lag” or CPL model. At first glance, this may seem to be the best choice, given the body is expected to behave like a harmonic oscillator: In order for the tidal waves to be linearly summed, the damping must be independent of frequency. However, for eccentric orbits, it may not be possible for the phase lag to remain constant as the orbital frequency changes in accordance with Kepler’s 2nd Law (Touma & Wisdom 1994; Efroimsky & Makarov 2013). This has led numerous researchers to reject the CPL model, despite its relative success at reproducing features in the Solar System (*e.g.*, MacDonald 1964; Hut 1981; Goldreich & Soter 1966; Peale et al. 1979), as well as the tidal circularization of close-in exoplanets (Jackson et al. 2008).

The second possibility for the lag is that the time interval between the perturber’s passage and the tidal bulge is constant. In this case, as frequencies change, the angle between the bulge and the perturber changes. We call this model the “constant-time-lag” (CTL) model and use the derivation from (Leconte et al. 2010), but see also (Bolmont et al. 2012; Barnes et al. 2013; Barnes 2017).

In terms of planetary rotation rate, many of the timescales are set by masses, radii, and semi-major axes. For typical main sequence stars, and Mars- to Neptune-sized planets in the classic HZ of Kasting et al. (1993), the timescales range from millions to trillions of years, with the shortest timescales occurring for the largest planets orbiting closest to the smallest stars (Barnes 2017).

The equilibrium tide framework is limited to two bodies and consists of 6 independent parameters: the semi-major axis  $a$ , the eccentricity  $e$ , the two rotation rates  $\Omega_j$ , and two obliquities  $\psi_j$ , where  $j = 1, 2$  corresponds to one of the bodies. If the gravitational gradient across a freely rotating body induces sufficient strain on that body’s interior to force movement, then frictional heating is inevitable. The energy for this heating comes at the expense of the orbit and/or rotational frequency, and hence tidal friction decreases the semi-major axis and rotation period. The friction will also prevent the elongation of the body to align exactly with the perturber. With an asymmetry introduced, torques arise and open pathways for angular momentum exchange. There are three reservoirs of angular momentum:

the orbit and the two rotations. Equilibrium tide models assume orbit-averaged shapes when calculating torques, which is a good approximation for the long-term evolution of the system. The redistribution of angular momentum depends on the tidal power, and the heights and positions of the tidal bulges relative to the line connecting the two centers of mass. The equilibrium tide model can therefore be seen as the angular momentum evolution of two bodies in an orbit that is losing energy.

The tidal power and bulge properties depend on the composition and microphysics of planetary and stellar interiors, which are very difficult to measure in our Solar System, let alone in an external planetary system. In equilibrium tide theory, the coupling between energy dissipation and the tidal bulge is therefore a central feature, and are scaled by two parameters, the Love number of degree 2,  $k_2$ , and a parameter that represents the lag between the line connecting the two centers of mass and the direction of the tidal bulge. In the CPL model, this parameter is the “tidal quality factor”  $Q$ , and in the CTL model it is the “tidal time lag”  $\tau$ .

Although energy dissipation results in semi-major axis decay, angular momentum exchange can lead to semi-major axis growth. This can occur if enough rotational angular momentum can be transferred to the orbit to overcome the decay due to tidal heating. Earth and the Moon are in this configuration now.

For planets on eccentric orbits, the rotation rates of the bodies compared to their instantaneous angular velocity at pericenter determines how  $e$  changes. If the rotational bulge leads the perturber, there will be a net force in the direction of the orbit at pericenter, which acts to accelerate the perturber and increase its eccentricity. If the bulge lags the perturber, the force retards the orbital velocity and the orbit circularizes. This latter case is typical of most close-in planets, and so the orbits circularize (Rasio et al. 1996; Jackson et al. 2008).

### E.1. Constant-Phase-Lag Model

In the CPL model of tidal evolution, the angle between the line connecting the centers of mass and the tidal bulge is constant. This approach is commonly utilized in planetary studies (*e.g.*, Goldreich & Soter 1966; Greenberg 2009) and the evolution is described by the following equations:

$$\frac{de}{dt} = -\frac{ae}{8GM_*M_p} \sum_{i=1}^2 Z'_i \left( 2\varepsilon_{0,i} - \frac{49}{2}\varepsilon_{1,i} + \frac{1}{2}\varepsilon_{2,i} + 3\varepsilon_{5,i} \right) \quad (\text{E1})$$

$$\begin{aligned}
 \frac{da}{dt} &= \frac{a^2}{4GM_*M_p} \sum_{i=1}^2 Z'_i \left( 4\varepsilon_{0,i} + e^2 \left[ -20\varepsilon_{0,i} + \frac{147}{2}\varepsilon_{1,i} + \frac{1}{2}\varepsilon_{2,i} - 3\varepsilon_{5,i} \right] - 4\sin^2(\psi_i) \left[ \varepsilon_{0,i} - \varepsilon_{8,i} \right] \right) \\
 \frac{d\Omega_i}{dt} &= -\frac{Z'_i}{8M_i r_{g,i}^2 R_i^2 n} \left( 4\varepsilon_{0,i} + e^2 \left[ -20\varepsilon_{0,i} + 49\varepsilon_{1,i} + \varepsilon_{2,i} \right] + 2\sin^2(\psi_i) \left[ -2\varepsilon_{0,i} + \varepsilon_{8,i} + \varepsilon_{9,i} \right] \right) \\
 \frac{d\psi_i}{dt} &= \frac{Z'_i \sin(\psi_i)}{4M_i r_{g,i}^2 R_i^2 n \Omega_i} \left( [1 - \xi_i] \varepsilon_{0,i} + [1 + \xi_i] \{ \varepsilon_{8,i} - \varepsilon_{9,i} \} \right). \tag{E2}
 \end{aligned}$$

The quantity  $Z'_i$  is

$$Z'_i \equiv 3G^2 k_{2,i} M_j^2 (M_i + M_j) \frac{R_i^5}{a^9} \frac{1}{nQ_i}, \tag{E3}$$

where  $k_{2,i}$  are the Love numbers of order 2, and  $Q_i$  are the tidal quality factors. The parameter  $\xi_i$  is

$$\xi_i \equiv \frac{r_{g,i}^2 R_i^2 \Omega_i a n}{GM_j}, \tag{E4}$$

where  $i$  and  $j$  refer to the two bodies, and  $r_g$  is the “radius of gyration,” *i.e.*, the moment of inertia is  $M(r_g R)^2$ . The signs of the phase lags are

$$\begin{aligned}
 \varepsilon_{0,i} &= \text{sgn}(2\Omega_i - 2n) \\
 \varepsilon_{1,i} &= \text{sgn}(2\Omega_i - 3n) \\
 \varepsilon_{2,i} &= \text{sgn}(2\Omega_i - n) \\
 \varepsilon_{5,i} &= \text{sgn}(n) \\
 \varepsilon_{8,i} &= \text{sgn}(\Omega_i - 2n) \\
 \varepsilon_{9,i} &= \text{sgn}(\Omega_i), \tag{E5}
 \end{aligned}$$

with  $\text{sgn}(x)$  the sign of any physical quantity  $x$ , *i.e.*,  $\text{sgn}(x) = +1, -1$  or 0.

The tidal heating of the  $i$ th body is due to the transformation of rotational and/or orbital energy into frictional heating. The heating from the orbit is

$$\dot{E}_{\text{orb},i} = \frac{Z'_i}{8} \times \left( 4\varepsilon_{0,i} + e^2 \left[ -20\varepsilon_{0,i} + \frac{147}{2}\varepsilon_{1,i} + \frac{1}{2}\varepsilon_{2,i} - 3\varepsilon_{5,i} \right] - 4\sin^2(\psi_i) \left[ \varepsilon_{0,i} - \varepsilon_{8,i} \right] \right),$$

and that from the rotation is

$$\dot{E}_{\text{rot},i} = -\frac{Z'_i}{8} \frac{\omega_i}{n} \times \left( 4\varepsilon_{0,i} + e^2 \left[ -20\varepsilon_{0,i} + 49\varepsilon_{1,i} + \varepsilon_{2,i} \right] + 2\sin^2(\psi_i) \left[ -2\varepsilon_{0,i} + \varepsilon_{8,i} + \varepsilon_{9,i} \right] \right).$$

The total heat in the  $i$ th body is therefore

$$\dot{E}_{\text{tide},i}^{\text{CPL}} = -(\dot{E}_{\text{orb},i} + \dot{E}_{\text{rot},i}) > 0. \quad (\text{E6})$$

The rate of evolution and amount of heating are set by three free parameters:  $Q$ ,  $k_2$ , and  $r_g$ .  $\dot{E}_{\text{tide},i}^{\text{CPL}}$  can be plugged into Eq. (K1) for worlds that are experiencing tidal heating.

Goldreich (1966) suggested that the equilibrium rotation period for both bodies is

$$P_{eq}^{CPL} = \frac{P}{1 + 9.5e^2}. \quad (\text{E7})$$

Murray & Dermott (1999) present a derivation of this expression, which assumes the rotation rate may take a continuum of values. However, the CPL model described above only permits 4 “tidal waves”, and hence does not permit this continuum. Instead the rotation rate is synchronous up to  $e = \sqrt{1/19} \approx 0.23$  and then jumps instantaneously to  $\omega/n = 1.5$ , *i.e.*, a 3:2 spin-orbit frequency ratio. The next phase jump occurs at  $e = \sqrt{2/19} \approx 0.32$  but is not present in the 2nd order CPL model. Therefore the evolution at larger  $e$  predicted by the CPL model may not be qualitatively correct. We urge caution when interpreting CPL results above  $e = 0.32$ .

## E.2. The Constant Time Lag Model

The constant-time-lag (CTL) model assumes that the time interval between the passage of the perturber and the tidal bulge is constant. This assumption allows the tidal response to be continuous over a wide range of frequencies, unlike the CPL model. But, if the phase lag is a function of the forcing frequency, then the system is no longer analogous to a damped driven harmonic oscillator. Therefore, this model should only be used over a narrow range of frequencies, see Greenberg (2009). However, this model’s use is widespread, especially at

high  $e$ , so we use it to evaluate tidal effects as well. This model predicts larger tidal heating and evolution rates at high  $e$  as any coupling between tidal waves is ignored. Therefore, the CPL and CTL models probably bracket the actual evolution.

The evolution is described by the following equations:

$$\frac{de}{dt} = \frac{11ae}{2GM_1M_2} \sum_{i=1}^2 Z_i \left( \cos(\psi_i) \frac{f_4(e)}{\beta^{10}(e)} \frac{\omega_i}{n} - \frac{18}{11} \frac{f_3(e)}{\beta^{13}(e)} \right) \quad (\text{E8})$$

$$\frac{da}{dt} = \frac{2a^2}{GM_1M_2} \sum_{i=1}^2 Z_i \left( \cos(\psi_i) \frac{f_2(e)}{\beta^{12}(e)} \frac{\omega_i}{n} - \frac{f_1(e)}{\beta^{15}(e)} \right) \quad (\text{E9})$$

$$\frac{d\omega_i}{dt} = \frac{Z_i}{2M_i r_{g,i}^2 R_i^2 n} \left( 2 \cos(\psi_i) \frac{f_2(e)}{\beta^{12}(e)} - [1 + \cos^2(\psi)] \frac{f_5(e)}{\beta^9(e)} \frac{\omega_i}{n} \right) \quad (\text{E10})$$

$$\frac{d\psi_i}{dt} = \frac{Z_i \sin(\psi_i)}{2M_i r_{g,i}^2 R_i^2 n \omega_i} \left( \left[ \cos(\psi_i) - \frac{\xi_i}{\beta} \right] \frac{f_5(e)}{\beta^9(e)} \frac{\omega_i}{n} - 2 \frac{f_2(e)}{\beta^{12}(e)} \right) \quad (\text{E11})$$

where

$$Z_i \equiv 3G^2 k_{2,i} M_j^2 (M_i + M_j) \frac{R_i^5}{a^9} \tau_i, \quad (\text{E12})$$

and

$$\begin{aligned} \beta(e) &= \sqrt{1 - e^2}, \\ f_1(e) &= 1 + \frac{31}{2}e^2 + \frac{255}{8}e^4 + \frac{185}{16}e^6 + \frac{25}{64}e^8, \\ f_2(e) &= 1 + \frac{15}{2}e^2 + \frac{45}{8}e^4 + \frac{5}{16}e^6, \\ f_3(e) &= 1 + \frac{15}{4}e^2 + \frac{15}{8}e^4 + \frac{5}{64}e^6, \\ f_4(e) &= 1 + \frac{3}{2}e^2 + \frac{1}{8}e^4, \\ f_5(e) &= 1 + 3e^2 + \frac{3}{8}e^4. \end{aligned} \quad (\text{E13})$$

The tidal heating of the  $i$ th body is therefore

$$\dot{E}_{\text{tide},i}^{\text{CTL}} = Z_i \left( \frac{f_1(e)}{\beta^{15}(e)} - 2 \frac{f_2(e)}{\beta^{12}(e)} \cos(\psi_i) \frac{\omega_i}{n} + \left[ \frac{1 + \cos^2(\psi_i)}{2} \right] \frac{f_5(e)}{\beta^9(e)} \left( \frac{\omega_i}{n} \right)^2 \right). \quad (\text{E14})$$

$\dot{E}_{\text{tide},i}^{\text{CTL}}$  can be plugged into Eq. (K1) for worlds that are experiencing tidal heating.

It can also be shown that the equilibrium rotation period for both bodies is

$$P_{eq}^{CTL}(e, \psi) = P \frac{\beta^3 f_5(e)(1 + \cos^2 \psi)}{2f_2(e) \cos \psi}, \quad (\text{E15})$$

which for low  $e$  and  $\psi = 0$  reduces to

$$P_{eq}^{CTL} = \frac{P}{1 + 6e^2}. \quad (\text{E16})$$

There is no general conversion between  $Q_p$  and  $\tau_p$ . Only if  $e = 0$  and  $\psi_p = 0$ , when merely a single tidal lag angle  $\varepsilon_p$  exists, then

$$Q_p \approx 1/(2|n - \omega_p|\tau_p), \quad (\text{E17})$$

as long as  $n - \omega_p$  remains unchanged. Hence, a dissipation value for an Earth-like planet of  $Q_p = 12$  (Williams et al. 1978) is not necessarily equivalent to a tidal time lag of 638 s (Lambeck 1977), so the results for the tidal evolution will intrinsically differ among the CPL and the CTL model. However, both choices are common for the respective model.

### E.3. The Orbit-Only Model

The calculations of § 14.3 use the orbital evolution model of Driscoll & Barnes (2015), which only considered the orbital effects and ignored dissipation in the star. We refer to this case as the “orbit-only model.” In this case the planet’s semi-major axis  $a$  and eccentricity  $e$  evolutions are (Goldreich & Soter 1966; Jackson et al. 2009; Ferraz-Mello et al. 2008)

$$\dot{e} = \frac{21}{2} Im(k_2) \frac{M_*}{M_p} \left( \frac{R_p}{a} \right)^5 ne \quad (\text{E18})$$

$$\dot{a} = 2ea\dot{e}. \quad (\text{E19})$$

The mean motion can be replaced with  $n^2 = GM_*/a^3$ , and after rearrangement we obtain

$$\dot{e} = \frac{21}{2} Im(k_2) \frac{M_*^{3/2} G^{1/2} R_p^5}{M_p} \frac{e}{a^{13/2}} \quad (\text{E20})$$

The differential equations for thermal evolution (K3, K4) and orbital evolution (E20, E19) are solved simultaneously to compute coupled thermal-orbital evolutions. The tidally heat Earth model example uses the approximation  $Im(k_2) = k_2/\mathcal{Q}$ , where  $\mathcal{Q} = \eta\omega/\mu$ , in (E19,E20).

## F. The GalHabit Module

The module `GalHabit` (“Galactic Habitability”) is designed to account for the effects of galactic scale processes on binary stars. The main processes are the galactic tide, stellar migration, and stellar encounters, which, as shown by Kaib et al. (2013), can lead to the destabilization of planetary systems.

### F.1. Galactic tides

The galactic tide is a differential force on gravitationally-bound, widely separated objects, such as wide binary star systems or Oort cloud comets orbiting the sun. This force arises because the galaxy is non-uniform in density. At the sun’s galactocentric distance ( $\sim 8$  kpc), the galactic gravitational potential is nearly axisymmetric (disk-like), where the density is highest in the mid-plane and gradually decreases with some scale height in the  $Z$ -direction, *i.e.*, perpendicular to the plane of the disk (Heisler & Tremaine 1986). However, the galactic bulge and halo do provide a spheroidal component to the galactic potential that becomes more important close to the galactic center and at high  $Z$  (Kordopatis et al. 2015). `GalHabit` does not at present account for such departures from axisymmetry, and so should be used with caution when modeling systems in such regions.

The effects of the axisymmetric galactic tide on a system may be described by the time-averaged (or secular) Hamiltonian (Heisler & Tremaine 1986):

$$H_{\text{av}} = -\frac{\mu^2}{2L^2} + \frac{\pi G \rho_0 L^2}{\mu^2} \frac{J^2}{J_z^2} \cdot (J^2 - J_z^2)[J^2 + 5(L^2 - J^2)\sin^2 \omega], \quad (\text{F1})$$

where  $\mu = G(M_c + M)$ ,  $L = \sqrt{\mu a}$ ,  $J = \sqrt{\mu a(1 - e^2)}$ ,  $J_z = J \cos i$ ,  $\rho_0$  is the local galactic density,  $M_c$  is the “central” mass,  $M$  the mass of the orbiter,  $a$  is its semi-major axis,  $e$  is its eccentricity,  $i$  is its inclination of the orbit with respect to the galactic mid-plane, and  $\omega$  is its argument of periastron. The variables  $L$ ,  $J$ , and  $J_z$  are thus canonical momenta associated with the energy of the orbit (in momentum units), the total angular momentum, and the  $Z$ -component of the angular momentum, respectively. From Hamilton’s equations we know that since the canonical angles associated with  $L$  and  $J_z$  do not appear explicitly in  $H_{\text{av}}$ ,  $L$  and  $J_z$  are perfectly conserved. Since  $\omega$ , which is associated with  $J$  does appear, however,  $J$  is free to vary with time. The eccentricity and inclination are thus coupled through the definitions of  $J$  and  $J_z$ , and as one changes under the influence of the tide, the other must compensate, resulting in “Kozai-like” cycling of  $e$  and  $i$ .

The Hamiltonian above results in four equations of motion (Hamilton's equations):

$$\frac{dJ}{dt} = -\frac{\partial H_{av}}{\partial \omega} = -\frac{5\pi G\rho_0}{\mu^2} \frac{L^2}{J^2} (J^2 - J_z^2)(L^2 - J^2) \sin 2\omega, \quad (\text{F2})$$

$$\frac{d\omega}{dt} = \frac{\partial H_{av}}{\partial J} = \frac{2\pi G\rho_0}{\mu^2} \frac{L^2}{J^2} \left[ J^3 + 5 \left( \frac{L^2 J_z^2}{J} - J^3 \right) \sin^2 \omega \right], \quad (\text{F3})$$

$$\frac{d\Omega}{dt} = \frac{\partial H_{av}}{\partial J_z} = -\frac{2\pi G\rho_0}{\mu^2} \frac{L^2}{J^2} J_z [J^2 + 5(L^2 - J^2) \sin^2 \omega], \quad (\text{F4})$$

$$\frac{dl}{dt} = \frac{\partial H_{av}}{\partial L} = \frac{\mu^2}{L^3} + \frac{2\pi G\rho_0}{\mu^2} \frac{L}{J^2} (J^2 - J_z^2) [J^2 + 5(2L^2 - J^2) \sin^2 \omega], \quad (\text{F5})$$

where  $\Omega$  is the longitude of ascending node and  $l$  is the mean anomaly. Since  $L$  is constant, and we are modeling the orbit-averaged (secular) evolution of the system, we can disregard Equation (F5) — this choice ultimately affects none of the other variables.

These equations are modeled in this form and the other orbital elements ( $e$  and  $i$ ) can be calculated from  $J$  and  $J_z$ . Since in future versions of `vPLanet` we intend to include the additional dynamics of triple star systems, we desire a form of these equations that is more easily generalized to different coordinate systems. Cartesian coordinate systems are ideal as rotational and translational transformations are easily applied. In our case, we utilize the Cartesian components of the angular momentum vector (per unit mass),  $\vec{J} = (J_x, J_y, J_z)$ , and the eccentricity vector,  $\vec{e} = (e_x, e_y, e_z)$ . They are defined as:

$$J_x = J \sin \Omega \sin i, \quad (\text{F6})$$

$$J_y = -J \cos \Omega \sin i, \quad (\text{F7})$$

$$J_z = J \cos i, \quad (\text{F8})$$

$$e_x = e [\cos \Omega \cos \omega - \sin \Omega \sin \omega \cos i], \quad (\text{F9})$$

$$e_y = e [\sin \Omega \cos \omega + \cos \Omega \sin \omega \cos i], \quad (\text{F10})$$

$$e_z = e \sin \omega \sin i. \quad (\text{F11})$$

The derivatives are calculated via chain-rule from Hamilton's equations above and written in terms of orbital elements (when convenient), resulting in

$$\frac{dJ_x}{dt} = \frac{\sin \Omega}{\sin i} \frac{dJ}{dt} + J \sin i \cos \Omega \frac{d\Omega}{dt}, \quad (\text{F12})$$

$$\frac{dJ_y}{dt} = -\frac{\cos \Omega}{\sin i} \frac{dJ}{dt} + J \sin i \cos \Omega \frac{d\Omega}{dt}, \quad (\text{F13})$$

$$\frac{dJ_z}{dt} = 0, \quad (\text{F14})$$

and

$$\frac{de_x}{dt} = \frac{\partial e_x}{\partial J} \frac{dJ}{dt} + \frac{\partial e_x}{\partial \Omega} \frac{d\Omega}{dt} + \frac{\partial e_x}{\partial \omega} \frac{d\omega}{dt}, \quad (\text{F15})$$

$$\frac{de_y}{dt} = \frac{\partial e_y}{\partial J} \frac{dJ}{dt} + \frac{\partial e_y}{\partial \Omega} \frac{d\Omega}{dt} + \frac{\partial e_y}{\partial \omega} \frac{d\omega}{dt}, \quad (\text{F16})$$

$$\frac{de_z}{dt} = \frac{\partial e_z}{\partial J} \frac{dJ}{dt} + \frac{\partial e_z}{\partial \omega} \frac{d\omega}{dt}, \quad (\text{F17})$$

where, for the  $x$ -components,

$$\frac{\partial e_x}{\partial J} = -\sqrt{\frac{1-e^2}{\mu ae^2}} \cos \Omega \cos \omega + \frac{\cos i}{e\sqrt{\mu a(1-e^2)}} \sin \Omega \sin \omega, \quad (\text{F18})$$

$$\frac{\partial e_x}{\partial \Omega} = -e \sin \Omega \cos \omega - e \cos \Omega \sin \omega \cos i, \quad (\text{F19})$$

$$\frac{\partial e_x}{\partial \omega} = -e \cos \Omega \sin \omega - e \sin \Omega \cos \omega \cos i, \quad (\text{F20})$$

for the  $y$ -components,

$$\frac{\partial e_y}{\partial J} = -\sqrt{\frac{1-e^2}{\mu ae^2}} \sin \Omega \cos \omega - \frac{\cos i}{e\sqrt{\mu a(1-e^2)}} \cos \Omega \sin \omega, \quad (\text{F21})$$

$$\frac{\partial e_y}{\partial \Omega} = e \cos \Omega \cos \omega - e \sin \Omega \sin \omega \cos i, \quad (\text{F22})$$

$$\frac{\partial e_y}{\partial \omega} = -e \sin \Omega \sin \omega + e \cos \Omega \cos \omega \cos i, \quad (\text{F23})$$

and for the  $z$ -components,

$$\frac{\partial e_z}{\partial J} = \frac{e^2 - \sin^2 i}{e \sin i \sqrt{\mu a(1-e^2)}} \sin \omega, \quad (\text{F24})$$

$$\frac{\partial e_z}{\partial \omega} = e \cos \omega \sin i. \quad (\text{F25})$$

Note that Equations (F12), (F13), (F18), (F21), and (F24) contain singularities at either  $e = 0$  or  $i = 0$ , however, the offending terms cancel when the algebra in Equations (F12 - F17) is fully carried out. We perform this algebra as necessary to remove the singularities, which are likely to trigger numerical instabilities or unphysical behavior. **vPLanet** contains the resulting equations.

Our integration variables for the galactic tide have thus grown from three ( $J$ ,  $\Omega$ , and  $\omega$ ) to five ( $J_x$ ,  $J_y$ ,  $e_x$ ,  $e_y$ , and  $e_z$ ); this is the trade-off of using this more flexible coordinate

system. In practice, the tidal model is still very fast, and thus this is an acceptable exchange for future flexibility.

For output, the orbital elements need to be calculated from the Cartesian vectors. The eccentricity is simply  $e = |\vec{e}|$ , while  $i$  and  $\Omega$  can be calculated from  $J = |\vec{J}|$ ,  $J_x$ ,  $J_y$ , and  $J_z$  (Eqs. [F6]—[F8]). For  $\omega$ , Mardling & Lin (2002) give

$$\cos \omega = \hat{e} \cdot \hat{n} \quad (\text{F26})$$

$$\sin \omega = \hat{e} \cdot (\hat{J} \times \hat{n}) \quad (\text{F27})$$

where  $\vec{n} = \hat{Z} \times \vec{J}$  and  $\hat{Z}$  is the unit vector perpendicular to the galactic plane. Note that  $\vec{n}$  contains the full vector  $\vec{J}$ , not its unit vector  $\hat{J}$ , and that in the equations above  $\hat{n} = \vec{n}/|\vec{n}|$ . The semi-major axis,  $a$ , is constant under the galactic tide alone, however, additional forces (see next Section) lead to changes in  $a$ . To recalculate  $a$ , we can first calculate  $e$  and then utilize the definition of  $J$ .

The local density around the host system is calculated using the mass model of Kordopatis et al. (2015), which accounts for disk stars, gas, dark matter, and stars in the galactic bulge. Technically, the latter two components have spheroidal distributions and thus do not fit the axisymmetric assumption of the tidal model. The time-averaging of the galactic Hamiltonian to produce Eq. (F1) requires axisymmetry (Heisler & Tremaine 1986). Generally, within the disk of the Milky Way, these components are small and axisymmetry is a decent approximation. However, close to the galactic center or at high  $Z$ , this approximation may not hold. In that case, the unaveraged Hamiltonian (or a reformulation of  $H_{\text{av}}$ ) for the galactic tide may be needed.

## F.2. Encounters with passing stars

The second force supplied by the galactic environment is the gravitational perturbation of wide orbits by passing stars. Close encounters between the solar system and nearby stars are thought to affect the Oort cloud and thus to contribute to the appearance of long-period comets (Duncan et al. 1987; Heisler et al. 1987; Kenyon & Bromley 2004; Rickman et al. 2008; Collins & Sari 2010). Similarly, such close encounters will affect the orbits of widely separated binary stars (Kaib et al. 2013), potentially affecting orbiting planets. We use the techniques developed by Heisler et al. (1987) and Rickman et al. (2008) to account for these perturbations. The process is described as follows.

At the start of a simulation, we calculate the total stellar encounter rate and the time until the next encounter. The encounter rate is based on the local stellar properties deter-

mined by García-Sánchez et al. (2001), see Table 5. Given an “encounter radius” (*i.e.*, the distance at which the system and a passing star are considered to encounter each other),  $R_{\text{enc}}$ , the rate of encounters is given by (García-Sánchez et al. 2001)

$$f_{\text{enc}} = \pi R_{\text{enc}}^2 \sum_i v_i n_{\star i}, \quad (\text{F28})$$

where  $n_{\star i}$  is the number density of each stellar type and  $v_i = \sqrt{v_{h,i}^2 + \sigma_{\star i}^2}$ . The encounter velocity,  $v_i$ , is a function of both the stellar type’s velocity dispersion,  $\sigma_{\star i}$ , and the host system’s peculiar (or “apex”) velocity relative to each stellar type,  $v_{h,i}$ . Using the numbers in García-Sánchez et al. (2001) and  $R_{\text{enc}} = 1$  pc yields a total encounter rate (summed over 13 stellar types) of 10.5 Myr<sup>-1</sup> for the sun in its current location. The density of stars increases toward the galactic center, while the velocity dispersion increases over time in galactic simulations (Minchev et al. 2012; Roškar et al. 2012). For systems placed at different galactocentric distances, we scale the number density according to the mass model of Kordopatis et al. (2015). The velocity dispersion is scaled as  $\sqrt{t}$ , where  $t$  is the simulation time. The next encounter time is then

$$t_{\text{next}} = t - \frac{\ln \xi}{f_{\text{enc}}}, \quad (\text{F29})$$

where  $\xi$  is a random number on the interval (0, 1]. This is taken to be the time of closest approach to the host system’s primary star (see below).

When the simulation time exceeds the time of the next stellar encounter, the initial position, mass, and velocity of the passing star are selected randomly. The position is given by two random numbers that give the angles  $\theta_\star$  and  $\phi_\star$ —these are the co-latitudinal and longitudinal position of the passing star on a sphere of radius  $R_{\text{enc}}$ , centered on the primary component of the host system. The passing star’s initial position,  $\vec{R}_\star = (x_\star, y_\star, z_\star)$ , is then

$$x_\star = R_{\text{enc}} \sin \theta_\star \cos \phi_\star, \quad (\text{F30})$$

$$y_\star = R_{\text{enc}} \sin \theta_\star \sin \phi_\star, \quad (\text{F31})$$

$$z_\star = R_{\text{enc}} \cos \theta_\star. \quad (\text{F32})$$

To obtain the stellar mass, we need to build a distribution of the stellar encounter frequencies for each stellar type and utilize rejection sampling. Similar to Eq. (F28), the encounter frequencies are given for each stellar type by

$$f_{\text{enc},i} = \pi R_{\text{enc}}^2 v_i n_{\star i}, \quad (\text{F33})$$

with values again given by García-Sánchez et al. (2001). The distribution of stellar types extends across a magnitude range of 23.7 (the bin edges are given in Table 5) for the main

sequence. Giant and white dwarfs are given bin sizes of  $\Delta M_{V,i} = 1$  each, resulting in a total magnitude range of 25.7. We now draw a random magnitude,  $\xi_{M_V}$ , on the interval  $[-7.7, 18]$ , with  $-7.7 < M_V < -6.7$  assigned to giants and  $-6.7 < M_V < -5.7$  assigned to white dwarfs (for selection purposes only), and calculate the relative frequency of an encounter as  $f_{\text{rel}} = f_{\text{enc},i}/\Delta M_{V,i}$  for the corresponding stellar type. We next draw another random number,  $\xi_{\text{samp}}$ , on the interval  $[0, f_{\text{enc}}]$ , where  $f_{\text{enc}}$  is the total encounter rate—this is the threshold for acceptance. If  $f_{\text{rel}} < \xi_{\text{samp}}$ , we then redraw  $\xi_{M_V}$  and  $\xi_{\text{samp}}$  until  $f_{\text{rel}} > \xi_{\text{samp}}$ . Once a value for the magnitude is accepted, the mass of the passing star is calculated using the formulas in Reid et al. (2002) for the main sequence (white dwarfs are assigned a mass of  $0.9 M_\odot$  and giants a mass of  $4 M_\odot$ ).

The three components of the velocity of the star are selected from a normal distribution with width  $\sigma_{\star i}/\sqrt{3}$ . This velocity is relative to the local standard of rest and thus we must account for the host system’s peculiar (“apex”) velocity. The velocity between the host and the passing star is then

$$\vec{v}_{h,\star} = \vec{v}_\star - \vec{v}_h, \quad (\text{F34})$$

where  $\vec{v}_\star$  is the passing star’s velocity as randomly selected and  $\vec{v}_h$  is the host system’s peculiar velocity relative to the selected star’s type. To account for the additional effect of the host system’s velocity on the encounter rate (and selection process), we reject and redraw the velocity if a random number on  $[0, 1]$  is greater than  $|\vec{v}_{h,\star}|/v_{\max}$ , where  $v_{\max} = v_h + 3\sigma_{\star i}$  (see Rickman et al. 2008). We similarly reject and redraw  $\vec{v}_{h,\star}$  if its radial component  $(\vec{v}_{h,\star})_r$  is positive, in which case the passing star would be moving away from the host system.

Our next step is to advance the mean anomaly,  $l$ , of the orbiting body in the host system (whether it is a comet or secondary star). This value is calculated from  $l(t) = l(t-\Delta t) + n\Delta t$ , where  $n = \sqrt{\mu/a^3} = \mu^2/L^3$ . The mean motion,  $n$ , is merely the first term in Eq. (F5). The model is not fully self-consistent in that the second term in Eq. (F5) (the affect of the tide on the mean anomaly) is not included (indeed, this is what makes the model “secular”), however, this term is generally very small compared to  $n$  (Heisler & Tremaine 1986).

Next, we calculate the impact parameters of the passing star. There are two that interest us: the closest approach to the primary (or central) star of the host system,  $\vec{b}_1$ , and the closest approach to the orbiter,  $\vec{b}_2$ , which do not occur at the same instant in time. The time of the encounter,  $t_{\text{next}}$ , is taken to be the time of closest approach to the primary,  $\vec{b}_1$ . The impact parameters are calculated using simple kinematics assuming that the positions of each body in the host system are fixed at the time of the encounter,  $t_{\text{next}}$ , and that the

passing star’s velocity is constant. This approach translates to

$$\vec{b}_1 = \vec{v}_{h,\star} \Delta t_1 + \vec{R}_\star \quad (\text{F35})$$

$$\vec{b}_2 = \vec{v}_{h,\star} \Delta t_2 + \vec{R}_\star - \vec{R}_2, \quad (\text{F36})$$

where  $\vec{R}_2$  is the position of orbiting body of the host system at time  $t_{\text{next}}$  and

$$\Delta t_1 = \frac{-\vec{R}_\star \cdot \vec{v}_{h,\star}}{v_{h,\star}^2} \quad (\text{F37})$$

$$\Delta t_2 = \frac{-(\vec{R}_\star - \vec{R}_2) \cdot \vec{v}_{h,\star}}{v_{h,\star}^2}. \quad (\text{F38})$$

Finally, we apply the perturbation using the impulse approximation (Remy & Mignard 1985). This takes the form of an instantaneous change in the orbiter’s velocity, given by

$$\Delta \vec{v}_2 = \frac{2Gm_\star}{v_{\star,2} b_2^2} \vec{b}_2 - \frac{2Gm_\star}{v_{h,\star} b_1^2} \vec{b}_1, \quad (\text{F39})$$

where  $m_\star$  is the mass of the passing star and  $v_{\star,2}$  is the relative speed between the orbiter and the passing star. We then recalculate the osculating elements based on the new velocity and finally recalculate  $\vec{e}$  and  $\vec{J}$ .

We then randomly select the time until the next encounter,  $t_{\text{next}}$ , using the procedure previously described, and then continue integration of the tidal model, etc., until  $t_{\text{next}}$  is exceeded.

### F.3. Radial migration

Radial migration of the host system is treated as a sudden change in the galactocentric position, since galactic simulations show the process is typically very rapid (Roškar et al. 2008). In this case, the encounter rate is recalculated at the time of migration, as is the local mass density,  $\rho_0$ . Currently, a system is only able to migrate once per simulation.

## G. The POISE Module

The climate model, POISE (Planetary Orbit-Influenced Simple EBM), is a one-dimensional EBM based on North & Coakley (1979), with a number of modifications, foremost of which is the inclusion of a model of ice sheet growth, melting, and flow. The model is one-dimensional

in  $x = \sin \phi$ , where  $\phi$  is the latitude. In this fashion, latitude cells of size  $dx$  will not have equal width in latitude, but will be equal in area. The general energy balance equation is

$$C(x) \frac{\partial T}{\partial t}(x, t) - D(x, t) \nabla^2 T(x, t) + I(x, T, t) = S(x, t)(1 - \alpha(x, T, t)), \quad (\text{G1})$$

where  $C(x)$  is the heat capacity of the surface at location  $x$ ,  $T$  is the surface temperature,  $t$  is time,  $D$  is the coefficient of heat diffusion between latitudes (due to atmospheric circulation),  $I(x, t)$  is the outgoing long-wave radiation (OLR) to space (*i.e.*, the thermal infrared flux),  $S(x, t)$  is the incident instellation (stellar flux), and  $\alpha$  is the planetary albedo and represents the percent of the instellation that is reflected back into space.

Though the model lacks a true longitudinal dimension, each latitude is divided into a land portion and a water portion. The land and water have distinct heat capacities and albedos, and heat is allowed to flow between the two regions. The energy balance equation can then be separated into two equations:

$$\begin{aligned} C_L \frac{\partial T_L}{\partial t} - D \frac{\partial}{\partial x} (1 - x^2) \frac{\partial T_L}{\partial x} + \frac{\nu}{f_L} (T_L - T_W) + I(x, T_L, t) \\ = S(x, t)(1 - \alpha(x, T_L, t)), \end{aligned} \quad (\text{G2})$$

$$\begin{aligned} C_W^{eff} \frac{\partial T_W}{\partial t} - D \frac{\partial}{\partial x} (1 - x^2) \frac{\partial T_W}{\partial x} + \frac{\nu}{f_W} (T_W - T_L) + I(x, T_W, t) \\ = S(x, t)(1 - \alpha(x, T_W, t)), \end{aligned} \quad (\text{G3})$$

where we have employed the co-latitudinal component of the spherical Laplacian,  $\nabla^2$  (the radial and longitudinal/azimuthal components vanish). The effective heat capacity of the ocean is  $C_W^{eff} = m_d C_W$ , where  $m_d$  is an adjustable parameter representing the mixing depth of the ocean. The parameter  $\nu$  is used to adjust the land-ocean heat transfer to reasonable values, and  $f_L$  and  $f_W$  are the fractions of each latitude cell that are land and ocean, respectively.

The instellation received as a function of latitude,  $\phi$ , and declination of the host star,  $\delta$ , is calculated using the formulae of Berger (1978). Declination,  $\delta$ , varies over the course of the planet's orbit for nonzero obliquity. For Earth, for example,  $\delta \approx 23.5^\circ$  at the northern summer solstice,  $\delta = 0^\circ$  at the equinoxes, and  $\delta \approx -23.5^\circ$  at the northern winter solstice. Because  $\delta$  is a function of time (or, equivalently, orbital position), the instellation varies, and gives rise to the seasons (again, assuming the obliquity is nonzero). For latitudes and times where there is no sunrise (*e.g.*, polar darkness during winter):

$$S(\phi, \delta) = 0, \quad (\text{G4})$$

while for latitudes and times where there is no sunset:

$$S(\phi, \delta) = \frac{S_\star}{\rho^2} \sin \phi \sin \delta, \quad (\text{G5})$$

and for latitudes with a normal day/night cycle:

$$S(\phi, \delta) = \frac{S_*}{\pi\rho^2} (H_0 \sin \phi \sin \delta + \cos \phi \cos \delta \sin H_0). \quad (\text{G6})$$

Here,  $S_*$  is the solar/stellar constant,  $\rho$  is the distance between the planet and host star normalized by the semi-major axis (*i.e.*,  $\rho = r/a$ ), and  $H_0$  is the hour angle of the star at sunrise and sunset, and is defined as:

$$\cos H_0 = -\tan \phi \tan \delta. \quad (\text{G7})$$

The declination of the host star with respect to the planet’s celestial equator is a simple function of its obliquity  $\varepsilon$  and its true longitude  $\theta$ :

$$\sin \delta = \sin \varepsilon \sin \theta. \quad (\text{G8})$$

See also Laskar et al. (1993) for a comprehensive derivation. For these formulas to apply, the true longitude should be defined as  $\theta = f + \Delta^*$ , where  $f$  is the true anomaly (the angular position of the planet with respect to its periastron) and  $\Delta^*$  is the angle between periastron and the planet’s position at its northern spring equinox, given by

$$\Delta^* = \varpi + \psi + 180^\circ. \quad (\text{G9})$$

Above,  $\varpi$  is the longitude of periastron, and  $\psi$  is the precession angle. Note that we add  $180^\circ$  because of the convention of defining  $\psi$  based on the vernal point,  $\Upsilon$ , which is the position of the *sun* at the time of the northern spring equinox.

A point of clarification is in order: EBMs (at least, the models employed in this study) can be either *seasonal* or *annual*. The EBM component of **POISE** is a seasonal model—the variations in the instellation throughout the year/orbit are resolved and the temperature of the surface at each latitude varies in response, according to the leading terms in Equations (G2) and (G3). In an annual model, the instellation at each latitude is averaged over the year, and the energy balance equation (Eq. G1) is forced into “steady state” by setting  $\partial T / \partial t$  equal to zero (either numerically or analytically). By “steady state”, we mean that the surface conditions (temperature and albedo) come to final values and remain there. Seasonal EBMs, on the other hand, can be in “equilibrium”, in that the orbitally averaged surface conditions remain the same from year to year, but the surface conditions vary *throughout* the year.

The planetary albedo is a function of surface type (land or water), temperature, and zenith angle. For land grid cells, the albedo is:

$$\alpha = \begin{cases} \alpha_L + 0.08P_2(\sin Z) & \text{if } M_{\text{ice}} = 0 \text{ and } T > -2^\circ \text{ C} \\ \alpha_i & \text{if } M_{\text{ice}} > 0 \text{ or } T \leq -2^\circ \text{ C}, \end{cases} \quad (\text{G10})$$

while for water grid cells it is:

$$\alpha = \begin{cases} \alpha_W + 0.08P_2(\sin Z) & \text{if } T > -2^\circ \text{ C} \\ \alpha_i & \text{if } T \leq -2^\circ \text{ C}, \end{cases} \quad (\text{G11})$$

where  $Z$  is the zenith angle of the sun at noon and  $P_2(x) = 1/2(3x^2 - 1)$  (the second Legendre polynomial). This last quantity is used to approximate the additional reflectivity seen at shallow incidence angles, *e.g.*, at high latitudes on Earth. The zenith angle at each latitude is given by

$$Z = |\phi - \delta|. \quad (\text{G12})$$

The albedos,  $\alpha_L$ ,  $\alpha_W$  (see Table 7), not accounting for zenith angle effects, are chosen to match Earth data (North & Coakley 1979) and account, over the large scale, for clouds, various surface types, and water waves. Additionally, the factor of 0.08 in Equations (G10) and (G11) is chosen to reproduce the albedo distribution in North & Coakley (1979). The ice albedo,  $\alpha_i$ , is a single value that does not depend on zenith angle due to the fact that ice tends to occur at high zenith angle, so that the zenith angle is essentially already accounted for in the choice of  $\alpha_i$ . Equation (G10) indicates that when there is ice on land ( $M_{\text{ice}} > 0$ ), or the temperature is below freezing, the land takes on the albedo of ice. Though there are multiple conditionals governing the albedo of the land, in practice the temperature condition is only used when ice sheets are turned off in the model, since ice begins to accumulate at  $T = 0^\circ \text{ C}$ , and so is always present when  $T < -2^\circ \text{ C}$ . Equation (G11) indicates a simpler relationship for the albedo over the oceans: when it is above freezing, the albedo is that of water (accounting also for zenith angle effects); when it is below freezing, the albedo is that of ice.

We take the land fraction and water fraction to be constant across all latitudes. This is roughly like having a single continent that extends from pole to pole. The current version of **POISE** does not contain other geographies because we have not yet developed a consistent method to handle the flow of at the land-ocean interface.

North & Coakley (1979) utilized a linearization of the OLR with temperature:

$$I = A + BT, \quad (\text{G13})$$

where, for Earth,  $A = 203.3 \text{ W m}^{-2}$  and  $B = 2.09 \text{ W m}^{-2} \text{ }^\circ\text{C}^{-1}$ , and  $T$  is the surface temperature in  ${}^\circ\text{C}$ . The purpose of this linearization is that it allows the coupled set of equations to be formulated as a matrix problem that can be solved using an implicit Euler scheme (Press et al. 1987) with the following form:

$$\mathcal{M} \cdot T_{n+1} = \frac{CT_n}{\Delta t} - A + S(1 - \alpha), \quad (\text{G14})$$

where  $T_n$  is a vector containing the current surface temperatures,  $T_{n+1}$  is a vector representing the temperatures to be calculated, and  $C$ ,  $A$ ,  $S$ , and  $\alpha$  are vectors containing the heat capacities, OLR offsets (Eq. [G13]), instellation at each latitude, and albedos, respectively. The matrix  $\mathcal{M}$  contains all of the information on the left-hand sides of Eqs. (G2) and (G3) related to temperature. The time-step,  $\Delta t$ , is chosen so that conditions do not change significantly between steps, resulting in typically 60 to 80 time-steps per orbit. The new temperature values can then be calculated by taking the dot-product of  $\mathcal{M}^{-1}$  with the right-hand side of Eq. (G14). The large time step allowed by this integration scheme greatly speeds the climate model, permitting simulations for millions of years.

We model ice accumulation and ablation in a similar fashion to Armstrong et al. (2014). Ice accumulates on land at a constant rate,  $r_{\text{snow}}$ , when temperatures are below 0° C. Melting/ablation occurs when ice is present and temperatures are above 0° C, according to the formula:

$$\frac{dM_{\text{ice}}}{dt} = \frac{\xi\sigma(T_{\text{freeze}}^4 - (T + T_{\text{freeze}})^4)}{L_h}, \quad (\text{G15})$$

where  $M_{\text{ice}}$  is the surface mass density of ice,  $\sigma = 5.67 \times 10^{-8} \text{ W m}^{-2} \text{ K}^{-4}$  is the Stefan-Boltzmann constant,  $L_h$  is latent heat of fusion of ice,  $3.34 \times 10^5 \text{ J kg}^{-1}$  and  $T_{\text{freeze}} = 273.15 \text{ K}$ . The factor of  $\xi$  that appears here, is used to scale the ice ablation. This can be done to reproduce values similar to Earth ( $\sim 3 \text{ mm } ^\circ\text{C}^{-1} \text{ day}^{-1}$  (see Braithwaite & Zhang 2000; Lefebvre et al. 2002; Huybers & Tziperman 2008) or to experiment with other melting rates.

The ice sheets flow across the surface via deformation and sliding at the base. We use the formulation from Huybers & Tziperman (2008) to model the changes in ice height due to these effects. Bedrock depression is important in this model (despite the fact that we have only one atmospheric layer and thus do not resolve elevation-based effects), because the flow rate is affected. The ice flow (via Huybers & Tziperman 2008) is:

$$\frac{\partial h}{\partial t} = \frac{\partial}{\partial y} \left[ \frac{2A_{\text{ice}}(\rho_i g)^n}{n+2} \left| \left( \frac{\partial(h+H)}{\partial y} \right)^{n-1} \right| \cdot \frac{\partial(h+H)}{\partial y} (h+H)^{n+2} + u_b h \right], \quad (\text{G16})$$

where  $h$  is the height of the ice,  $H$  is the height of the bedrock (always negative or zero, in this case),  $A_{\text{ice}}$  represents the deformability of the ice,  $\rho_i$  is the density of ice,  $g$  is the acceleration due to gravity, and  $n$  is the exponent in Glen's flow law (Glen 1958), where  $n = 3$ . The ice height and ice surface mass density,  $M_{\text{ice}}$  are simply related via  $M_{\text{ice}} = \rho_i h$ . The first term inside the derivative represents the ice deformation; the second term is the sliding of the ice at the base. The latitudinal coordinate,  $y$ , is related to the radius of the planet and the latitude,  $y = R\phi$ , thus  $\Delta y = R\Delta x(1-x^2)^{-1/2}$ . Finally,  $u_b$ , the ice velocity

across the sediment, is:

$$u_b = \frac{2D_0 a_{\text{sed}}}{(m+1)b_{\text{sed}}} \left( \frac{|a_{\text{sed}}|}{2D_0 \mu_0} \right)^m \cdot \left( 1 - \left[ 1 - \frac{b_{\text{sed}}}{|a_{\text{sed}}|} \min \left( h_s, \frac{|a_{\text{sed}}|}{b_{\text{sed}}} \right) \right]^{m+1} \right), \quad (\text{G17})$$

as described by Jenson et al. (1996). The constant  $D_0$  represents a reference deformation rate for the sediment,  $\mu_0$  is the reference viscosity of the sediment,  $h_s$  is the depth of the sediment, and  $m = 1.25$ . The shear stress from the ice on the sediment is:

$$a_{\text{sed}} = \rho_i g h \frac{\partial(h+H)}{\partial y}, \quad (\text{G18})$$

and the rate of increase of shear strength with depth is:

$$b_{\text{sed}} = (\rho_s - \rho_w)g \tan \phi_s, \quad (\text{G19})$$

where  $\rho_s$  and  $\rho_w$  are the density of the sediment and water, respectively, and  $\phi_s$  is the internal deformation angle of the sediment. We adopt the same numerical values as Huybers & Tziperman (2008) for all parameters related to ice and sediment (see Table 8), with a few exceptions. We use a value of  $A_{\text{ice}}$  (ice deformability) that is consistent with ice at 270 K (Paterson 1994), and a value of  $r_{\text{snow}}$  (the precipitation rate) that best reproduces Milankovitch cycles on Earth (see Section 14.1). Note also that the value of  $D_0$  in Table A2 of Huybers & Tziperman (2008) appears to be improperly converted for the units listed (the correct value, from Jenson et al. (1996), is listed in the text, however). With Eqs. (G17) and (G18), Eq. (G16) can be treated numerically as a diffusion equation, with the form:

$$\frac{\partial h}{\partial t} = D_{\text{ice}} \frac{\partial^2(h+H)}{\partial y^2}, \quad (\text{G20})$$

where,

$$D_{\text{ice}} = \frac{2A_{\text{ice}}(\rho_i g)^n}{n+2} \left| \left( \frac{\partial(h+H)}{\partial y} \right)^{n-1} \right| (h+H)^{n+2} + \frac{2D_0 \rho_i g h^2}{(m+1)b_{\text{sed}}} \left( \frac{|a_{\text{sed}}|}{2D_0 \mu_0} \right)^m \cdot \left( 1 - \left[ 1 - \frac{b_{\text{sed}}}{|a_{\text{sed}}|} \min \left( h_s, \frac{|a_{\text{sed}}|}{b_{\text{sed}}} \right) \right]^{m+1} \right), \quad (\text{G21})$$

and  $D_{\text{ice}}$  is evaluated at each time-step, at every boundary to provide mass continuity. We solve the diffusion equation numerically using a Crank-Nicolson scheme (Crank et al. 1947).

The bedrock depresses and rebounds locally in response to the changing weight of ice above, always seeking isostatic equilibrium. The equation governing the bedrock height,  $H$ , is

$$\frac{\partial H}{\partial t} = \frac{1}{T_b} \left( H_{\text{eq}} - H - \frac{\rho_i h}{\rho_b} \right), \quad (\text{G22})$$

where  $T_b$  is a characteristic relaxation time scale,  $H_{eq} = 0$  is the ice-free equilibrium height, and  $\rho_b$  is the bedrock density (Clark & Pollard 1998; Huybers & Tziperman 2008). We again adopt the values used by Huybers & Tziperman (2008) (see Table 8).

Because of the longer time-scales (years) associated with the ice sheets, the growth/melting and ice-flow equations are run asynchronously in `POISE`. First, the EBM, Eq. (G1), is run for 4-5 orbital periods, and ice accumulation and ablation is tracked over this time frame, but ice-flow (Equation G16) is ignored. The annually-averaged ice accumulation/ablation is then calculated from this time-frame and passed to the ice-flow time-step, which can be much longer (years). The EBM is then re-run periodically to update accumulation and ablation and ensure that conditions vary smoothly and continuously.

To clarify, the hierarchy of models and their time-steps is as follows:

1. The EBM (shortest time-step): run for a duration of several orbital periods with time-steps on the order of days. The model is then rerun at the end of every orbital/obliquity time-step and at user-set intervals throughout the ice-flow model.
2. The ice-flow model (middle time-step): run at the end of every orbital time-step (with time-steps of a few orbital periods), immediately after the EBM finishes. The duration of the model will follow one of two scenarios:
  - (a) If the orbital/obliquity time-step is sufficiently long, the EBM is rerun at user-set intervals, then the ice-flow model continues. The ice-flow model and the EBM thus alternate back-and-forth until the end of the orbit/obliquity time-step.
  - (b) If the orbital/obliquity time-step is shorter than the user-set interval, the ice-flow model simply runs until the end of the orbital time-step.
3. The rest of `vPLanet` (longest time-step). The time-steps are set by the fastest changing variable amongst those parameters.

This approach is shown schematically in Figure 29. The user-set interval discussed above must be considered carefully. The assumption is that annually-averaged climate conditions like surface temperature and albedo do not change much during the time span over which the ice-flow model runs. Hence, we choose a value that ensures that the ice-flow does not run so long that it dramatically changes the albedo without updating the temperature and ice balance (growth/ablation) via the EBM.

The initial conditions for the EBM are as follows. The first time the EBM is run, the planet has zero ice mass on land, the temperature on both land and water is set by the

function

$$T_0 = 7.5^\circ\text{C} + (20^\circ\text{C})(1 - 2 \sin^2 \phi), \quad (\text{G23})$$

where  $\phi$  is the latitude. This gives the planet a mean temperature of  $\sim 14^\circ\text{ C}$ , ranging from  $\sim 28^\circ\text{ C}$  in the tropics to  $\sim -13^\circ\text{ C}$  at the poles. This is thus a “warm start” condition. The initial albedo of the surface is calculated from the initial temperatures. We then perform a “spin-up” phase, running the EBM iteratively until the mean temperature between iterations changes by  $< 0.1^\circ\text{ C}$ , *without* running the orbit, obliquity, or ice-flow models, to bring the seasonal EBM into equilibrium at the actual stellar flux the planet receives and its actual initial obliquity. Then, every time the EBM is rerun (at the user-set interval or the end of the orbit/obliquity time-step), the initial conditions are taken from the previous EBM run (temperature distribution) and the end of the ice-flow run (albedo, ice mass).

## H. The RadHeat Module

Radiogenic heat production in the Earth is generated primarily by the decay of  $^{238}\text{U}$ ,  $^{235}\text{U}$ ,  $^{232}\text{Th}$ , and  $^{40}\text{K}$  in the crust, mantle, and core. Other species, such as  $^{26}\text{Al}$ , are also potential heat sources on exoplanets. The radiogenic power produced by species  $i$  in reservoir  $j$  is

$$Q_{i,j} = Q_{i,j}(0) \exp(-\lambda_{i,1/2} t) \quad (\text{H1})$$

where  $\lambda_{i,1/2} = \ln 2 / \tau_{i,1/2}$ ,  $\tau_{i,1/2}$  is the halflife,  $t$  is time, and  $Q_{i,j}(0)$  is the initial heat production at  $t = 0$ . The initial radiogenic heat can be input as a power, number of atoms, or mass within each reservoir. Table 6 shows our default Earth values.

## I. The SpiNBody Module

In addition to the `DistOrb` method described in Section C, orbital evolution can also be modelled using a classic n-body simulation. The `VPLanet` module `SpiNBody` simulates the orbital evolution of a system by calculating the gravitational forces on each body using Newtonian gravity. The gravitational force on an orbital body  $i$  by  $j$  additional bodies is given by:

$$F = \sum_j G \frac{m_i m_j}{r_{i,j}^2}, \quad (\text{I1})$$

where  $G$  is Newton’s gravitational constant,  $m_i$  is the mass of body  $i$ , and  $r_{i,j}$  is the distance

Table 3. Physical and orbital parameters for the system shown in Figs. 21–22.

Parameter	Planet b	Planet c
$m_p (M_\oplus)$	1	18
$r_p (R_\oplus)$	1	1.5
$a (\text{AU})$	0.125	0.2246
$e$	0.1	0.1
$i (\text{°})$	0.5	0.001
$\varpi (\text{°})$	248.87	356.71
$\Omega (\text{°})$	20.68	20
$\epsilon (\text{°})$	45	-
$p_A (\text{°})$	0	-
$Q$	100	-
$k_2$	0.3	-

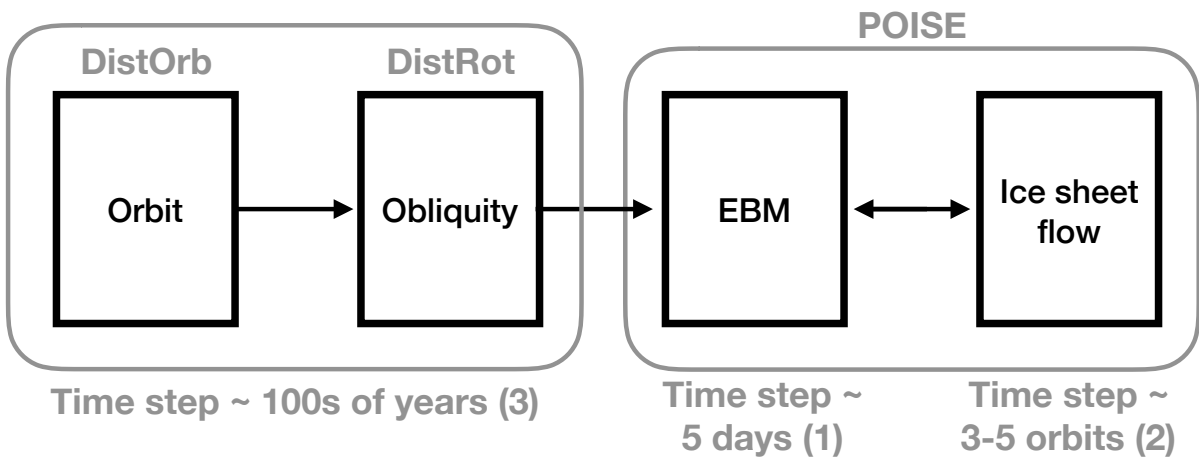


Fig. 29.— Hierarchy of POISE and the orbit and obliquity models. The orbit and obliquity models (`DistOrb` and `DistRot`) are run for  $\sim$  hundreds of years (with an adaptive time step determined by the rates of change of the orbital/obliquity parameters). POISE is run at the end of each orbit/obliquity time step. First, the EBM is run for several orbits, with time steps of  $\sim$  5 days. Then the ice flow model is run with time steps of  $\sim$  3 – 5 orbits. The ice flow model runs until the next orbit/obliquity time step, or until a user-set time, at which point the EBM is rerun for several orbits.

Table 4: **Disturbing function**

Term
D0.1 $f_1 + (h^2 + k^2 + h'^2 + k'^2)f_2 + (p^2 + q^2 + p'^2 + q'^2)f_3$ $+ (h^2 + k^2)^2 f_4 + (h^2 + k^2)(h'^2 + k'^2)f_5 + (h'^2 + k'^2)^2 f_6$ $+ [(h^2 + k^2)(p^2 + q^2) + (h'^2 + k'^2)(p^2 + q^2)$ $+ (h^2 + k^2)(p'^2 + q'^2) + (h'^2 + k'^2)(p'^2 + q'^2)]f_7$ $+ [(p^2 + q^2)^2 + (p'^2 + q'^2)^2]f_8 + (p^2 + q^2)(p'^2 + q'^2)f_9$
D0.2 $(hh' + kk')[f_{10} + (h^2 + k^2)f_{11} + (h'^2 + k'^2)f_{12}$ $+ (p^2 + q^2 + p'^2 + q'^2)f_{13}]$
D0.3 $(pp' + qq')[f_{14} + (h^2 + k^2 + h'^2 + k'^2)f_{15}$ $+ (p^2 + q^2 + p'^2 + q'^2)f_{16}]$
D0.4 $(h^2h'^2 - k^2h'^2 - h^2k'^2 + k^2k'^2 + 4hh'kk')f_{17}$
D0.5 $(h^2p^2 - h^2q^2 - k^2p^2 + k^2q^2 + 4hkpq)f_{18}$
D0.6 $[hh'(p^2 - q^2) - kk'(p^2 - q^2) + 2pq(hk' + kh')]f_{19}$
D0.7 $(h'^2p^2 - h'^2q^2 - k'^2p^2 + k'^2q^2 + 4h'k'pq)f_{20}$
D0.8 $(h^2pp' - h^2qq' - k^2pp' + k^2qq' + 2hkp'q + 2hkp'q')f_{21}$
D0.9 $[(hh' + kk')(pp' + qq') + (hk' - kh')(pq' - qp')]f_{22}$
D0.10 $[(hh' + kk')(pp' + qq') + (hk' - kh')(qp' - pq')]f_{23}$
D0.11 $[(hh' - kk')(pp' - qq') + (hk' + kh')(pq' + qp')]f_{24}$
D0.12 $(h'^2pp' - h'^2qq' - k'^2pp' + k'^2qq' + 2h'k'p'q + 2h'k'pq')f_{25}$
D0.13 $(h^2p'^2 - h^2q'^2 - k^2p'^2 + k^2q'^2 + 4hkp'q')f_{18}$
D0.14 $[hh'(p'^2 - q'^2) - kk'(p'^2 - q'^2) + 2p'q'(hk' + kh')]f_{19}$
D0.15 $(h'^2p'^2 - h'^2q'^2 - k'^2p'^2 + k'^2q'^2 + 4h'k'p'q')f_{20}$
D0.16 $(p^2p'^2 - p^2q'^2 - q^2p'^2 + q^2q'^2 + 4pqp'q')f_{26}$

Table 5: **Stellar properties used in encounter model (reproduced from García-Sánchez et al. 2001)**

Stellar type	$\Delta M_V$	$v_{h,i}$ (km s $^{-1}$ )	$\sigma_{\star i}$ (km s $^{-1}$ )	$n_{\star i}$ (10 $^{-3}$ pc $^{-3}$ )
B0	(-5.7, -0.2)	18.6	14.7	0.06
A0	(-0.2, 1.3)	17.1	19.7	0.27
A5	(1.3, 2.4)	13.7	23.7	0.44
F0	(2.4, 3.6)	17.1	29.1	1.42
F5	(3.6, 4.0)	17.1	36.2	0.64
G0	(4.0, 4.7)	26.4	37.4	1.52
G5	(4.7, 5.5)	23.9	39.2	2.34
K0	(5.5, 6.4)	19.8	34.1	2.68
K5	(6.4, 8.1)	25.0	43.4	5.26
M0	(8.1, 9.9)	17.3	42.7	8.72
M5	(9.9, 18)	23.3	41.8	41.55
WD	-	38.3	63.4	3.00
Giants	-	21.0	41.0	0.43

Table 6: **Initial Radiogenic Properties of Earth**

Isotope	Half-life (Gyr)	Energy/decay (10 $^{-12}$ J)	$Q_{rad,core}(0)$ (TW)	$Q_{rad,man}(0)$ (TW)	$Q_{rad,crust}(0)$ (TW)
$^{26}\text{Al}$	0.717	0.642	0	0	0
$^{40}\text{K}$	1.8178	0.213	33.86	36.16	13.89
$^{232}\text{Th}$	20.202	6.834	0.145	6.52	3.83
$^{235}\text{U}$	1.015	6.555	0.50	20.25	10.39
$^{238}\text{U}$	6.452	8.283	0.12	11.67	5.16

Table 7: Parameters used in the EBM

Variable	Value	Units	Physical description
$C_L$	$1.55 \times 10^7$	$\text{J m}^{-2} \text{K}^{-1}$	land heat capacity
$C_W$	$4.428 \times 10^6$	$\text{J m}^{-2} \text{K}^{-1} \text{m}^{-1}$	ocean heat capacity per meter of depth
$m_d$	70	m	ocean mixing depth
$D$	0.58	$\text{W m}^{-2} \text{K}^{-1}$	meridional heat diffusion coefficient
$\nu$	0.8		coefficient of land-ocean heat flux
$A$	203.3	$\text{W m}^{-2}$	OLR parameter
$B$	2.09	$\text{W m}^{-2} \text{K}^{-1}$	OLR parameter
$\alpha_L$	0.363		albedo of land
$\alpha_W$	0.263		albedo of water
$\alpha_i$	0.6		albedo of ice
$f_L$	0.34		fraction of latitude cell occupied by land
$f_W$	0.66		fraction of latitude cell occupied by water

between body  $i$  and body  $j$ . Thus, the barycentric position and velocity derivatives are given by:

$$\dot{x}_i = v_i \quad (\text{I2})$$

$$\dot{v}_i = \sum_j G \frac{m_j}{r_{i,j}^2} \quad (\text{I3})$$

Because this is an n-body model, it is several orders of magnitude slower than `DistOrb`. Unlike `DistOrb`, however, `SpInBody` can simulate systems of large eccentricity and mutual inclination, as well as systems with orbital resonances. Note, because `SpInBody` uses Cartesian coordinates and derivatives, it cannot currently couple to modules (*e.g.*, `DistOrb` and `EqTide`) that calculate orbital evolution based on the derivatives of the osculating elements. Fig. 30 shows the evolution of Earth’s orbit due to the Sun and other 7 planets for both `VPLanet` in black, and `HNBody` in red.

## J. The STELLAR Module

The `STELLAR` module simulates the evolution of the stellar radius, radius of gyration ( $r_g$ ), effective temperature, luminosity, XUV luminosity, and rotation rate over time. `STELLAR`

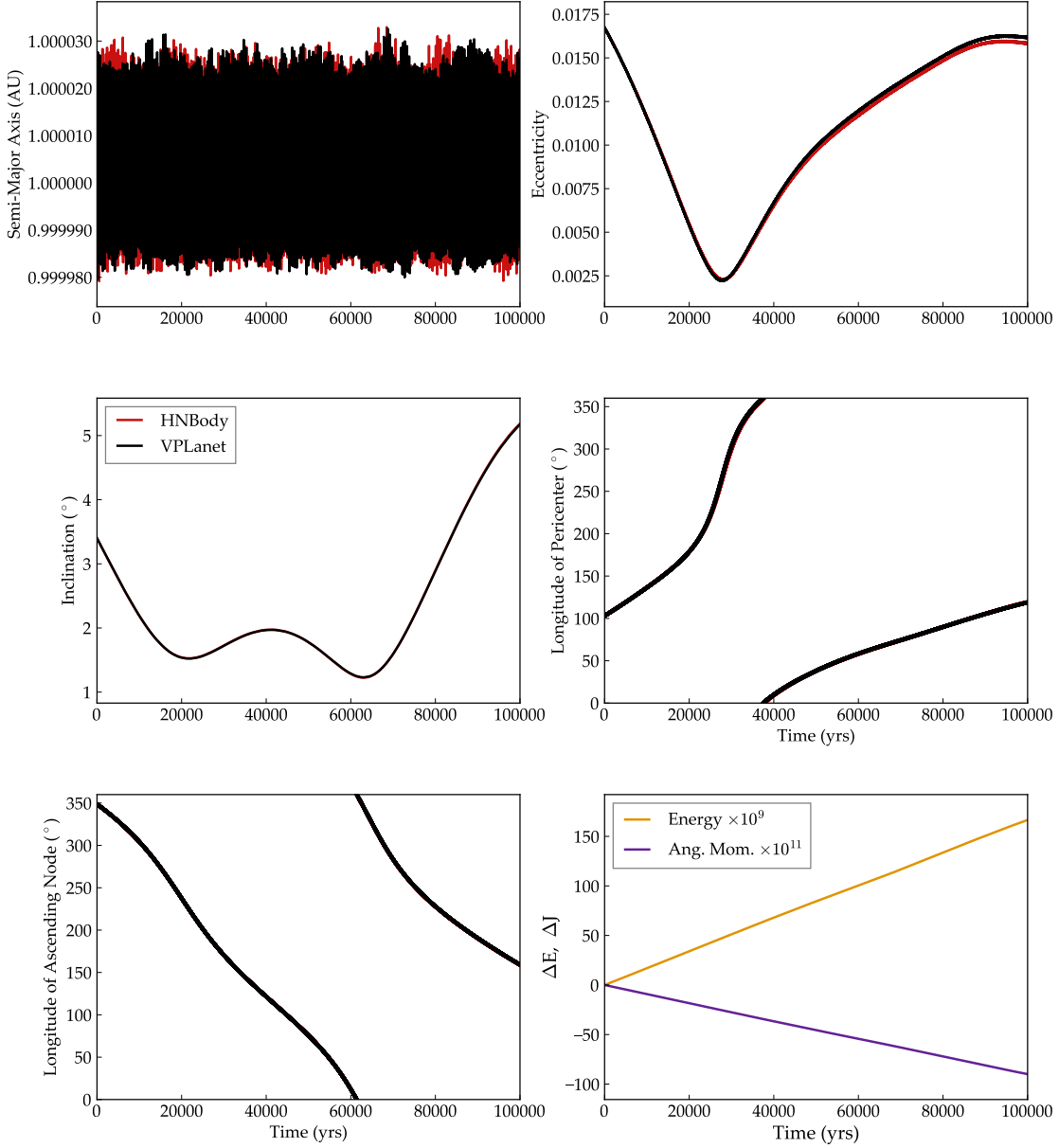


Fig. 30.— Evolution of Earth’s orbit according to `SpInBody` (black) and `HNBODY` (red). The two trajectories are nearly identical. The bottom right panel shows the conservation of energy ( $\Delta E$ ) and angular momentum ( $\Delta J$ ) for `SpInBody` only. [examples/SS\\_NBody](#).

Table 8: Parameters used in the ice sheet model

Variable	Value	Units	Physical description
$T_{freeze}$	273.15	K	freezing point of water
$L_h$	$3.34 \times 10^5$	J kg $^{-1}$	latent heat of fusion of water
$r_{\text{snow}}$	$2.25 \times 10^{-5}$	kg m $^{-2}$ s $^{-1}$	snow/ice deposition rate
$A_{\text{ice}}$	$2.3 \times 10^{-24}$	Pa $^{-3}$ s $^{-1}$	deformability of ice
$n$	3		exponent of Glen’s flow law
$\rho_i$	916.7	kg m $^{-3}$	density of ice
$\rho_s$	2390	kg m $^{-3}$	density of saturated sediment
$\rho_w$	1000	kg m $^{-3}$	density of liquid water
$D_0$	$7.9 \times 10^{-7}$	s $^{-1}$	reference sediment deformation rate
$\mu_0$	$3 \times 10^9$	Pa s	reference sediment viscosity
$m$	1.25		exponent in sediment stress-strain relation
$h_s$	10	m	sediment depth
$\phi_s$	22	degrees	internal deformation angle of sediment
$T_b$	5000	years	bedrock depression/ rebound timescale
$\rho_b$	3370	kg m $^{-3}$	bedrock density

evolves the four former quantities using a bicubic spline interpolation over mass and time of the evolutionary tracks of Baraffe et al. (2015) for solar-metallicity stars. **STELLAR** tracks the XUV luminosity of stars using the empirical broken power law model of Ribas et al. (2005),

$$\frac{L_{\text{XUV}}}{L_{\text{bol}}} = \begin{cases} f_{\text{sat}} & t \leq t_{\text{sat}} \\ f_{\text{sat}} \left( \frac{t}{t_{\text{sat}}} \right)^{-\beta_{\text{XUV}}} & t > t_{\text{sat}}, \end{cases} \quad (\text{J1})$$

where  $L_{\text{bol}}$  is the total (bolometric) stellar luminosity, *i.e.*, from the Baraffe et al. (2015) grids,  $\beta_{\text{XUV}}$  is the power law exponent (equal to  $-1.23$  for Sun-like stars; Ribas et al. 2005), and  $f_{\text{sat}}$  is the initial (constant) ratio of XUV to bolometric luminosity. Prior to  $t = t_{\text{sat}}$ , the XUV luminosity is said to be “saturated,” as observations show that the ratio  $L_{\text{XUV}}/L_{\text{bol}}$  remains relatively constant at early times (*e.g.*, Wright et al. 2011). For G and K dwarfs,  $t_{\text{sat}} \approx 100$  Myr and  $f_{\text{sat}} \approx 10^{-3} - 10^{-4}$  (Jackson et al. 2012). Because of poor constraints on the ages of field M dwarfs, the saturation timescale for these stars is not known, although it is likely longer than that for K dwarfs. Following Luger & Barnes (2015), we adopt  $t_{\text{sat}} = 1$  Gyr and  $f_{\text{sat}} = 10^{-3}$  as default values in **STELLAR**.

In addition to tracking the evolution of fundamental stellar properties, **STELLAR** models the angular momentum evolution of stars undergoing stellar evolution, *e.g.*, radius contrac-

tion, and angular momentum loss due to magnetic braking. We allow the user to model magnetic braking using three different prescriptions from Reiners & Mohanty (2012), Repetto & Nelemans (2014), and Matt et al. (2015), with the latter including the corrections of Matt et al. (2019).

The Reiners & Mohanty (2012) magnetic braking model, which links angular momentum loss with stellar magnetic field strength, is given by

$$\begin{aligned} \frac{dJ_\star}{dt} &= -C \left[ \omega \left( \frac{R^{16}}{M^2} \right)^{1/3} \right] \text{ for } \omega \geq \omega_{crit} \\ \frac{dJ_\star}{dt} &= -C \left[ \left( \frac{\omega}{\omega_{crit}} \right)^4 \omega \left( \frac{R^{16}}{M^2} \right)^{1/3} \right] \text{ for } \omega < \omega_{crit}, \end{aligned} \quad (\text{J2})$$

where  $C = 2.66 \times 10^3$  ( $\text{gm}^5 \text{ cm}^{-10} \text{ s}^3$ ) $^{1/3}$ ,  $\omega_{crit} = 8.56 \times 10^{-6} \text{ s}^{-1}$  for  $M > 0.35 \text{ M}_\odot$ , and  $\omega_{crit} = 1.82 \times 10^{-6} \text{ s}^{-1}$  for  $M \leq 0.35 \text{ M}_\odot$ . In this model, the dichotomy between unsaturated ( $\omega < \omega_{crit}$ ) and saturated ( $\omega \geq \omega_{crit}$ ) assumes that for fast enough rotation rates, *i.e.*, the stars in the “saturated” regime, the stellar magnetic field strength is constant, whereas in the unsaturated regime, the stellar magnetic field strength depends on the rotation rate. The Repetto & Nelemans (2014) model is simply based off of the observed spin-down of Sun-like stars by Skumanich (1972) and is given by

$$\frac{dJ_\star}{dt} = -\gamma M r_g^2 R^4 \omega^3, \quad (\text{J3})$$

where  $\gamma = 5 \times 10^{-25} \text{ s m}^{-2}$ . STELLAR also allows the user to select the Matt et al. (2015) magnetic braking model that was used to successfully reproduce observed features in the rotation period distribution of *Kepler* field stars. The Matt et al. (2015) model is based on scaling relations with the stellar mass, radius, and Rossby number, the ratio of the convective turnover timescale to the rotation period, and is given by the following equations:

$$\begin{aligned} \frac{dJ_\star}{dt} &= -T_0 \left( \frac{\tau_{cz}}{\tau_{cz\odot}} \right)^2 \left( \frac{\omega_\star}{\omega_\odot} \right)^3, \text{ (unsaturated)} \\ \frac{dJ_\star}{dt} &= -T_0 \chi^2 \left( \frac{\omega_\star}{\omega_\odot} \right), \text{ (saturated)} \end{aligned} \quad (\text{J4})$$

where  $\tau_{cz}$  is the convective turnover timescale,  $\tau_{cz\odot}$  is the solar convective turnover timescale, 12.9 days, and

$$\chi = \frac{\text{Ro}_\odot}{\text{Ro}_{sat}} = \frac{\omega_{sat} \tau_{cz}}{\omega_\odot \tau_{cz\odot}} \quad (\text{J5})$$

is the inverse critical Rossby number for saturation in solar units. Matt et al. (2015) finds that saturation occurs when  $\text{Ro} \leq \text{Ro}_\odot / \chi$ , where  $\chi = 10$ . The normalized torque is given by

$$T_0 = 6.3 \times 10^{23} \text{ Joules} \left( \frac{R}{R_\odot} \right)^{3.1} \left( \frac{M}{M_\odot} \right)^{0.5}. \quad (\text{J6})$$

We compute  $\tau_{cz}$  using the fit presented in Cranmer & Saar (2011), given by

$$\tau_{cz} = 314.24 \exp \left[ - \left( \frac{T_{eff}}{1952.5 \text{ K}} \right) - \left( \frac{T_{eff}}{6250 \text{ K}} \right)^{18} \right] + 0.002 \quad (\text{J7})$$

for stellar effective temperature  $T_{eff}$ .

We model the total change in a star’s rotation rate,  $\omega$  due to radius and  $r_g$  evolution, assuming conservation of angular momentum, and magnetic braking according to

$$\dot{\omega} = \frac{\dot{J}_\star}{I} - \frac{2\dot{R}\omega}{R} - \frac{2r_g\dot{\omega}}{r_g} \quad (\text{J8})$$

for a star’s moment of inertia,  $I = mr_g^2R^2$ . We compute numerical time derivatives of the stellar radius and  $r_g$  using our interpolation of the Baraffe et al. (2015) grids and  $\dot{J}_\star$  is the angular momentum loss due to magnetic braking given by one of the above models. In Fig. 31, we plot the rotation period evolution for late M-dwarfs and Sun-like stars subject to Eq. (J8) for the three magnetic braking models implemented in vPLanet.

## K. The ThermInt Module

The thermal history of the interior is determined by the time evolution of the average mantle  $T_m$  and average core  $T_c$  temperatures. The energetic state of the core governs inner core crystallization and the dynamo.

### K.1. Governing Differential Equations

The conservation of energy in the mantle is

$$Q_{surf} = Q_{conv} + Q_{melt} = Q_{i,man} + Q_{cmb} + Q_{man} + Q_{tidal} + Q_{L,man}, \quad (\text{K1})$$

where  $Q_{surf}$  is the total mantle surface heat flow,  $Q_{conv}$  is heat conducted through the lithospheric thermal boundary layer that is supplied by mantle convection,  $Q_{melt}$  is heat loss due to the eruption of upwelling mantle melt at the surface,  $Q_{i,man}$  is heat generated by radioactive decay of species  $i$  in the mantle,  $Q_{cmb}$  is heat lost from the core across the core-mantle boundary (CMB),  $Q_{man}$  is the secular heat lost from the mantle,  $Q_{tidal}$  is heat generated in the mantle by tidal dissipation, and  $Q_{L,man}$  is latent heat released by the solidification of the mantle. Crustal heat sources have been excluded because they do not contribute to the mantle heat budget. Note that heat can be released from the mantle in two

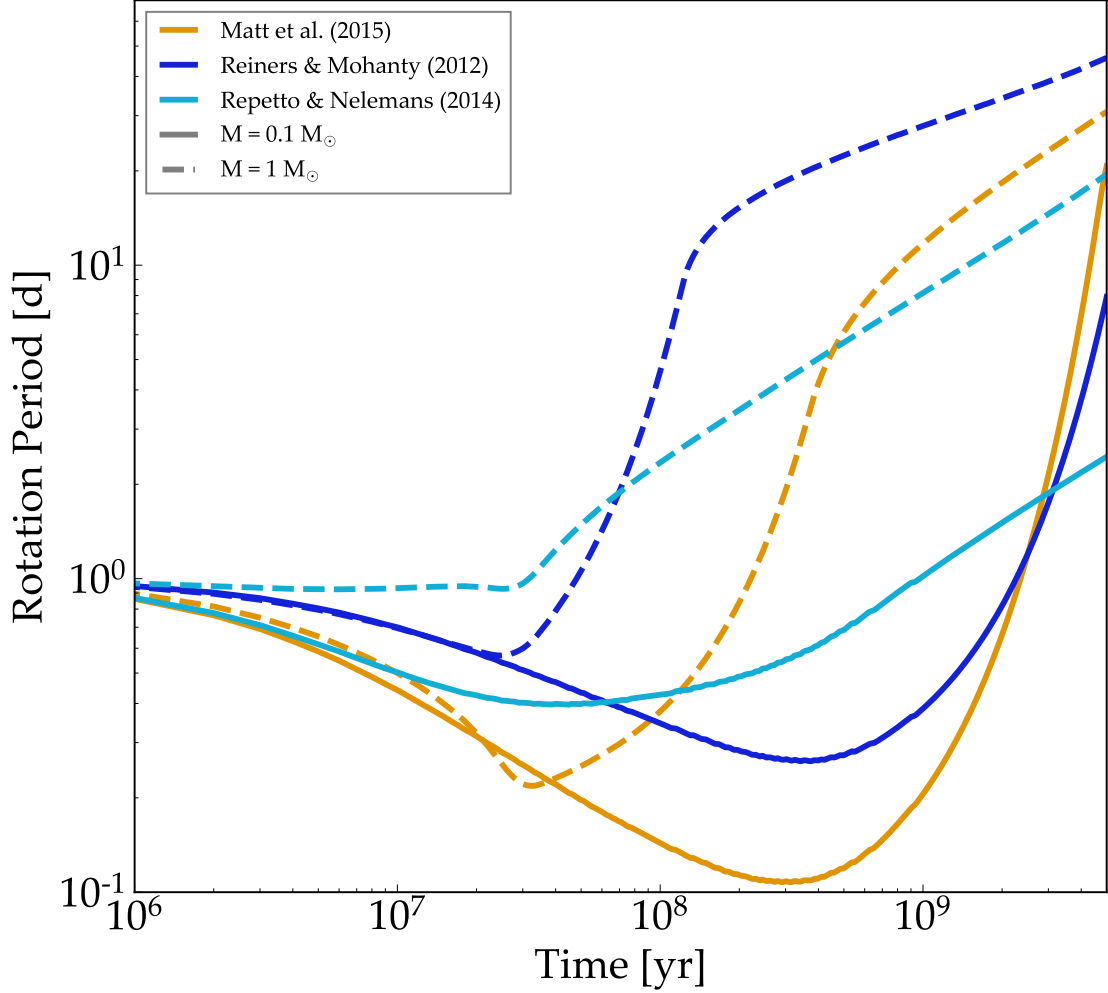


Fig. 31.— Rotation period evolution for  $0.1M_{\odot}$  (late M dwarf, solid lines) and  $1M_{\odot}$  (Sun-like star, dashed lines) mass stars evolved using `STELLAR` according to Eq. (J8) for the Matt et al. (2015) (blue), Reiners & Mohanty (2012) (orange), and Repetto & Nelemans (2014) magnetic braking models. Initially as the stars contract along the pre-main sequence, the rotation periods decrease via conservation of angular momentum. Once the stars reach the main sequence, stellar radii and  $r_g$  remain mostly constant allowing magnetic braking to remove angular momentum from the stars, increasing rotation periods in the long terms.

[examples/MagneticBraking](#)

ways: via conduction through the upper mantle thermal boundary layer ( $Q_{conv}$ ) and by melt eruption ( $Q_{melt}$ ). Detailed expressions for heat flows and temperature profiles as functions of mantle and core properties are given below.

Similarly, the thermal evolution of the core is governed by the conservation of energy in the core,

$$Q_{cmb} = Q_{core} + Q_{icb} + Q_{i,core} \quad (\text{K2})$$

where  $Q_{core}$  is core secular cooling,  $Q_{i,core}$  is radiogenic heat production of species  $i$  in the core, and heat released by the solidification of the inner core is  $Q_{icb} = \dot{M}_{ic}(L_{icb} + E_{icb})$ , where  $\dot{M}_{ic}$  is the change in inner core mass  $M_{ic}$ , and  $L_{icb}$  and  $E_{icb}$  are the latent and gravitational energy released per unit mass at the inner-core boundary (ICB).

Thermal evolution equations for the average mantle  $T_m$  and core  $T_c$  temperatures are derived by using the secular cooling equation  $Q_j = -c_j M_i \dot{T}_j$ , where  $c$  is specific heat and  $j$  refers to either mantle or core, in Eqs. (K1) and (K2). Solving for  $\dot{T}_m$  and  $\dot{T}_c$  gives the mantle and core thermal evolution equations,

$$\dot{T}_m = (Q_{cmb} + Q_{i,man} + Q_{tidal} + Q_{L,man} - Q_{conv} - Q_{melt}) / M_m c_m \quad (\text{K3})$$

$$\dot{T}_c = -\frac{(Q_{cmb} - Q_{i,core})}{M_c c_c - A_{ic} \rho_{ic} \eta_c \frac{dR_{ic}}{dT_{cmb}} (L_{Fe} + E_G)} \quad (\text{K4})$$

where the denominator of (K4) is the sum of core specific heat and heat released by the inner core growth,  $A_{ic}$  is inner core surface area,  $\rho_{ic}$  is inner core density,  $\eta_c$  is a constant that relates average core temperature to CMB temperature,  $dR_{ic}/dT_{cmb}$  is the rate of inner core growth as a function of CMB temperature, and  $L_{Fe}$  and  $E_G$  are the latent and gravitational energy released at the ICB per unit mass. Table 9 lists the values for these parameters, which are taken from McKenzie (1984), McKenzie & Bickle (1988), Hirschmann (2000), Elkins-Tanton (2008), Barnes et al. (2013), and Jaupart et al. (2015).

An additional conservation of energy can be added for the cooling of the lithosphere for a stagnant lid planet. Alternatively, the stagnant lid heat flow can be approximated by

$$Q_{conv,stagn} = \epsilon_{stag} Q_{conv} \quad (\text{K5})$$

where  $\epsilon_{stag} \approx 1/25$ .

## K.2. Mantle Rheology

Effective mantle viscosity follows an Arrhenius Law form,

$$\nu = \nu_{ref} \exp \left( \frac{E_\nu}{R_g T} \right) / \epsilon_{phase} \quad (\text{K6})$$

where  $\nu = \eta/\rho_m$  is kinematic viscosity,  $\rho_m$  is mantle density,  $\nu_{ref}$  is a reference viscosity,  $E_\nu$  is the viscosity activation energy,  $R_g$  is the gas constant,  $T$  is either upper or lower mantle temperature, and  $\epsilon_{phase}$  accounts for the weakening effect of a solid to liquid phase change (see Table 9 for a list of constants). Shear modulus, which is required to calculate tidal heating (see App. K.3), is similarly described,

$$\mu = \mu_{ref} \exp \left( \frac{E_\mu}{R_g T_m} \right) / \epsilon_{phase}. \quad (\text{K7})$$

This model predicts the rapid drop in shear modulus with melt fraction demonstrated experimentally by Jackson et al. (2004). The reference shear modulus  $\mu_{ref} = 6.24 \times 10^4$  Pa and effective stiffness  $\beta_{st} = 1.71 \times 10^4$  GPa are calibrated by  $k_2 = 0.3$  and  $Q = 100$  for the present-day mantle.

The influence of melt fraction  $\phi$  on viscosity is modeled following the parameterization of Costa et al. (2009),

$$\epsilon_{phase}(\phi) = \frac{1 + \Phi^{\delta_{ph}}}{[1 - F]^{B\phi^*}} \quad (\text{K8})$$

where

$$F = (1 - \xi) \operatorname{erf} \left[ \frac{\sqrt{\pi}}{2(1 - \xi)} \Phi (1 + \Phi^{\gamma_{ph}}) \right] \quad (\text{K9})$$

and  $\Phi = \phi/\phi^*$ , and  $\phi^*$ ,  $\xi$ ,  $\gamma_{ph}$ , and  $\delta_{ph}$  are empirical constants (Table 9). The nominal value of  $A_\mu = 2 \times 10^5$  **jmol** produces a dissipation peak when melt fraction is about 50%. **What is jmol?**

The mid-mantle and lower mantle viscosities can be related to the upper mantle viscosity by

$$\nu_{man} = f_{\nu,man} \nu_{UM}, \quad \nu_{LM} = f_{\nu,LM} \nu_{UM} \quad (\text{K10})$$

where  $f_{\nu,man}$  and  $f_{\nu,LM}$  are constant coefficients. The mantle Rayleigh number is

$$Ra_{man} = \frac{\alpha g \Delta T_{man} D_{man}^3}{\kappa \nu_{man}} \quad (\text{K11})$$

where  $\alpha$  is thermal expansivity,  $D_{man} = R - R_{cmb}$  is mantle shell thickness,  $\kappa$  is thermal diffusivity, and mantle convective temperature jump is,

$$\Delta T_{man} = \Delta T_{UM} + \Delta T_{LM} = (T_{UM} - T_g) + (T_{cmb} - T_{LM}) \quad (\text{K12})$$

where  $T_{UM}$  and  $\Delta T_{UM}$  are the temperatures at the bottom of and across the upper mantle thermal boundary layer;  $T_{LM}$  and  $\Delta T_{LM}$  are the temperatures at the top of and across the lower mantle thermal boundary layer;  $T_{cmb}$  is CMB temperature.

### K.3. Tidal Heating

Tidal heating associated with gravitational tides is assumed to occur by visco-elastic dissipation in the mantle. The power dissipated by tidal strain in a planet in synchronous rotation is (Segatz et al. 1988; Driscoll & Barnes 2015),

$$Q_{tidal} = -\frac{21}{2} \text{Im}(k_2) \frac{GM_*^2 R_p \omega e^2}{a^6} \quad (\text{K13})$$

where  $G$  is the gravitational constant,  $M_*$  is stellar mass,  $R_p$  is planet radius,  $\omega$  is orbital frequency,  $e$  is orbital eccentricity,  $a$  is orbital semi-major axis, and  $\text{Im}(k_2)$  is the imaginary part of the complex second order love number  $k_2$ . If planetary rotation is synchronous then the tidal frequency is equal to the mean motion  $\omega = n = \sqrt{GM_*/a^3}$ , and the tidal power reduces to

$$Q_{tidal} = -\frac{21}{2} \text{Im}(k_2) G^{3/2} M_*^{5/2} R_p \frac{e^2}{a^{15/2}}. \quad (\text{K14})$$

This expression for tidal dissipation is the product of three physical components: (1) tidal efficiency ( $-\text{Im}(k_2)$ ), (2) star-planet size ( $M_*^{5/2} R_p$ ), and (3) orbit ( $e^2/a^{15/2}$ ).

The one-dimensional dissipation model in Eq. (K14) assumes a homogeneous body with uniform stiffness and viscosity. We assume that dissipation is dominated by the material properties at the base of the upper mantle thermal boundary layer where viscosity is expected to be at a minimum in the mantle. To derive the dissipation efficiency ( $-\text{Im}(k_2)$ ) we first define the Love number,

$$k_2 = \frac{3}{2} \frac{1}{1 + \frac{19}{2} \frac{\mu}{\beta_{st}}}, \quad (\text{K15})$$

where  $\mu$  is shear modulus and  $\beta_{st}$  is effective stiffness. Writing shear modulus as a complex number and using the constitutive relation for a Maxwell body, one can derive the dissipation efficiency in Eq. (K14) as

$$-\text{Im}(k_2) = \frac{57\eta\omega}{4\beta_{st} \left( 1 + \left[ \left( 1 + \frac{19\mu}{2\beta_{st}} \right) \frac{\eta\omega}{\mu} \right]^2 \right)} \quad (\text{K16})$$

where  $\eta = \nu\rho$  is dynamic viscosity (Henning et al. 2009). We note that this model does not involve a tidal  $Q$  factor, rather the rheological response of the mantle is described entirely by  $\text{Im}(k_2)$ . For comparison with other models, one can compute the standard tidal  $Q$  factor of the Maxwell model as

$$Q = \frac{\eta\omega}{\mu}. \quad (\text{K17})$$

The common approximation is then  $-\text{Im}(k_2) \approx k_2/Q$ .

#### K.4. Geotherm

The mantle temperature profile is assumed to be adiabatic everywhere except in the thermal boundary layers where it is conductive. The adiabatic temperature profile in the well mixed region of the mantle is approximated to be linear in radius, which is a good approximation considering that mantle thickness  $D = 2891$  km is significantly less than the adiabatic scale height  $H = c_p/\alpha g \approx 12650$  km,

$$T_{ad} = T_{UM} + \gamma_{ad}(R - r - \delta_{UM}) , \quad (K18)$$

where the solid adiabatic gradient is  $\gamma_{ad} \approx 0.5$  K/km. In the thermal boundary layers the conductive temperature solutions,

$$\Delta T_{UM} \operatorname{erf} \left[ \frac{R - r}{\delta_{UM}} \right] + T_g , \quad \text{Upper mantle} \quad (K19)$$

$$\Delta T_{LM} \operatorname{erf} \left[ \frac{R_c - r}{\delta_{LM}} \right] + T_{cmb} , \quad \text{Lower mantle} \quad (K20)$$

replace the adiabat. Thermal boundary layer temperature jumps are  $\Delta T_{UM} = T_{UM} - T_g$  and  $\Delta T_{LM} = T_{cmb} - T_{LM}$ ,  $T_g$  is ground temperature, and thermal boundary layer depth is  $\delta$ .

The core temperature profile is assumed to be adiabatic throughout the entire core, and the thermal boundary layers within the core are ignored. This approximation is valid because the low viscosity and high thermal conductivity of liquid iron produce very small thermal boundary layers that are insignificant. The core adiabatic profile is approximated by

$$T_c(r) = T_{cmb} \exp \left( \frac{R_c^2 - r^2}{D_N^2} \right) , \quad (K21)$$

where  $D_N \approx 6340$  km is an adiabatic length scale (Labrosse et al. 2001). The iron solidus is approximated by Lindemann’s Law,

$$T_{Fe}(r) = T_{Fe,0} \exp \left[ -2 \left( 1 - \frac{1}{3\gamma_c} \right) \frac{r^2}{D_{Fe}^2} \right] - \Delta T_x , \quad (K22)$$

where  $T_{Fe,0} = 5600$  K,  $\gamma_c$  is the core Gruneisen parameter,  $D_{Fe} = 7000$  km is a constant length scale (Labrosse et al. 2001), and  $\Delta T_x$  is a liquidus depression due to the presence of a light element. If  $\Delta T_x = 0$  then the inner core radius can then be written as a function of CMB temperature by equating Eqs. (K21) and (K22) and solving for  $r = R_{ic}$ , giving

$$R_{ic} = R_c \sqrt{\frac{(D_N/R_c)^2 \ln(T_{cmb}/T_{Fe,cen}) + 1}{(D_N/R_c)^2 \ln(T_{Fe,cmb}/T_{Fe,cen}) + 1}} \quad (K23)$$

where  $T_{cmb}$  is CMB temperature,  $T_{Fe,cen}$  is the liquidus at the center of the core, and  $T_{Fe,CMB}$  is the liquidus at the CMB. The time derivative of Eq. (K23) gives the rate of inner core growth as a function of core cooling rate  $\dot{T}_c$  as,

$$\dot{R}_{ic} = \frac{D_N^2/(2R_{ic})}{(D_N/R_c)^2 \ln(T_{Fe,cmb}/T_{Fe,cen}) + 1} \frac{\dot{T}_c}{T_c} \quad (\text{K24})$$

Assuming a constant inner core density  $\rho_{ic}$ , inner core mass growth rate is approximated by

$$\dot{M}_{ic} = A_{ic}\rho_{ic}\dot{T}_{cmb} \frac{dR_{ic}}{dT_{cmb}} \quad (\text{K25})$$

where  $A_{ic}$  is the area of the inner core and the change in inner core radius with CMB temperature can be computed by the temperature derivative of Eq. (K23), giving

$$\frac{dR_{ic}}{dT_{cmb}} = \frac{\dot{R}_{ic}}{\dot{T}_c} = \frac{D_N^2/(2R_{ic})}{T_{cmb}[(D_N/R_c)^2 \ln(T_{Fe,cmb}/T_{Fe,cen}) + 1]} \quad (\text{K26})$$

## K.5. Mantle and Core Heat Flows

In this subsection we define the remaining heat flows that appear in the mantle and core energy balance, Eqs. (K1)–(K2). The convective cooling of the mantle  $Q_{conv}$  is proportional to the temperature gradient in the upper mantle thermal boundary layer,

$$Q_{conv} = Ak_{UM} \frac{\Delta T_{UM}}{\delta_{UM}} , \quad (\text{K27})$$

where  $A$  is surface area and  $k_{UM}$  is upper mantle thermal conductivity.  $Q_{conv}$  is written in terms of  $T_m$  and the thermal boundary layer thickness  $\delta_{UM}$  by requiring that the Rayleigh number of the boundary layer  $Ra_{UM}$  be equal to the critical Rayleigh number for thermal convection  $Ra_c \approx 660$  (Howard 1966; Solomatov 1995; Sotin & Labrosse 1999; Driscoll & Bercovici 2014). Solving for the critical thermal boundary layer thickness from  $Ra_{UM} = Ra_c$  gives,

$$\delta_{UM} = D \left( Ra_c \frac{\nu_{UM} \kappa}{\alpha g \Delta T_{UM} D^3} \right)^\beta \quad (\text{K28})$$

Using this relationship in Eq. (K27) gives,

$$Q_{conv} = Ak_{UM} \left( \frac{\alpha g}{Ra_c \kappa} \right)^\beta \frac{(\epsilon_{UM} \Delta T_m)^{\beta+1}}{\nu_{UM}^\beta} , \quad (\text{K29})$$

where the thermal boundary layer temperature jump  $\Delta T_{UM}$  has been replaced by  $\Delta T_{UM} \approx \epsilon_{UM} \Delta T_m$ ,  $\epsilon_{UM} = \exp(-(R_{UM} - R_m) \alpha g / c_p) \approx 0.7$ , which is the adiabatic temperature decrease from the average mantle temperature to the bottom of the upper mantle thermal boundary layer,  $\Delta T_m = T_m - T_g$ , and the mantle cooling exponent is  $\beta = 1/3$ .

Similar to the mantle convective heat flow, the CMB heat flow is,

$$Q_{cmb} = A_c k_{LM} \frac{\Delta T_{LM}}{\delta_{LM}} , \quad (\text{K30})$$

where  $A_c$  is core surface area and  $k_{LM}$  is lower mantle thermal conductivity. The lower mantle and CMB temperatures,  $T_{LM}$  and  $T_{cmb}$ , are extrapolations along the mantle and core adiabats:  $T_{LM} = \epsilon_{LM} T_m$  and  $T_{cmb} = \epsilon_c T_c$ , where  $\epsilon_{LM} = \exp(-(R_{LM} - R_m) \alpha g / c_p) \approx 1.3$  and  $\epsilon_c \approx 0.8$ . Analogous to Eq. (K28) the lower mantle thermal boundary layer thickness  $\delta_{LM}$  is derived by assuming the boundary layer Rayleigh number is critical, giving

$$\delta_{LM} = \left( \frac{\kappa \nu_{LM}}{\alpha g \Delta T_{LM}} Ra_c \right)^{1/3} \quad (\text{K31})$$

Core secular cooling is

$$Q_{core} = -M_c c_c \dot{T}_c , \quad (\text{K32})$$

where  $M_c$  is core mass,  $c_c$  is core specific heat, and  $\dot{T}_c$  is the rate of change of the average core temperature  $T_c$ .

## K.6. Mantle Melting

The mantle solidus is approximated by a third-order polynomial (Elkins-Tanton 2008),

$$T_{sol}(r) = A_{sol} r^3 + B_{sol} r^2 + C_{sol} r + D_{sol} , \quad (\text{K33})$$

where the coefficients are constants (see Table 9). This solidus is calibrated to fit the following constraints: solidus temperature of 1450 K at the surface, solidus temperature of 4150 K at the CMB (Andrault et al. 2011), and present-day upwelling melt fraction of  $f_{melt} = 8\%$ . The liquidus is assumed to be hotter by a constant offset  $\Delta T_{liq} = 500$  K, so  $T_{liq}(r) = T_{sol}(r) + \Delta T_{liq}$ .

Mantle melt heat loss (or advective heat flow) is modeled as,

$$Q_{melt} = \epsilon_{erupt} \dot{M}_{melt} (L_{melt} + c_m \Delta T_{melt}) , \quad (\text{K34})$$

where  $\epsilon_{erupt} = 0.2$  is the assumed efficiency of magma eruption to Earth's surface,  $\dot{M}_{melt}$  is melt mass flux (see below),  $L_{melt}$  is latent heat of the melt,  $c_m$  is specific heat of the melt, and  $\Delta T_{melt}$  is the excess temperature of the melt at the surface (see below). The latent heat released by mantle melting does not contribute to the cooling of the mantle. This formulation of heat loss is similar to the “heat pipe” mechanism invoked for Io (O'Reilly &

Davies 1981; Moore 2003), where melt eruption is a significant source of heat loss. We note that this mechanism is more important for stagnant lid planets where the normal conductive heat flow is lower (Driscoll & Bercovici 2014).

The melt mass flux  $\dot{M}_{melt}$  is the product of the upwelling solid mass flux times the melt mass fraction  $f_{melt}$ ,

$$\dot{M}_{melt} = \dot{V}_{up}\rho_{solid}f_{melt}(z_{UM}) , \quad (\text{K35})$$

where solid density is  $\rho_{solid}$ , volumetric upwelling rate is  $\dot{V}_{up} = 1.16\kappa A_p/\delta_{UM}$ ,  $z_{UM} = R - \delta_{UM}$ , and melt fraction is

$$f_{melt}(z) = \frac{T_m(z) - T_{sol}}{T_{liq} - T_{sol}} . \quad (\text{K36})$$

This model predicts a ridge melt production of  $\dot{M}_{melt} = 2.4 \times 10^6 \text{ kg s}^{-1}$  for  $\delta_{UM} = 80 \text{ km}$  and  $f_{melt} = 0.1$ , similar to present-day global melt production estimates (Cogné & Humler 2004).

We define the magma ocean as the region of the mantle with temperature exceeding the liquidus. Given the geotherm in Eqs. (K18) and (K20) and the liquidus  $T_{liq}(r)$  similar to Eq. (K33), the mantle will mainly freeze from the bottom of the convecting mantle up because the liquidus gradient is steeper than the adiabat (*e.g.*, Elkins-Tanton 2012). However, if the core is hot enough a second melt region exists in the lower mantle boundary layer, where the temperature gradient exceeds the liquidus and the mantle freezes towards the CMB.

Latent heat released from the solidification of the mantle is

$$Q_{L,man} = \dot{M}_{sol}L_{melt} , \quad (\text{K37})$$

where  $L_{melt}$  is the latent heat released per kg and  $\dot{M}_{sol}$  is the solid mantle growth rate. The growth rate is calculated assuming a uniform mantle density  $\rho_m$  so that  $\dot{M}_{sol} = \rho_m \dot{V}_{sol}$ , where  $\dot{V}_{sol} = -\dot{V}_{liq}$ . The rate of change of the liquid volume of the mantle is approximated by

$$\dot{V}_{liq} = \frac{dV_{liq}}{dT_m} \dot{T}_m , \quad (\text{K38})$$

where  $\dot{T}_m$  is the mantle secular cooling rate and  $dV_{liq}/dT_m$  is linearly approximated by  $8 \times 10^{17} \text{ m}^3 \text{ K}^{-1}$ , which is the change in liquid volume from a 90% liquid to a completely solid mantle. This approximation implies that the latent heat released due to mantle solidification is linearly proportional to the mantle secular cooling rate, and the ratio of the latent heat flow to the mantle secular cooling heat flow is  $Q_{L,man}/Q_{sec,m} \approx 0.24$ . For example, a mantle solidification time of 100 Myr corresponds to an average latent heat release of  $Q_{L,man} \approx 400 \text{ TW}$  over that time.

### K.7. Core Dynamo

Given the thermal cooling rate of the core, the magnetic dipole moment  $\mathcal{M}$  is estimated from the empirical scaling law,

$$\mathcal{M} = 4\pi R_c^3 \gamma_d \sqrt{\rho/2\mu_0} (F_c D_c)^{1/3}, \quad (\text{K39})$$

where  $\gamma_d$  is the saturation constant for fast rotating dipolar dynamos,  $\mu_0 = 4\pi \times 10^{-7} \text{ H m}^{-1}$  is magnetic permeability,  $D_c = R_c - R_{ic}$  is the dynamo region shell thickness,  $R_c$  and  $R_{ic}$  are outer and inner core radii, respectively, and  $F_c$  is the core buoyancy flux (Olson & Christensen 2006). We assume that the field is dipolar, ignoring the complicating influences of shell thickness and heterogeneous boundary conditions. In this formulation a positive buoyancy flux implies dynamo action, which is a reasonable approximation when the net buoyancy flux is large, but may overestimate the field strength at low flux. The total core buoyancy flux  $F_c$  is the sum of thermal and compositional buoyancy fluxes,

$$F_c = F_{th} + F_\chi, \quad (\text{K40})$$

where the thermal and compositional buoyancy fluxes are

$$F_{th} = \frac{\alpha_c g_c}{\rho_c c_c} q_{c,conv}, \quad (\text{K41})$$

$$F_\chi = g_i \frac{\Delta \rho_\chi}{\rho_c} \left( \frac{R_{ic}}{R_c} \right)^2 \dot{R}_{ic}, \quad (\text{K42})$$

where the subscript  $c$  refers to bulk core properties, core convective heat flux is  $q_{c,conv} = q_{cmb} - q_{c,ad}$ , gravity at the ICB is approximated by  $g_{ic} = g_c R_{ic}/R_c$ , and the outer core compositional density difference is  $\Delta \rho_\chi = \rho_c - \rho_\chi$  with  $\rho_\chi$  the light element density. For simplicity, the expression for light element buoyancy Eq. (K42) ignores buoyancy due to latent heat release at the ICB because it is a factor of 3.8 less than buoyancy of the light elements.

The isentropic core heat flux at the CMB, proportional to the gradient of Eq. (K21), is

$$q_{c,ad} = k_c T_{cmb} R_c / D_N^2, \quad (\text{K43})$$

where core thermal conductivity is approximated by the Wiedemann-Franz law,

$$k_c = \sigma_c L_c T_{cmb}, \quad (\text{K44})$$

and electrical conductivity is  $\sigma_c$  and  $L_c$  is the Lorentz number. For typical values of high pressure-temperature iron,  $\sigma_c = 10 \times 10^5 \Omega^{-1} m^{-1}$  (Pozzo et al. 2012; Gomi et al. 2013),  $L_c = 2.5 \times 10^{-8} \text{ W}\Omega\text{K}^{-1}$ , and  $T_{cmb} = 4000 \text{ K}$ , the core thermal conductivity is  $k_c = 100 \text{ Wm}^{-1}\text{K}^{-1}$ .

Table 9:: **ThermInt constants.**

Symbol	Value	Units	Description
$A_\nu$	$3 \times 10^5$	J mol $^{-1}$	Viscosity activation energy in (K6)
$A_\mu$	$2 \times 10^5$	J mol $^{-1}$	Nominal shear modulus activation energy in (K7)
$A_{sol}$	$-1.160 \times 10^{-16}$	K/m $^3$	Solidus coefficient in (K33) (ET08)
$\alpha$	$3 \times 10^{-5}$	K $^{-1}$	Thermal expansivity of mantle
$\alpha_c$	$1 \times 10^{-5}$	K $^{-1}$	Thermal expansivity of core
$B$	2.5	nd	Melt fraction coefficient in (K8)
$B_{sol}$	$1.708 \times 10^{-9}$	K/m $^2$	Solidus coefficient in (K33), calibrated
$\beta$	1/3	nd	Convective cooling exponent in (K29)
$\beta_{st}$	$1.71 \times 10^4$	GPa	Effective mantle stiffness
$c_m$	1265	J kg $^{-1}$ K $^{-1}$	Specific heat of mantle
$c_c$	840	J kg $^{-1}$ K $^{-1}$	Specific heat of core
$C_{sol}$	$-9.074 \times 10^{-3}$	K/m	Solidus coefficient in (K33), calibrated
$D$	2891	km	Mantle depth
$D_{Fe}$	7000	km	Iron solidus length scale
$D_N$	6340	km	Core adiabatic length scale
$D_{sol}$	$1.993 \times 10^4$	K	Solidus coefficient in (K33), calibrated
$\delta_{ph}$	6	nd	Rheology phase coefficient in (K8, K9)
$E_G$	$3 \times 10^5$	J kg $^{-1}$	Gravitational energy density release at ICB
$\epsilon_{UM}$	0.7	nd	Upper mantle adiabatic temperature drop
$\epsilon_{LM}$	1.3	nd	Lower mantle adiabatic temperature jump
$\epsilon_c$	0.8	nd	Average core to CMB adiabatic temperature drop
$\phi^*$	0.8	nd	Rheology phase coefficient in (K8, K9)
$g_{UM}$	9.8	m s $^{-2}$	Upper mantle gravity
$g_{LM}$	10.5	m s $^{-2}$	Lower mantle gravity
$g_c$	10.5	m s $^{-2}$	CMB gravity
$\gamma_c$	1.3	nd	Core Gruneisen parameter
$\gamma_{dip}$	0.2	nd	Magnetic dipole intensity coefficient in (K39)
$\gamma_{ph}$	6	nd	Rheology phase coefficient in (K8, K9)
$k_{UM}$	4.2	W m $^{-1}$ K $^{-1}$	Upper mantle thermal conductivity
$k_{LM}$	10	W m $^{-1}$ K $^{-1}$	Lower mantle thermal conductivity
$\kappa$	$10^{-6}$	m $^2$ s $^{-1}$	Mantle thermal diffusivity
$L_{Fe}$	750	kJ kg $^{-1}$	Latent heat of inner core crystallization
$L_{melt}$	320	kJ kg $^{-1}$	Latent heat of mantle melting
$L_e$	$2.5 \times 10^{-8}$	W Ω K $^{-1}$	Lorentz number
$L_*$	$3.09 \times 10^{23}$	W	Stellar luminosity for $M_* = 0.1M_{sun}$ (B13)

$M_m$	$4.06 \times 10^{24}$	kg	Mantle mass
$M_c$	$1.95 \times 10^{24}$	kg	Core mass
$\mu_{ref}$	$6.24 \times 10^4$	Pa	Reference shear modulus in (K7)
$\mu_0$	$4\pi \times 10^{-7}$	$\text{H m}^{-1}$	Magnetic permeability
$\nu_{ref}$	$6 \times 10^7$	$\text{m}^2\text{s}^{-1}$	Reference viscosity
$\nu_{LM}/\nu_{UM}$	2	nd	Viscosity jump from upper to lower mantle
$Q_{rad,0}$	60	TW	Initial mantle radiogenic heat flow (J07)
$R$	6371	km	Surface radius
$R_c$	3480	km	Core radius
$R_m$	4925	km	Radius to average mantle temperature $T_m$
$Ra_c$	660	nd	Critical Rayleigh number
$\rho_c$	11900	$\text{kg m}^{-3}$	Core density
$\rho_{ic}$	13000	$\text{kg m}^{-3}$	Inner core density
$\rho_m$	4800	$\text{kg m}^{-3}$	Mantle density
$\rho_{melt}$	2700	$\text{kg m}^{-3}$	Mantle melt density
$\rho_{solid}$	3300	$\text{kg m}^{-3}$	Mantle upwelling solid density
$\Delta\rho_\chi$	700	$\text{kg m}^{-3}$	Outer core compositional density difference
$\sigma_c$	$10 \times 10^5$	$\text{S m}^{-1}$	Core electrical conductivity
$T_{Fe,0}$	5600	K	Iron solidus coefficient in (K22)
$\tau_{rad}$	2.94	Gyr	Mantle radioactive decay time scale
$\tau_{rad,c}$	1.2	Gyr	Core radioactive decay time scale
$\xi$	$5 \times 10^{-4}$	nd	Rheology phase coefficient in (K8, K9)

## L. List of Symbols

In this appendix we present the definitions of all symbols used in this manuscript. Those that are general are listed first, followed by those that are specific to individual models.

### L.1. General Symbols

$a$  = semi-major axis

$e$  = eccentricity

$G$  = Newton's gravitational constant

$j$  = index

$L$  = luminosity

$M$  = mass

$M_*$  = stellar mass

$M_p$  = planetary mass

$M_j$  = mass of body  $j$

$n$  = mean motion (orbital frequency)

$\Omega$  = rotational frequency

$\Omega_j$  = rotational frequency of body  $j$

$P$  = period

$\psi$  = obliquity

$\psi_j$  = obliquity of body  $j$

$R$  = body radius

$R_p$  = planetary radius  
 $r_g$  = radius of gyration  
 $T_{eff}$  = effective temperature  
 $t$  = time

$\Phi_{jk1}$  = 1st component of binary gravitational potential

$R_0$  = CBP radial guiding center  
 $\psi_0$  = arbitrary phase offset in the  $R$  direction  
 $\varphi$  = arbitrary phase offset in the  $\phi$  direction  
 $\xi$  = arbitrary phase offset in the  $z$  direction  
 $n_k$  = CBP Keplerian mean motion  
 $n_0$  = CBP mean motion  
 $n_{AB}$  = binary mean motion  
 $e_{free}$  = binary free eccentricity  
 $i_{free}$  = binary free inclination  
 $\kappa_0$  = Radial CBP epicyclic frequency  
 $\nu_0$  = Vertical CBP epicyclic frequency

## L.2. AtmEsc Symbols

$b_{\text{diff}}$  = binary diffusion coefficient  
 $\epsilon_{\text{XUV}}$  = XUV absorption efficiency  
 $F_{\text{diff}}$  = diffusion-limited particle escape flux  
 $F_{\text{EL}}$  = energy-limited particle escape flux  
 $F_{\text{H}}$  = hydrogen particle escape flux  
 $\mathcal{F}_{\text{XUV}}$  = XUV flux  
 $k_{\text{boltz}}$  = Boltzmann constant  
 $K_{\text{tide}}$  = tidal enhancement factor  
 $m_c$  = crossover mass  
 $m_{\text{H}}$  = hydrogen atom mass  
 $m_{\text{O}}$  = oxygen atom mass  
 $T_{\text{flow}}$  = temperature of hydrodynamic flow  
 $X_{\text{O}}$  = oxygen mixing ratio

## L.4. DistOrb Symbols

$m_i$  = mass of  $i^{th}$  star  
 $a_{AB}$  = binary semi-major axis  
 $e_{AB}$  = binary eccentricity  
 $M_b$  = binary mean anomaly  
 $\varpi_B$  = binary longitude of the periapse  
 $\alpha_i$  = normalized CBP orbital distance from the  $i^{th}$  star  
 $\delta_{k0}$  = Kroenker delta function  
 $b_{(j+1)/2}^k$  = Laplace coefficient  
 $\Phi_{jk0}$  = 0th component of binary gravitational potential

$e$  = orbital eccentricity  
 $\varpi$  = [°] longitude of pericenter  
 $i$  = [°] orbital inclination  
 $\Omega$  = [°] longitude of ascending node  
 $h$  = first Poincaré coordinate for eccentricity  
 $k$  = second Poincaré coordinate for eccentricity  
 $p$  = first Poincaré coordinate for inclination  
 $q$  = second Poincaré coordinate for inclination  
 $\mathcal{R}$  = [au<sup>2</sup> day<sup>-2</sup>] disturbing function  
 $n$  = [rad day<sup>-1</sup>] mean motion  
 $\delta_R$  = post-Newtonian correction factor  
 $c$  = speed of light  
 $\mu$  = [au<sup>3</sup> day<sup>-2</sup>] mass factor of inner planet in a pair  
 $\mu'$  = [au<sup>3</sup> day<sup>-2</sup>] mass factor of outer planet in a pair  
 $\kappa$  = [au<sup>3/2</sup> day<sup>-1</sup> M<sub>⊕</sub><sup>-1/2</sup>] Gaussian gravitational constant

## L.3. BINARY Symbols

$\mathcal{R}_D$ = direct terms disturbing function	$\Omega = [^\circ]$ longitude of ascending node
$D_{0,i}$ = term $i$ of direct disturbing function	$\Upsilon = [^\circ]$ vernal point (location of sun on northern spring equinox)
$f_i$ = semi-major axis functions in disturbing function	$\xi$ = first rectangular coordinate for obliquity and precession
	$\zeta$ = second rectangular coordinate for obliquity and precession
	$\chi$ = third rectangular coordinate for obliquity and precession
	$J_{2\oplus}$ = gravitational quadrupole moment of Earth
	$\nu_\oplus = [\text{rad day}^{-1}]$ rotation rate of Earth
	$R_\oplus = [\text{m}]$ equatorial radius of Earth
	$M_\oplus = [\text{kg}]$ mass of Earth

### L.5. DistRot Symbols

$\psi = [^\circ]$ precession angle	$\varepsilon = [^\circ]$ obliquity of planet's spin axis
$R(\varepsilon) = [\text{rad day}^{-1}]$ precession rate due to stellar torque	
$p$ = first Poincaré coordinate for inclination	
$q$ = second Poincaré coordinate for inclination	
$A(p, q) = [\text{rad day}^{-1}]$ precession/obliquity term from orbital plane motion	
$B(p, q) = [\text{rad day}^{-1}]$ precession/obliquity term from orbital plane motion	
$\Gamma(p, q) = [\text{rad day}^{-1}]$ precession/obliquity term from orbital plane motion	
$p_g = [\text{rad day}^{-1}]$ geodetic (relativistic) precession rate	
$\kappa = [\text{au}^{3/2} \text{ day}^{-1} M_\odot^{-1/2}]$ Gaussian gravitational constant	
$M_\star = [\text{M}_\odot]$ mass of host star	
$M = [\text{kg}]$ mass of planet	
$J_2$ = gravitational quadrupole moment due to planetary oblateness	
$a = [\text{au}]$ semi-major axis	
$\nu = [\text{rad day}^{-1}]$ rotation rate of planet	
$C = [\text{kg m}^2]$ polar moment of inertia of planet	
$r = [\text{m}]$ equatorial radius of planet	
$S_0$ = correction term for precession due to eccentric orbit	
$\Lambda = [^\circ]$ angle between vernal point and ascending node	
	$\varepsilon$ = sign of the phase lag
	$k_2$ = Love number of degree 2
	$P_{eq}$ = equilibrium spin period
	$Q$ = tidal quality factor
	$\xi$ = constant in EqTide calculations
	$Z$ = constant in EqTide calculations

### L.6. EqTide Symbols

$\varepsilon$ = sign of the phase lag
$k_2$ = Love number of degree 2
$P_{eq}$ = equilibrium spin period
$Q$ = tidal quality factor
$\xi$ = constant in EqTide calculations
$Z$ = constant in EqTide calculations

### L.7. GalHabit Symbols

$Z = [\text{kpc}]$ height above galactic midplane
$H_{av}$ = time-averaged Hamiltonian for galactic tide
$\mu$ = mass factor
$G$ = Newtonian gravitational constant
$\rho_0$ = density of stars
$M_c$ = mass of central star
$M$ = mass of orbiter

$a$ = semi-major axis	$\vec{R}_\star$ = starting position of passing star
$L$ = canonical momentum associated with orbital energy	$x_\star$ = x component of passing star's starting position
$J$ = canonical momentum associated with total orbital angular momentum	$y_\star$ = y component of passing star's starting position
$J_z$ = canonical momentum associated with $Z$ angular momentum	$z_\star$ = z component of passing star's starting position
$\omega$ = argument of periastron	$x_\star$ = x component of passing star's starting position
$i$ = inclination of system with respect to galactic plane	$\theta_\star$ = co-latitudinal angle of passing star's starting position
$\Omega$ = longitude of ascending node	$\phi_\star$ = longitudinal angle of passing star's starting position
$l$ = mean anomaly	$f_{\text{enc},i}$ = frequency of stellar encounters of stellar type $i$
$\vec{J}$ = angular momentum vector	$M_V$ = magnitude of passing star
$J_x$ = x component of angular momentum	$\Delta M_{V,i}$ = magnitude bin size of stellar type $i$
$J_y$ = y component of angular momentum	$f_{\text{rel}}$ = frequency of stellar encounters of stellar type $i$ per magnitude
$\vec{e}$ = eccentricity vector	$\xi_{M_V}$ = randomly drawn magnitude of passing star
$e_x$ = x component of eccentricity vector	$\xi_{\text{samp}}$ = random number used in rejection sampling for magnitude
$e_y$ = y component of eccentricity vector	$\vec{v}_{h,\star}$ = relative velocity vector between system and passing star
$e_z$ = z component of eccentricity vector	$\vec{v}_\star$ = passing star's velocity vector
$\hat{e}$ = unit vector with direction of eccentricity vector	$\vec{v}_h$ = velocity of system relative to local standard of rest for stellar type $i$
$\hat{J}$ = unit vector with direction of angular momentum vector	$v_{\max}$ = threshold velocity used for passing star velocity selection
$\hat{n}$ = unit vector used in calculation of $\omega$	$n$ = mean anomaly of orbiter
$\vec{n}$ = vector used in calculation of $\omega$	$\vec{b}_1$ = impact parameter of passing star relative to host system's primary star
$\hat{Z}$ = unit vector perpendicular to galactic plane	$\vec{b}_2$ = impact parameter of passing star relative to host system's orbiter
$f_{\text{enc}}$ = frequency of stellar encounters	$\vec{R}_2$ = position of orbiter relative to primary
$R_{\text{enc}}$ = radius at which stellar encounters begin	$\Delta t_1$ = time difference until closest approach of passing star to primary
$v_i$ = velocity of typical encounter with stellar type $i$	
$n_{\star,i}$ = number density of stellar type $i$	
$v_{h,i}$ = average velocity of system relative to stellar type $i$	
$\sigma_{\star i}$ = velocity dispersion of stellar type $i$	
$t_{\text{next}}$ = time of next encounter	
$\xi$ = random number used in $t_{\text{next}}$ calculation	

$\Delta t_2$ = time difference until closest approach of passing star to orbiter	$\varpi$ = longitude of periastron
$\Delta \vec{v}_2$ = instantaneous change in velocity of orbiter due to passing star	$\psi$ = precession angle
$m_\star$ = mass of passing star	$\Upsilon$ = vernal point
	$\alpha_L$ = albedo over land
	$\alpha_W$ = albedo over water
	$P_2$ = second Legendre polynomial
	$M_{\text{ice}}$ = mass of ice on land
	$Z$ = zenith angle of sun/star at noon
	$A$ = OLR coefficient
	$B$ = OLR coefficient
	$\mathcal{M}$ = matrix used in energy balance model integration
	$\xi$ = ice ablation tuning parameter
	$\sigma$ = Stefan-Boltzmann constant
	$L_h$ = latent heat of fusion for water
	$T_{\text{freeze}}$ = freezing temperature of water
	$h$ = height of ice sheet above ground
	$H$ = height of bedrock
	$y$ = latitudinal coordinate
	$R$ = radius of planet
	$A_{\text{ice}}$ = deformability of ice
	$\rho_i$ = density of ice
	$g$ = gravitational acceleration at the surface
	$n$ = Glen's flow law exponent
	$u_b$ = flow speed of ice at the base
	$D_0$ = reference deformation rate of sediment
	$a_{\text{sed}}$ = shear stress from ice on sediment
	$b_{\text{sed}}$ = rate of increase of shear strength with depth of sediment
	$\mu_0$ = reference viscosity of sediment
	$m$ = coefficient used in basal flow calculation
	$h_s$ = depth of sediment
	$\rho_s$ = density of sediment
	$\rho_w$ = density of water
	$\phi_s$ = internal deformation angle of sediment
	$D_{\text{ice}}$ = diffusion coefficient for ice flow
	$r_{\text{snow}}$ = rate of snow accumulation
	$T_b$ = relaxation time scale of bedrock

### L.8. POISE Symbols

$\phi$ = latitude	
$x$ = sine of latitude	
$C$ = heat capacity of atmosphere	
$T$ = temperature at/near surface	
$D$ = coefficient of heat diffusion	
$I$ = outgoing longwave radiation (OLR)	
$S$ = instellation	
$\alpha$ = albedo	
$C_L$ = heat capacity over land	
$C_W^{\text{eff}}$ = heat capacity over water	
$T_L$ = temperature over land	
$T_W$ = temperature over water	
$f_L$ = land fraction of grid cell	
$f_W$ = water fraction of grid cell	
$\nu$ = land-ocean heat transport parameter	
$C_W$ = head capacity over water per meter of depth	
$m_d$ = depth of ocean mixing layer	
$\delta$ = declination of sun/host star	
$S_\star$ = flux at planet's distance from host star	
$\rho$ = planet-star distance, in semi-major axis units	
$H_0$ = hour angle of host star at sunrise/sunset	
$\varepsilon$ = obliquity	
$\theta$ = true longitude of planet	
$f$ = true anomaly of planet	
$\Delta^*$ = angle between periastron and planet's position at northern spring equinox	

$H_{eq}$  = ice-free equilibrium height of bedrock  
 $\rho_b$  = bedrock density

$T_0$  = initial temperature distribution of surface

### L.9. RadHeat Symbols

$Q_{i,j}$  = [W] radiogenic heat production of species  $i$  in reservoir  $j$

$\lambda_{i,1/2}$  = [ $\text{yr}^{-1}$ ] radiogenic decay constant of species  $i$  =  $\ln 2/\tau_{i,1/2}$

$\tau_{i,1/2}$  = [yr] radiogenic halflife of species  $i$

### L.10. SpiNBody Symbols

$F_i$  = Newtonian gravitational force on orbital body  $i$

$m_i$  = Mass of orbital body  $i$

$r_{i,j}$  = Distance between  $i$  and  $j$

$\dot{v}_i$  = Net gravitational acceleration of body  $i$

$\dot{x}_i$  = Net velocity of body  $i$

### L.11. STELLAR Symbols

$\beta_{\text{sat}}$  = XUV power law index

$L_{\text{bol}}$  = Stellar bolometric (total) luminosity

$L_{\text{XUV}}$  = Stellar XUV luminosity

$f_{\text{sat}}$  = Saturation ratio of  $L_{\text{XUV}}$  to  $L_{\text{bol}}$

$t_{\text{sat}}$  = XUV saturation timescale

$r_g$  = Stellar radius of gyration

### L.12. ThermInt Symbols

$Q_{\text{surf}}$  = [W] total mantle surface heat flow

$Q_{\text{conv}}$  = heat conducted through the lithospheric thermal boundary layer that is supplied by mantle convection

$Q_{\text{melt}}$  = heat loss due to the eruption of upwelling mantle melt at the surface

$Q_{\text{cmb}}$  = heat lost from the core conducted across the core-mantle boundary (CMB)

$Q_{\text{man}}$  = secular (sensible) heat lost from the mantle

$Q_{\text{tidal}}$  = heat generated in the mantle by tidal dissipation

$Q_{L,\text{man}}$  = latent heat released by the solidification of the mantle

$Q_{\text{core}}$  = core secular cooling

$Q_{i,\text{core}}$  = radiogenic heat production of species  $i$  in the core

$Q_{icb}$  = heat released by the solidification of the inner core

$M_{ic}$  = inner core mass

$L_{icb}$  = [J/kg] latent energy released per unit mass at the inner-core boundary (ICB)

$E_{icb}$  = [J/kg] gravitational energy released per unit mass at the ICB

$T_g$  = ground temperature

$T_{UM}$  = upper mantle temperature

$T_m$  = average mantle temperature

$T_{LM}$  = lower mantle temperature

$T_{CMB}$  = core-mantle boundary temperature

$T_c$  = average core temperature

$\delta_{UM}$  = thermal boundary layer thickness of upper mantle

$\delta_{LM}$  = thermal boundary layer thickness of lower mantle

$\epsilon_{erupt}$  = mantle melt mass extrusive eruption fraction

$A$ = Surface area of planet	$\gamma_c$ = Core Gruneisen parameter
$A_{CMB}$ = CMB area	$\gamma_{dip}$ = Magnetic dipole intensity coefficient in (K39)
$A_{ICB}$ = ICB area	$\gamma_{ph}$ = Rheology phase coefficient in (K8, K9)
$A_\nu$ = Viscosity activation energy in (K6)	$\gamma_{ad}$ = solid mantle adiabatic temperature gradient
$A_\mu$ = Nominal shear modulus activation energy in (K7)	$k_2$ = real second order Love number in (K15)
$A_{sol}$ = Solidus coefficient in (K33)	$Im(k_2)$ = imaginary second order Love number in (K16)
$\alpha$ = Thermal expansivity of mantle	$k_{UM}$ = Upper mantle thermal conductivity
$\alpha_c$ = Thermal expansivity of core	$k_{LM}$ = Lower mantle thermal conductivity
$B$ = Melt fraction coefficient in (K8)	$\kappa$ = Mantle thermal diffusivity
$B_{sol}$ = Solidus coefficient in (K33)	$k_c$ = core thermal conductivitiy
$\beta$ = Convective cooling exponent in (K29)	$L_{Fe}$ = Latent heat of inner core crystallization
$\beta_{st}$ = Effective mantle stiffness	$L_{melt}$ = Latent heat of mantle melting
$c_m$ = Specific heat of mantle	$L_e$ = Lorentz number
$c_c = 840$ = Specific heat of core	$M_m$ = Mantle mass
$C_{sol}$ = Solidus coefficient in (K33), calibrated	$M_{sol}$ = mass of solid mantle
$D$ = Mantle depth	$V_{liq}$ = volume of liquid mantle
$D_{Fe}$ = Iron solidus length scale	$M_c$ = Core mass
$D_N$ = Core adiabatic length scale	$M_{ic}$ = Inner core mass
$D_{sol}$ = Solidus coefficient in (K33), calibrated	$\mathcal{M}$ = core dynamo dipolar magnetic moment
$\delta_{ph}$ = Rheology phase coefficient in (K8, K9)	$\mu_{ref}$ = Reference shear modulus in (K7)
$E_G$ = Gravitational energy density release at ICB	$\mu_0$ = Magnetic permeability
$\epsilon_{UM}$ = Upper mantle adiabatic temperature drop	$\nu_{ref}$ = Reference viscosity
$\epsilon_{LM}$ = Lower mantle adiabatic temperature jump	$f_{\nu,UM,LM}$ = Viscosity jump from upper to lower mantle
$\epsilon_c$ = Average core to CMB adiabatic temperature drop	$q_{c,conv}$ = core convective heat flux
$\epsilon_{phase}$ = mantle rheology melt reduction factor	$q_{c,ad}$ = core adiabatic heat flux
$F_c$ = total core buoyancy flux	$Q$ = tidal quality factor
$F_{th}$ = core thermal buoyancy flux	$R$ = Surface radius
$F_\chi$ = core compositional buoyancy flux	$R_c$ = Core radius
$\phi^*$ = Rheology phase coefficient in (K8, K9)	$R_{ic}$ = Inner core radius
$g_{UM}$ = Upper mantle gravity	$R_m$ = Radius to average mantle temperature
$g_{LM}$ = Lower mantle gravity	$T_m$
$g_c$ = CMB gravity	$Ra_c$ = Critical Rayleigh number
	$\rho_c$ = Core density

$\rho_{ic}$ = Inner core density	$T_{Fe,0}$ = Iron solidus coefficient in (K22)
$\rho_m$ = Mantle density	$T_{Fe,cmb}$ = Iron solidus temperature at CMB
$\rho_{melt}$ = Mantle melt density	$T_{Fe,cen}$ = Iron solidus temperature at center of core
$\rho_{solid}$ = Mantle upwelling solid density	
$\Delta\rho_\chi$ = Outer core compositional density difference	$\xi$ = Rheology phase coefficient in (K8, K9)
$\sigma_c$ = Core electrical conductivity	

## M. VPLanet Accessibility and Support Software

In this final appendix, we describe our approaches for accessibility and reproducibility. In general, we adhere to the recommendations of the National Academies 2018 report *Open Science by Design*<sup>3</sup>. This study identified numerous challenges in science as software and data sets grow to very large scales. **VPLanet** brings together numerous models from disparate fields of science, and is therefore inscrutable to many professional scientists. Moreover, **VPLanet** can produce large amounts of high-dimensional data that can be difficult for the user to digest. More philosophically, given that the challenge of detecting life beyond the Solar System is daunting, and the potential societal impact of such a discovery is huge, it is critical that the scientific process that culminates in such an announcement be as transparent as possible. To address these issues, **VPLanet** has been designed and released to maximize usability and clarity, including the addition of new modules and data management.

### M.1. Parameter Sweeps: vspace

**vspace** is a `python` code that can be used to conveniently generate initial conditions for **VPLanet** simulations (it does not run **VPLanet** itself). This option is ideal when the user wishes to run a large number of simulations, perhaps on a cluster. Initial conditions can be generated in a random (Monte Carlo) fashion or over a regular grid. The user creates a template plain text file that contains a list of all desired input files, with a list of variables that are to be changed, iterated over, or randomly drawn. **vspace** operates on this text file, determines which files are to be copied to new directories, which input parameters are to be varied, and then creates a new directory that contains (as individual directories) all the desired simulations. When used in random mode, the user sets the total number of simulations and the parameters to be sampled along with details about the distributions.

---

<sup>3</sup><https://www.nap.edu/catalog/25116/open-science-by-design-realizing-a-vision-for-21st-century>

Current distribution types are uniform, Gaussian/normal, uniform in sine, or uniform in cosine. When used in grid mode, the user does not need to specify the total number of simulations. One simply sets all of the parameters to be varied, along with the spacing type (linear or logarithmic), and spacing size, or the total range and number of grid points. `VSPACE` automatically determines the number of simulations and identifies every permutation of the desired set of input parameters using the `itertools` library. There is no limit to the number of parameters that can be iterated over in a single set of simulations, thus the user should be cautious about generating large numbers of files.

## M.2. Plotting: `VPlot`

The `VPlot` package is recommended for interacting with and visualizing the output of `VPLanet` simulations. `VPlot` is coded in `Python` and is installable via the `pip` command or from source on `GitHub`<sup>4</sup>. `VPlot` reads any `.log` and `.forward` files generated by a `VPLanet` run in the current working directory and provides an object-oriented interface to the simulation output, with convenience plotting functions. `VPlot` can also be run from the command line, providing a quick graphical view of the simulation output. For more information on `VPlot`, please read the documentation. Note that all plots in this document that display `VPLanet` output have utilized `VPlot`.

## M.3. Data Management: `BigPlanet`

`BigPlanet` is an accompanying Python package for storing the output of a large number of `VPLanet` simulations. For large numbers of `VPLanet` simulations, *i.e.*, a suite over a large grid of initial conditions, the total size of the output for all simulations can exceed what can be stored in memory, necessitating out-of-core solutions. `BigPlanet` solves this issue by using the HDF5 data storage format<sup>5</sup> for efficiently storing full time series simulation outputs for easy access. `BigPlanet` leverages the hierarchical structure of the HD5F format by storing each simulation as a group, each simulation body as a subgroup of the simulation, and each variable as a subgroup of its parent body. `BigPlanet` wraps the HDF5 file interface in easy-to-use Python code, using the `H5PY`<sup>6</sup> Python package, to allow users to easily read

---

<sup>4</sup><https://github.com/VirtualPlanetaryLaboratory/vplot>

<sup>5</sup><https://support.hdfgroup.org/HDF5/>

<sup>6</sup><https://www.h5py.org/>

and manipulate `vPLanet` simulation outputs from storage for in-memory analysis. `BigPlanet` works for both Python 2.7 and 3.6+, is extensively documented, and comes with several example scripts and Jupyter notebooks that demonstrate its typical use cases.

#### M.4. The `vPLanet` Repository

The `vPLanet` repository contains the source code, example scripts, and documentation to facilitate its use. The master branch to this `git` repository is stable, and the results presented in this manuscript can all be obtained by using it. The `vPLanet` team continuously checks that all new updates reproduce past results through continuous integration<sup>7</sup>, and periodically searches for memory issues using `valgrind`<sup>8</sup> and `addresssanitizer`<sup>9</sup>.

Community input and additions are welcome. Pull requests should be issued to the “dev” branch and will be reviewed before being merged with the master branch. As new features and modules are added to the software suite, this document will be updated and available in the [Manual](#) sub-directory.

## REFERENCES

- Abe, Y., Abe-Ouchi, A., Sleep, N. H., & Zahnle, K. J. 2011, *Astrobiology*, 11, 443
- Allart, R., Bourrier, V., Lovis, C., et al. 2019, *Astron. & Astrophys.*, 623, A58
- Andrault, D., Bofan-Casanova, N., Nigro, G. L., et al. 2011, *Earth and planetary science letters*, 304, 251
- Anglada-Escudé, G., Amado, P. J., Barnes, J., et al. 2016, *Nature*, 536, 437
- Arevalo, R., McDonough, W. F., Stracke, A., et al. 2013, *Geochemistry, Geophysics, Geosystems*, 14, 2265
- Armstrong, J. C., Barnes, R., Domagal-Goldman, S., et al. 2014, *Astrobiology*, 14, 277
- Armstrong, J. C., Leovy, C. B., & Quinn, T. 2004, *Icarus*, 171, 255

---

<sup>7</sup><https://travis-ci.org/>

<sup>8</sup><http://valgrind.org/>

<sup>9</sup><https://github.com/google/sanitizers/wiki/AddressSanitizer>

- Baraffe, I., Homeier, D., Allard, F., & Chabrier, G. 2015, *Astron. & Astrophys.*, 577, A42
- Barker, B. M., & O'Connell, R. F. 1970, Phys. Rev. D, 2, 1428
- Barnes, R. 2017, Celestial Mechanics and Dynamical Astronomy, 129, 509
- Barnes, R., Deitrick, R., Greenberg, R., Quinn, T. R., & Raymond, S. N. 2015, *Astrophys. J.*, 801, 101
- Barnes, R., Mullins, K., Goldblatt, C., et al. 2013, Astrobiology, 13, 225
- Berger, A., & Loutre, M. F. 1991, Quaternary Science Reviews, 10, 297
- Berger, A. L. 1978, Journal of Atmospheric Sciences, 35, 2362
- Bills, B. G., & Ray, R. D. 2000, *J. Geophys. Res.*, 105, 29277
- Bolmont, E., Raymond, S. N., Leconte, J., & Matt, S. P. 2012, *Astron. & Astrophys.*, 544, A124
- Bolmont, E., Selsis, F., Owen, J. E., et al. 2017, *Mon. Not. R. Astron. Soc.*, 464, 3728
- Braithwaite, R. J., & Zhang, Y. 2000, Journal of Glaciology, 46, 7
- Brasser, R., Ida, S., & Kokubo, E. 2014, *Mon. Not. R. Astron. Soc.*, 440, 3685
- Chassefière, E. 1996a, *J. Geophys. Res.*, 101, 26039
- . 1996b, *Icarus*, 124, 537
- Chassefière, E., & Leblanc, F. 2004, Planetary and Space Science, 52, 1039
- Clark, P. U., & Pollard, D. 1998, Paleoceanography, 13, 1
- Cogné, J.-P., & Humler, E. 2004, Earth and Planetary Science Letters, 227, 427
- Collins, B. F., & Sari, R. 2010, *Astron. J.*, 140, 1306
- Colombo, G., & Shapiro, I. I. 1966, *Astrophys. J.*, 145, 296
- Cook, A. H. 1980, *Interiors of the planets*, Cambridge planetary science series (Cambridge [England] ; New York: Cambridge University Press)
- Costa, A., Caricchi, L., & Bagdassarov, N. 2009, *Geochemistry, Geophysics, Geosystems*, 10

- Crank, J., Nicolson, P., & Hartree, D. R. 1947, Proceedings of the Cambridge Philosophical Society, 43, 50
- Cranmer, S. R., & Saar, S. H. 2011, *Astrophys. J.*, 741, 54
- Darwin, G. H. 1880, Royal Society of London Philosophical Transactions Series I, 171, 713
- Deitrick, R., Barnes, R., Quinn, T. R., et al. 2018a, *Astron. J.*, 155, 60
- Deitrick, R., Barnes, R., Bitz, C., et al. 2018b, *Astron. J.*, 155, 266
- Dobrovolskis, A. R. 2009, *Icarus*, 204, 1
- Donahue, T. M., Hoffman, J. H., Hodges, R. R., & Watson, A. J. 1982, Science, 216, 630
- Doyle, L. R., Carter, J. A., Fabrycky, D. C., et al. 2011, Science, 333, 1602
- Driscoll, P., & Bercovici, D. 2014, Physics of the Earth and Planetary Interiors, 236, 36
- Driscoll, P., & Bercovici, D. 2014, Physics of the Earth and Planetary Interiors, 236, 36
- Driscoll, P., & Olson, P. 2011, *Icarus*, 213, 12
- Driscoll, P. E., & Barnes, R. 2015, Astrobiology, 15, 739
- Duncan, M., Quinn, T., & Tremaine, S. 1987, *Astron. J.*, 94, 1330
- Efroimsky, M., & Makarov, V. V. 2013, *Astrophys. J.*, 764, 26
- Efroimsky, M., & Williams, J. G. 2009, Celestial Mechanics and Dynamical Astronomy, 104, 257
- Elkins-Tanton, L. 2008, Earth and Planetary Science Letters, 271, 181
- Elkins-Tanton, L. T. 2012, Annual Review of Earth and Planetary Sciences, 40, 113
- Ellis, K. M., & Murray, C. D. 2000, *Icarus*, 147, 129
- Erkaev, N. V., Kulikov, Y. N., Lammer, H., et al. 2007, A&A, 472, 329
- Ferraz-Mello, S., Rodríguez, A., & Hussmann, H. 2008, Celestial Mechanics and Dynamical Astronomy, 101, 171
- Ferraz-Mello, S., Rodríguez, A., & Hussmann, H. 2008, Celestial Mechanics and Dynamical Astronomy, 101, 171

- Fleming, D. P., Barnes, R., Davenport, J. R. A., & Luger, R. 2019, arXiv e-prints, arXiv:1903.05686
- Fleming, D. P., Barnes, R., Graham, D. E., Luger, R., & Quinn, T. R. 2018, *Astrophys. J.*, 858, 86
- Fleming, D. P., & VanderPlas, J. 2018, *The Journal of Open Source Software*, 3, 781
- García-Sánchez, J., Weissman, P. R., Preston, R. A., et al. 2001, *Astron. & Astrophys.*, 379, 634
- Gillmann, C., Chassefière, E., & Lognonné, P. 2009, *Earth and Planetary Science Letters*, 286, 503
- Gillon, M., Triaud, A. H. M. J., Demory, B.-O., et al. 2017, *Nature*, 542, 456
- Glen, J. W. 1958, *Nature*, 182, 1560
- Goldreich, P. 1966, *Astron. J.*, 71, 1
- Goldreich, P., & Soter, S. 1966, *Icarus*, 5, 375
- Goldreich, P., & Soter, S. 1966, *Icarus*, 5, 375
- Gomi, H., Ohta, K., Hirose, K., et al. 2013, *Physics of the Earth and Planetary Interiors*, 224, 88
- Greenberg, R. 2009, *Astrophys. J.*, 698, L42
- Heisler, J., & Tremaine, S. 1986, *Icarus*, 65, 13
- Heisler, J., Tremaine, S., & Alcock, C. 1987, *Icarus*, 70, 269
- Heller, R., Leconte, J., & Barnes, R. 2011, *Astro. & Astrophys.*, 528, A27+
- Henning, W., O’Connell, R., & Sasselov, D. 2009, *The Astrophysical Journal*, 707, 1000
- Hirschmann, M. 2000, *Geochemistry Geophysics Geosystems*, 1, 1042:1
- Howard, L. N. 1966, in *Applied Mechanics* (Springer), 1109–1115
- Hunten, D. M. 1973, *Journal of Atmospheric Sciences*, 30, 1481
- Hunten, D. M., Pepin, R. O., & Walker, J. C. G. 1987, *Icarus*, 69, 532
- Hut, P. 1981, *Astro. & Astrophys.*, 99, 126

- Huybers, P., & Tziperman, E. 2008, *Paleoceanography*, 23, PA1208
- Jackson, A. P., Davis, T. A., & Wheatley, P. J. 2012, *Mon. Not. R. Astron. Soc.*, 422, 2024
- Jackson, B., Barnes, R., & Greenberg, R. 2009, *The Astrophysical Journal*, 698, 1357
- Jackson, B., Greenberg, R., & Barnes, R. 2008, *Astrophys. J.*, 678, 1396
- Jackson, I., Faul, U. H., Gerald, F., John, D., & Tan, B. H. 2004, *Journal of Geophysical Research: Solid Earth* (1978–2012), 109
- Jaupart, C., Labrosse, S., Lucaleau, F., & Mareschal, J. C. 2015, in *Treatise on Geophysics*, 2nd edn., ed. D. Bercovici, Vol. 7 *Mantle Dynamics* (Elsevier), 253–305
- Jenson, J. W., Macayeal, D. R., Clark, P. U., Ho, C. L., & Vela, J. C. 1996, *J. Geophys. Res.*, 101, 8717
- Johnson, R. E., Volkov, A. N., & Erwin, J. T. 2013, *ApJL*, 768, L4
- Kaib, N. A., Raymond, S. N., & Duncan, M. 2013, *Nature*, 493, 381
- Kasting, J. F. 1988, *Icarus*, 74, 472
- Kasting, J. F., & Pollack, J. B. 1983, *Icarus*, 53, 479
- Kasting, J. F., Pollack, J. B., & Ackerman, T. P. 1984, *Icarus*, 57, 335
- Kasting, J. F., Whitmire, D. P., & Reynolds, R. T. 1993, *Icarus*, 101, 108
- Kenyon, S. J., & Bromley, B. C. 2004, *Nature*, 432, 598
- Kinoshita, H. 1975, SAO Special Report, 364
- . 1977, *Celestial Mechanics*, 15, 277
- Kopparapu, R. K., Ramirez, R., Kasting, J. F., et al. 2013, *Astrophys. J.*, 765, 131
- Kordopatis, G., Binney, J., Gilmore, G., et al. 2015, *Mon. Not. R. Astron. Soc.*, 447, 3526
- Labrosse, S., Poirier, J., & Le Mouël, J. 2001, *Earth Planet. Sci. Lett.*, 190, 111
- Lambeck, K. 1977, Royal Society of London Philosophical Transactions Series A, 287, 545
- Lammer, H., Erkaev, N. V., Odert, P., et al. 2013, *Mon. Not. R. Astron. Soc.*, 430, 1247
- Laskar, J. 1986, *Astron. & Astrophys.*, 157, 59

- Laskar, J., Correia, A. C. M., Gastineau, M., et al. 2004, *Icarus*, 170, 343
- Laskar, J., Joutel, F., & Boudin, F. 1993, *Astron. & Astrophys.*, 270, 522
- Leconte, J., Chabrier, G., Baraffe, I., & Levrard, B. 2010, *Astro. & Astrophys.*, 516, A64+
- Lee, M. H., & Peale, S. J. 2006, *Icarus*, 184, 573
- Lefebvre, F., Gallée, H., van Ypersele, J.-P., & Huybrechts, P. 2002, *Annals of Glaciology*, 35, 391
- Lehmer, O. R., & Catling, D. C. 2017, *Astrophys. J.*, 845, 130
- Leung, G. C. K., & Lee, M. H. 2013, *Astrophys. J.*, 763, 107
- Lincowski, A. P., Meadows, V. S., Crisp, D., et al. 2018, *Astrophys. J.*, 867, 76
- Line, M. R., Knutson, H., Wolf, A. S., & Yung, Y. L. 2014, *Astrophys. J.*, 783, 70
- Lissauer, J. J. 2007, *Astrophys. J. Lett.*, 660, L149
- Lopez, E. D., & Fortney, J. J. 2014, *Astrophys. J.*, 792, 1
- Lopez, E. D., Fortney, J. J., & Miller, N. 2012, *Astrophys. J.*, 761, 59
- Lopez, E. D., & Rice, K. 2016, arXiv e-prints, arXiv:1610.09390
- Lovett, E. O. 1895, *Astron. J.*, 15, 113
- Luger, R., & Barnes, R. 2015, *Astrobiology*, 15, 119
- Luger, R., Barnes, R., Lopez, E., et al. 2015, *Astrobiology*, 15, 57
- Lurie, J. C., Vyhmeister, K., Hawley, S. L., et al. 2017, *Astron. J.*, 154, 250
- Lynch, C. R., Murphy, T., Lenc, E., & Kaplan, D. L. 2018, *Mon. Not. R. Astron. Soc.*, 478, 1763
- MacDonald, G. J. F. 1964, *Reviews of Geophysics and Space Physics*, 2, 467
- MacDonald, R. J., & Madhusudhan, N. 2019, *Mon. Not. R. Astron. Soc.*, 801
- Mardling, R. A., & Lin, D. N. C. 2002, *Astrophys. J.*, 573, 829
- Matt, S. P., Brun, A. S., Baraffe, I., Bouvier, J., & Chabrier, G. 2015, *Astrophys. J. Lett.*, 799, L23

- . 2019, *Astrophys. J. Lett.*, 870, L27
- McKenzie, D. 1984, Journal of Petrology, 25, 713
- McKenzie, D., & Bickle, M. 1988, Journal of Petrology, 29, 625
- McQuillan, A., Mazeh, T., & Aigrain, S. 2014, *Astrophys. J. Supp.*, 211, 24
- Meadows, V. S., & Barnes, R. K. 2018, Factors Affecting Exoplanet Habitability, 57
- Meadows, V. S., Arney, G. N., Schwieterman, E. W., et al. 2018, Astrobiology, 18, 133
- Meibom, S., & Mathieu, R. D. 2005, *Astrophys. J.*, 620, 970
- Minchev, I., Famaey, B., Quillen, A. C., et al. 2012, *Astron. & Astrophys.*, 548, A127
- Moore, W. 2003, Journal of Geophysical Research: Planets (1991–2012), 108
- Moore, W. B. 2003, Journal of Geophysical Research (Planets), 108, 5096
- Morbidelli, A., Karato, S.-I., Ikoma, M., et al. 2018, Space Sci. Rev., 214, 110
- Murray, C. D., & Dermott, S. F. 1999, Solar system dynamics (Cambridge University Press)
- North, G. R., & Coakley, Jr., J. A. 1979, Journal of Atmospheric Sciences, 36, 1189
- Nortmann, L., Pallé, E., Salz, M., et al. 2018, Science, 362, 1388
- Odert, P., Erkaev, N. V., Kislyakova, K. G., et al. 2019, arXiv e-prints, arXiv:1903.10772
- Olson, P., & Christensen, U. 2006, Earth Planet. Sci. Lett., 250, 561
- O'Reilly, T. C., & Davies, G. F. 1981, Geophysical Research Letters, 8, 313
- Owen, J. E., & Mohanty, S. 2016, *Mon. Not. R. Astron. Soc.*, 459, 4088
- Owen, J. E., & Wu, Y. 2013, ArXiv e-prints, arXiv:1303.3899
- . 2017, *Astrophys. J.*, 847, 29
- Paterson, W. S. B. 1994, The physics of glaciers
- Peale, S. J., Cassen, P., & Reynolds, R. T. 1979, Science, 203, 892
- Pozzo, M., Davies, C., Gubbins, D., & Alfè, D. 2012, Nature, 485, 355

- Press, W. H., Flannery, B. P., Teukolsky, S. A., Vetterling, W. T., & Gould, H. 1987, American Journal of Physics, 55, 90
- Prša, A., Harmanec, P., Torres, G., et al. 2016, *Astron. J.*, 152, 41
- Rasio, F. A., Tout, C. A., Lubow, S. H., & Livio, M. 1996, *Astrophys. J.*, 470, 1187
- Rauch, K. P., & Hamilton, D. P. 2002, in Bulletin of the American Astronomical Society, Vol. 34, AAS/Division of Dynamical Astronomy Meeting #33, 938
- Reid, I. N., Gizis, J. E., & Hawley, S. L. 2002, *Astron. J.*, 124, 2721
- Reiners, A., & Mohanty, S. 2012, *Astrophys. J.*, 746, 43
- Remy, F., & Mignard, F. 1985, *Icarus*, 63, 1
- Repetto, S., & Nelemans, G. 2014, *Mon. Not. R. Astron. Soc.*, 444, 542
- Ribas, I., Guinan, E. F., Güdel, M., & Audard, M. 2005, *Astrophys. J.*, 622, 680
- Rickman, H., Fouchard, M., Froeschlé, C., & Valsecchi, G. B. 2008, Celestial Mechanics and Dynamical Astronomy, 102, 111
- Robertson, P., Mahadevan, S., Endl, M., & Roy, A. 2014, Science, 345, 440
- Rodríguez, A., Ferraz-Mello, S., Michtchenko, T. A., Beaugé, C., & Miloni, O. 2011, *Mon. Not. R. Astron. Soc.*, 415, 2349
- Roškar, R., Debattista, V. P., Quinn, T. R., Stinson, G. S., & Wadsley, J. 2008, *Astrophys. J. Lett.*, 684, L79
- Roškar, R., Debattista, V. P., Quinn, T. R., & Wadsley, J. 2012, *Mon. Not. R. Astron. Soc.*, 426, 2089
- Scalo, J., Kaltenegger, L., Segura, A. G., et al. 2007, *Astrobiology*, 7, 85
- Schaefer, L., Wordsworth, R. D., Berta-Thompson, Z., & Sasselov, D. 2016, *Astrophys. J.*, 829, 63
- Segatz, M., Spohn, T., Ross, M., & Schubert, G. 1988, *Icarus*, 75, 187
- Skumanich, A. 1972, *Astrophys. J.*, 171, 565
- Solomatov, V. 1995, *Physics of Fluids*, 7, 266

- Sotin, C., Grasset, O., & Mocquet, A. 2007, *Icarus*, 191, 337
- Sotin, C., & Labrosse, S. 1999, Physics of the earth and planetary interiors, 112, 171
- Tian, F. 2015, *Earth and Planetary Science Letters*, 432, 126
- Touma, J., & Wisdom, J. 1993, *Science*, 259, 1294
- . 1994, *Astron. J.*, 108, 1943
- Udry, S., Bonfils, X., Delfosse, X., et al. 2007, *Astron. & Astrophys.*, 469, L43
- van Dishoeck, E. F., Bergin, E. A., Lis, D. C., & Lunine, J. I. 2014, *Protostars and Planets VI*, 835
- Veeder, G. J., Davies, A. G., Matson, D. L., et al. 2012, *Icarus*, 219, 701
- Veeder, G. J., Matson, D. L., Johnson, T. V., Blaney, D. L., & Goguen, J. D. 1994, *J. Geophys. Res.*, 99, 17095
- Volkov, A. N., & Johnson, R. E. 2013, *ApJ*, 765, 90
- Ward, W. R. 1992, Long-term orbital and spin dynamics of Mars, ed. H. H. Kieffer, B. M. Jakosky, C. W. Snyder, & M. S. Matthews (U of Arizona Press), 298–320
- Ward, W. R., & Hamilton, D. P. 2004, *Astron. J.*, 128, 2501
- Ward, W. R., & Rudy, D. J. 1991, *Icarus*, 94, 160
- Watson, A. J., Donahue, T. M., & Walker, J. C. G. 1981, *Icarus*, 48, 150
- Williams, J. G., Sinclair, W. S., & Yoder, C. F. 1978, *Geophys. Res. Lett.*, 5, 943
- Winn, J. N., & Holman, M. J. 2005, *Astrophys. J. Lett.*, 628, L159
- Wisdom, J. 2008, *Icarus*, 193, 637
- Wright, N. J., Drake, J. J., Mamajek, E. E., & Henry, G. W. 2011, *Astrophys. J.*, 743, 48
- Wu, Y., & Goldreich, P. 2002, *Astrophys. J.*, 564, 1024
- Yoder, C. F. 1995, in Global Earth Physics: A Handbook of Physical Constants, ed. T. J. Ahrens, 1–31
- Zahn, J.-P. 1989, *Astron. & Astrophys.*, 220, 112

Zahn, J.-P., & Bouchet, L. 1989, *Astron. & Astrophys.*, 223, 112

Zahnle, K. J., & Kasting, J. F. 1986, *Icarus*, 68, 462

Zahnle, K. J., Kasting, J. F., & Pollack, J. B. 1988, *Icarus*, 74, 62

Zhang, K., & Hamilton, D. P. 2008, *Icarus*, 193, 267